

A Proposal to enhance the DUNE Near-Detector Complex

G. Adamov^{1,10}, L. Alvarez Russo², I. Bagaturia¹, P. Bernardini^{3,4}, S. Bertolucci^{5,6}, M. Bhattacharjee⁷, B. Bhuyan⁷, S. Biagi⁸, A. Caminata⁹, A. Cervelli⁵, D. Chokheli^{1,10}, A. Chukanov¹⁰, S. Davini⁹, S. Di Domizio^{9,11}, C. Distefano⁸, L. Di Noto^{9,11}, M. Diwan⁴¹², H. Duyang¹³, A. Falcone^{14,15}, O. Fedin¹⁶, A. Ferrari¹⁷, F. Ferraro^{9,11}, A. Gabrielli⁵, M. Guerzoni⁵, B. Guo¹³, M.A. Iliescu^{18,19}, A.L. Kataev²⁰, A. Khvedelidze^{1,10}, B. Kirby¹², U. Kose^{5,19}, S.A. Kulagin²⁰, C. Kullenberg¹⁰, C. Kuruppu¹³, I. Lomidze¹, G. Laurenti⁵, V. Maleev¹⁶, G. Mandrioli⁵, N. Mauri^{5,6}, P. Mehta²¹, S.R. Mishra¹³, N. Moggi^{5,6}, A. Montanari⁵, S. Movchan¹⁰, S. Nagu²², F. Olness²³, M. Pallavicini^{9,11}, R. Papaleo⁸, L. Pasqualini^{5,6}, L. Patrizii⁵, R. Petti¹³, V. Pia^{5,6}, F. Poppi^{5,6}, V.K.S. Potukuchi²⁴, M. Pozzato^{5,6}, G. Riccobene⁸, P.R. Sala²⁵, O. Samoylov¹⁰, P. Sapienza⁸, F. H. Sawy^{26,28}, Ja. Singh²², Jy. Singh²², V. Singh²⁷, G. Sirri⁵, L. Stanco²⁶, A. Surdo⁴, M. Tenti⁵, F. Terranova^{14,15}, G. Testera⁹, M. Torti^{14,15}, N. Tosi⁵, R. Travaglini²⁶, Z. Tsamalaidze^{1,10}, N. Tsverava^{1,10}, and S. Zucchelli^{5,6}

¹Georgian Technical University (GTU), 0175 Tbilisi, Georgia

²Instituto de Fisica Corpuscular (IFIC), Valencia, Spain

³Dipartimento di Matematica e Fisica, Università del Salento, 73100 Lecce, Italy

⁴INFN, Sezione di Lecce, 73100 Lecce, Italy

⁵INFN, Sezione di Bologna, 40127 Bologna, Italy

⁶Dipartimento di Fisica e Astronomia dell’Università di Bologna, 40127 Bologna, Italy

⁷Indian Institute of Technology Guwahati, Guwahati, 781039, India

⁸INFN, Laboratori Nazionali del Sud, 95125 Catania Italy

⁹INFN Sezione Genova, 16146 Genova, Italy

¹⁰Joint Institute for Nuclear Research, JINR Dubna, 141980 Moscow Region, Russia

¹¹Dipartimento di Fisica, Università degli Studi di Genova, 16146 Genova, Italy

¹²Brookhaven National Laboratory, Upton, NY 11973, USA

¹³Department of Physics and Astronomy, Univ. of South Carolina, Columbia, SC 29208, USA

¹⁴Università degli Studi di Milano Bicocca, Milano, Italy

¹⁵INFN, Sezione di Milano Bicocca, 20126, Milano, Italy

¹⁶ Petersburg Nuclear Physics Institute, PNPI, 188300 Gatchina, Russia

¹⁷Helmholtz-Zentrum Dresden-Rossendorf, 01328 Dresden, Germany

¹⁸INFN, Laboratori Nazionali di Frascati, 00044 Frascati, Italy

¹⁹CERN, 1211 Geneva 23, Switzerland

²⁰Institute for Nuclear Research of the Russian Academy of Sciences, 117312 Moscow, Russia

²¹Jawaharlal Nehru University, New Delhi, 110067, India

²²University of Lucknow, 226007, India

²³Southern Methodist University, Dallas, Texas 75205, USA

²⁴University of Jammu, 180006, India

²⁵INFN, Sezione di Milano, 20133 Milano, Italy

²⁶INFN, Sezione di Padova, 35131 Padova, Italy

²⁷Banaras Hindu University, 221005, India

²⁸Dipartimento di Fisica e Astronomia dell’Università di Padova, 35131 Padova, Italy

May 25, 2019

Contents

1	Introduction	3
1.1	The near detector of DUNE	4
1.2	Requirements for the DUNE ND	5
2	Physics Program	7
2.1	Reduced Systematics for Long-baseline Oscillation Analyses	7
2.1.1	$\Phi(E_\nu)$ Measurements	8
2.1.2	$R_{\text{phys}}(E_\nu, E_{\text{vis}})$ Constraints	8
2.2	Physics Facility for Precision Measurements and Searches	9
2.2.1	Electroweak Precision Measurements	9
2.2.2	Tests of Isospin Physics and Sum Rules	10
2.2.3	Measurements of the Strangeness Content of the Nucleon	10
2.2.4	Nucleon Structure and QCD Studies	10
2.2.5	Studies of (Anti)Neutrino-Nucleus Interactions	11
2.2.6	Searches for New Physics	11
3	Detector description	12
3.1	The KLOE magnet	12
3.2	The KLOE EM calorimeter	12
3.3	Inner Tracker	14
3.3.1	Straw Tube Tracker	16
3.3.2	Internal LAr target	18
3.4	Electronic Readout for STT	18
3.4.1	STT Readout Requirements	18
3.4.2	VMM3a ASIC Architecture	19
3.4.3	VMM3a ASIC Performance	20
3.4.4	VMM3a ASIC Readout and STT Spatial Constraints	21
3.4.5	Experience with VMM3a ASIC Readout in Cathode Strip Chambers	22
3.4.6	VMM3a ASIC Readout DAQ Options	22
3.4.7	VMM3a ASIC Readout Cost and Development Plan	23
3.5	External range catcher	24
3.6	Calibration and Monitoring	24
4	Simulation setup and tools	25
4.1	Neutrino fluxes	25
4.2	Generators	25
4.2.1	GENIE	25
4.2.2	NUNDIS in FLUKA	28
4.3	Detector simulation	30
4.3.1	FLUKA	30
4.3.2	GEANT4-based simulation	31
5	Neutrino event reconstruction	33
5.1	Single particles	33
5.1.1	Muon momentum and angular resolutions	33
5.1.2	Electron momentum and angular resolutions	34
5.1.3	π^0 identification and reconstruction	36
5.1.4	Neutron detection	38
5.1.5	Neutron energy reconstruction by time of flight technique	39
5.2	Particle Identification	40
5.2.1	Optimization of the STT Radiators	43
5.3	Full event reconstruction	44
5.4	CC events	45

6	Expected Physics Performance	46
6.1	Measurements of $\nu(\bar{\nu})$ -Hydrogen Interactions	46
6.1.1	Determination of Relative and Absolute Fluxes	49
6.1.2	Constraining the Nuclear Smearing in Ar	52
6.2	ν -e Elastic Scattering	53
6.3	Coherent π^\pm Production	56
6.4	ν_e/ν_μ & $\bar{\nu}_e/\bar{\nu}_\mu$ Flux Ratios	57
6.5	Low- ν Relative Flux	57
7	Coupling with external LAr detector	61
8	Backgrounds	63
9	Technical feasibility	65
9.1	Disassembling KLOE	65
9.2	Cost and Schedule: STT tracker	75
10	Summary of conclusions	76
11	Conclusions	76

Abstract

The Long-Baseline Neutrino Facility (LBNF) offers a unique opportunity for neutrino physics due to its high intensity (anti)neutrino beam(s) with a broad energy spectrum. The project envisages a near (ND) and a far detector (FD) to control the fluxes and the systematic, and to contribute to Short-baseline neutrino physics. In this paper we discuss the requirements for the ND and its possible implementation within the current design of DUNE. In particular, the potential use of well performing already exploited detectors is studied, addressing the re-use of the KLOE magnet and the electromagnetic calorimeter, and the addition of a straw tube tracker (STT). The performances of that layout have been obtained with great details and large simulations, also in view of its potential in a movable configuration.

1 Introduction

The largest neutrino project is under active development in U.S.A., the begin of data taking being foreseen in 2026. A multi-detector system is envisaged to fully accomplish the massive physics opportunities available for the neutrino studies and related fields, like the detection of supernova explosions.

As largely demonstrated by the previous similar neutrino experiments, a key point of the project is given by an optimized near detector (ND) arrangement, which undergoes the twofold requirements: event detection in a very refined interplay with the far detection, and exploitation of the short-baseline neutrino physics like e.g. cross-section measurements.

This paper will address the effects, constraints and generic issues for both the requirements, further describing the possible design of a multipurpose detector.

The Near Detector Concept Study Group has provided recommendations for the ND baseline configuration. The recommended concept (as of January 2019) corresponds to a near detector suite consisting of a Liquid Argon Time projection Chamber (LArTPC) (not in a magnetic field) matched to a Multi-Purpose Detector (MPD) with magnetic field, consisting of a High Pressure TPC (HPgTPC), an ElectroMagnetic Calorimeter (ECAL) and 3D Scintillator Tracker (3DST). It was also recommended to pursue additional studies of a movable LAr detector that can make measurements at one or more off-axis positions (DUNE-PRISM) for technical feasibility and cost.

The work presented in this paper aims to complement the baseline study just reported suggesting the addition of another MPD system that can be accommodated into the baseline systems. An added value of our proposal stays in its reliability, complementary and tested integration, as well as the full possibility to move it in any of the off-axis positions.

In Section 1 the description of the possible site at FNAL as well as the basic physics requirements are provided. In Section 2 the physics program for the near detection is addressed, while in Section 3 a possible setup for the detector is given. Sections 4 describes the simulation tools and the event generation, while the event reconstruction is reported in Section 5. Physics performances with the chosen detector configuration are extensively reported in Section 6. Section 7 deals with the delicate issue of the coupled Liquid Argon detection, while backgrounds are described in Section 8. Finally, Section 9 reports the issues about the KLOE dismantling and the possible costs for the STT. Summary and conclusions are given at the end.

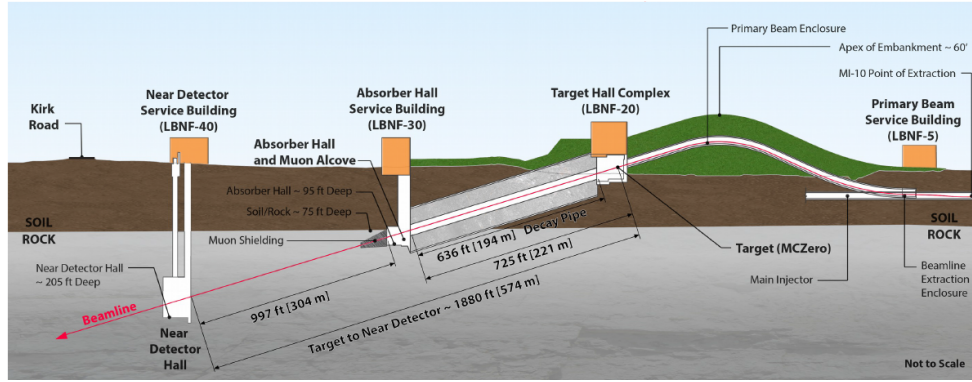


Figure 1: The DUNE neutrino beam line

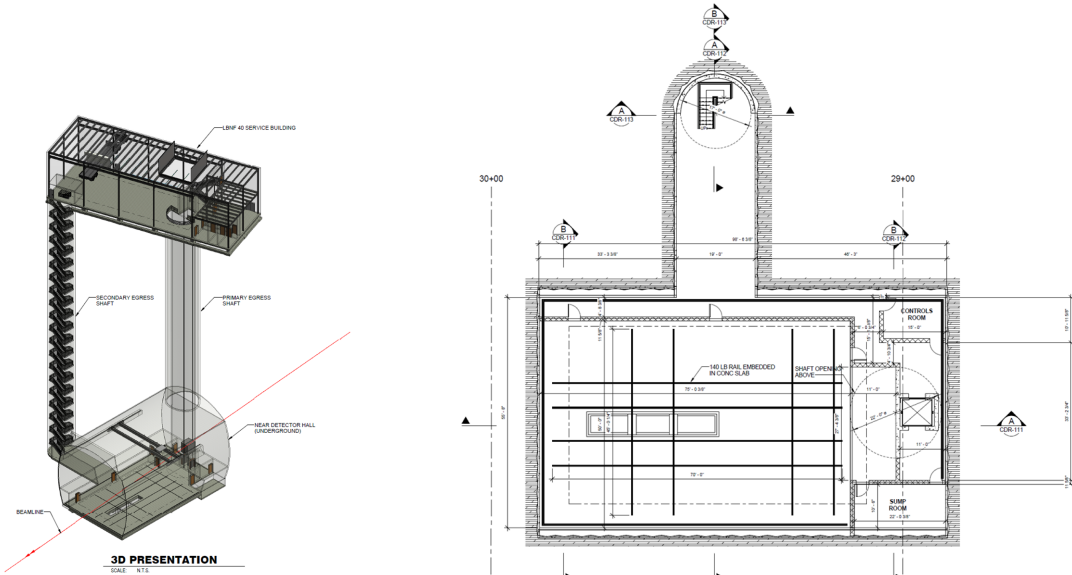


Figure 2: 3D rendering of the Near detector shaft and hall

Figure 3: Baseline drawing of the ND cavern

1.1 The near detector of DUNE

The near detector of dune (ND) will be placed 62 m underground, at a distance of 574 m from target. A schematic view of the neutrino beam line and near detector location is shown in Fig. 1, while Fig. 2 is a three dimensional rendering of the ND access shaft and hall. The actual dimensions and precise location of the ND cavern are still object of optimization. According to the recommendations of the ND task force, the experimental floor area should be at least 42.5m x 17m and the hook height must be at least 13 m, measured from the floor. The minimum lateral dimension of hall needs further study, and will ultimately be settled in EFIG (Expt-Facility Interface Group).

The neutrino beam will be produced with protons extracted from the Fermilab Main Injector. The design proton energy ranges from 60 to 120 GeV, at a nominal power of 1.2 MW possibly upgraded to 2.4 MW. Approximately 7.5×10^{13} protons will be extracted every 1.2 seconds at 120 GeV, for an estimated total of 1.11×10^{21} pot/year, including a factor 0.57 to account for the efficiency of the accelerator complex. The spill duration will be 10 μ sec. The extracted beam will be bent downwards at the appropriate angle of 101 mrad.

With this beam parameters, the total neutrino event rate in the Near Detector (ND) will be ≈ 0.14 events/ton/spill, and the total number of ν_μ CC events/year/ton $\cong 1.6 \times 10^6$. The typical shape of the neutrino flux is compared in Fig. 4 with expected oscillations at the far detector given by $P_{\text{osc}} \sim 1$ as extracted by the up-to-date global fits for neutrino mass scales and mixing angles. The huge variation of the oscillated spectrum is due to the largely unknown value of the δ_{CP} phase.

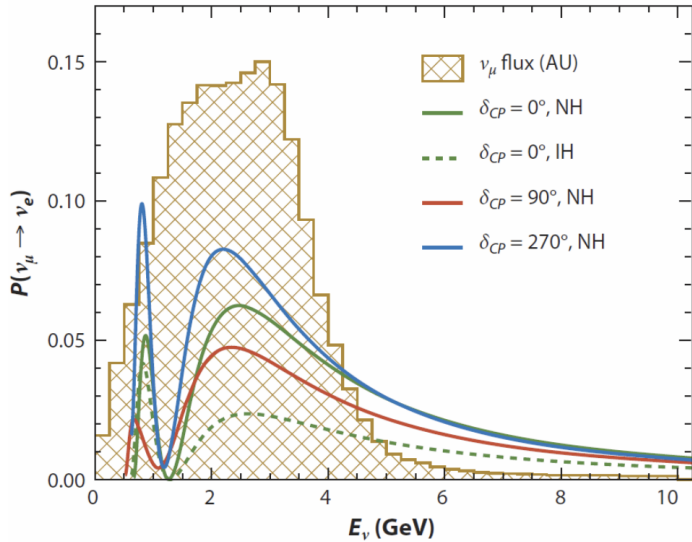


Figure 4: Comparison of the typical neutrino spectrum in DUNE with the expected oscillations in the FD for various parameter assumptions.

1.2 Requirements for the DUNE ND

The number of events for the exclusive process X (signal and backgrounds) detected in both the Near (ND) ($P_{\text{osc}} \sim 1$) and Far (FD) detectors can be written as:

$$N_X(E_{\text{rec}}) = \int_{E_{\nu}} dE_{\nu} \Phi(E_{\nu}) P_{\text{osc}}(E_{\nu}) \sigma_X(E_{\nu}) R_{\text{phys}}(E_{\nu}, E_{\text{vis}}) R_{\text{det}}(E_{\text{vis}}, E_{\text{rec}}) \quad (1)$$

where Φ is the incoming (anti)neutrino flux, σ_X the cross-section for the process X on the given nuclear target, R_{phys} the physics response function introduced by the nuclear smearing resulting in the visible final state particles, and R_{det} is the detector response function (acceptance) for the visible final state particles. E_{ν} and E_{rec} are the true and the reconstructed neutrino energies, respectively. Specifically, the variables E_{vis} and E_{rec} represent the total energy of the visible final state particles emerging from the nuclear smearing and the final reconstructed energy in the detector, respectively. Similar equations can be written for any other kinematic variable, by simply replacing the energy with the corresponding variable. The main terms in Eq.(1) are folded together into the observed event distributions and cannot be decoupled by using a single detector or nuclear target.

The energy range relevant for the oscillation analyses in DUNE corresponds to $0.5 < E_{\nu} < 10$ GeV (Fig. 4). While the sensitivity to different values of δ_{CP} increases at $E_{\nu} < 5$ GeV, the higher energy region is important for normalization purpose and the search for effects beyond PMNS oscillations. This broad energy range is particularly challenging since (anti)neutrino interactions receive significant contributions from all the main processes: $\sim 25\%$ quasi-elastic (QE), 42% resonances (RES), and 33% deep inelastic scattering (DIS). As a result, DUNE cannot be considered a simple counting experiment within a restricted energy window (like T2K), but requires an understanding of all the QE, RES, and DIS processes on an Argon nucleus, as well as their interplay at the boundary of the corresponding kinematic regions. In particular, (anti)neutrino interactions in DUNE are dominated by inelastic interactions, with about 54% of events characterized by $W > 1.4$ GeV and 43% by $W > 1.6$ GeV. The most critical region is therefore the one related to the resonance productions (at smaller W 's) and to the transition region to DIS, which is rather complex to model properly, due to the interplay of various effects including nuclear modifications, non-perturbative contributions etc. Unfortunately, the existing uncertainties in the modeling of the (anti)neutrino-nucleus cross-sections, as well as final state interactions within the nucleus are not consistent with the precision required by the DUNE oscillation analysis [12].

The FD exposures expected in DUNE imply that the oscillation analyses will benefit from relatively large event samples for most of the accessible oscillation parameters, with about 1,000 ν_e and 10,000 ν_{μ} CC events identified in the FD. To this end, a basic requirement for the analysis is that the combined systematic uncertainties must be smaller than the corresponding statistical uncertainties. Figure 5 illustrates the impact of different values of systematic uncertainties on the observed ν_e signal for the CP violation sensitivity [28]. Even a relatively small change of the relative uncertainties from 1% to 3% can potentially almost double the total exposure needed to achieve a discovery (5σ). This simple example shows that the cost of systematic uncertainties can be large in DUNE. It is therefore crucial for DUNE to design and build a capable near detector able to provide detailed in-situ constraints for all the systematic uncertainties relevant for the oscillation analysis.

The DUNE FD is based upon the LAr technology and requires the presence of dedicated Ar target(s) in the ND. The ND complex currently planned can provide detailed measurements of (anti)neutrino interactions

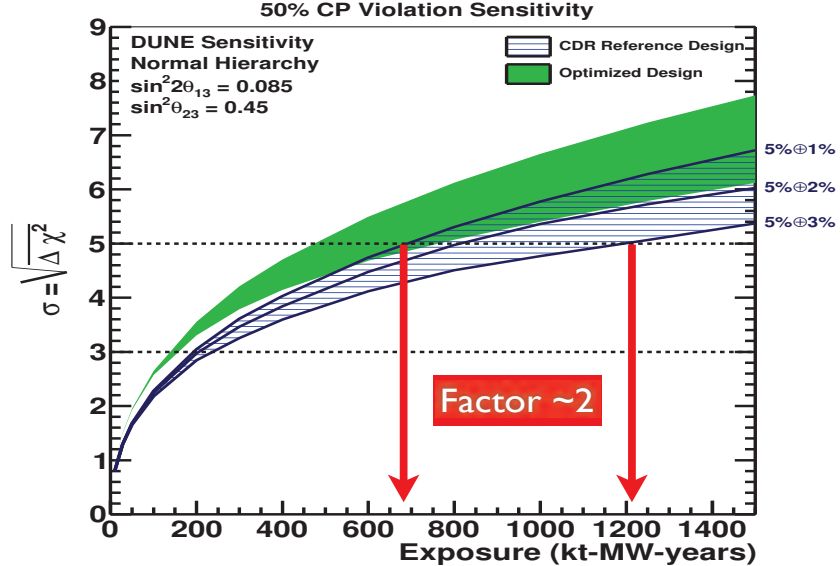


Figure 5: Impact of systematic uncertainties on the sensitivity to the CP violation search in the FD. Figure adapted from the DUNE CDR [28].

on Ar using the combination of a massive LAr TPC (~ 25 t fiducial mass) with a high pressure Ar gas TPC (HPgTPC). The first detector offers large statistics samples with a technology similar to the one used in the FD, while the second detector can detect low threshold particles (primarily protons) originated in the interactions, albeit with a limited fiducial mass. However, the use of Ar as a single nuclear target implies severe intrinsic limitations for the ND measurements. The Ar nucleus is not a good target for the flux measurements $\Phi(E_\nu)$ since it is affected by substantial nuclear effects (neutrons, final state interactions etc.). In turn, the nuclear smearing $R_{\text{phys}}(E_\nu, E_{\text{vis}})$ in Ar introduces large modifications in the reconstructed spectra, which are present even for an ideally perfect Ar detector. This smearing must be understood in order to unfold the event distributions measured in the FD and to calibrate the corresponding neutrino energy scale. Using a single Ar target in the ND complex does not allow a complete characterization of these effects since it cannot decouple the factors entering in Eq.(1). As a result, the ND measurements on Ar are affected by irreducible systematic uncertainties and, most importantly, by a relatively large reliance upon MC or model corrections.

The planned capability to move the Ar targets in the ND complex off-axis with respect to the nominal beam direction (DUNE-Prism) can certainly offer useful information to determine the reconstructed neutrino energy scale, by providing a series of known beam spectra centered around selected energy values. However, DUNE-Prism cannot be the sole handle to address the issues described above since its application in DUNE is characterized by some limitations. The main limitation is probably related to the dependence from the beam model in predicting the expected “known” beam spectra, further coupled with the model dependence associated to the use of a single Ar target. Any unexpected discrepancy between the measured event distributions in Ar and the corresponding MC predictions can potentially affect the results. Furthermore, DUNE-Prism can be affected by possible variations of the beam conditions (and detector acceptances) over time while moving in the various off-axis positions. Finally, the DUNE-Prism concept cannot provide accurate beam spectra at higher energies $E_\nu > 3.5$ GeV.

The DUNE oscillation analysis cannot rely largely on MC or model corrections to control the relevant systematics, given its ambition and the expected sensitivity. The need of a robust analysis with minimal model-dependence is particularly critical in the searches for New Physics, which must be one of the main goals of DUNE, rather than obtaining a mere parameterization of the expected PMNS oscillation matrix. To this end, an ad-hoc tuning of the MC models to wash away unexpected discrepancies is not a robust option. Without a clear strategy to constrain individually all the factors folded in Eq.(1) using in-situ data, MC corrections can introduce potential biases in the analysis. Furthermore, degeneracies and correlations represent an additional challenge for any MC tuning. An instructive example is offered by the NO ν A long-baseline oscillation experiment, which is located 14 mrad off-axis. The dominant systematic uncertainty in NO ν A arises from the neutrino energy scale. As shown in Fig. 6, large discrepancies were observed on the reconstructed hadronic energy E_{had} in the NO ν A ND. Given the impossibility to disentangle the effects of the CC interaction modeling, initial and final state nuclear effects, smearing etc. without independent measurements, a MC tuning necessarily introduces additional systematic uncertainties.

As discussed above, the use of Ar as the sole nuclear target in the ND complex results in severe limitations. While the presence of a CH plastic scintillator tracker (3DST) provides independent measurements from a different nuclear target, its resolutions are not consistent with the precisions required to resolve the factors

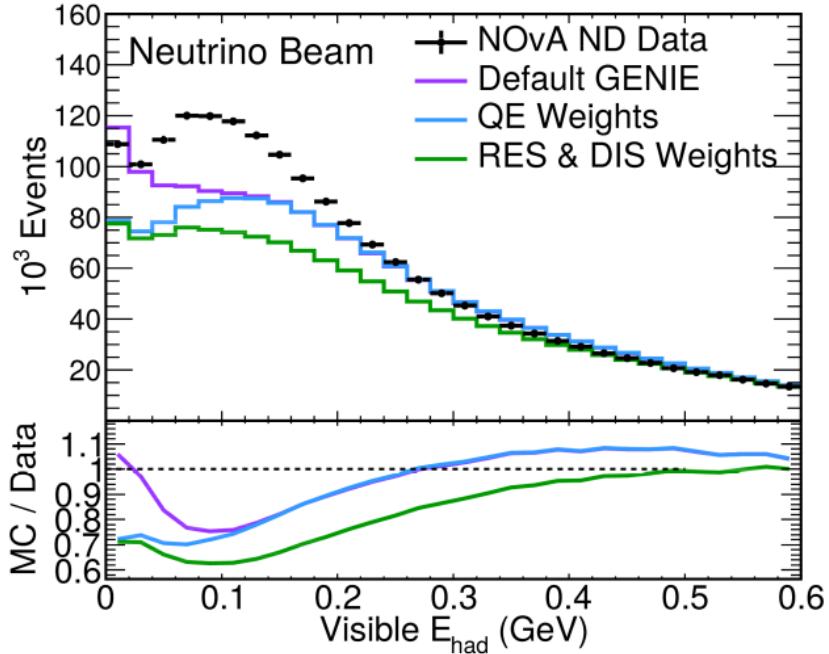


Figure 6: Observed discrepancies on the measured hadronic energy in the NO ν A ND located 14 *mrad* off-axis. See text for details.

in Eq.(1). Furthermore, there is no unambiguous way to relate measurements on the CH and Ar targets. A possible solution is the addition of another low-density spectrometer using a straw tube tracker (STT) as (anti)neutrino target and high resolution tracking detector. A key feature offered by STT is the capability to perform accurate measurements of (anti)neutrino interactions on hydrogen (free proton), in addition to various other nuclear targets. We can then exploit the synergies among different detectors to achieve more accurate predictions for the FD oscillation analysis.

2 Physics Program

2.1 Reduced Systematics for Long-baseline Oscillation Analyses

A necessary condition to constrain the systematic uncertainties relevant for the DUNE oscillation analysis is a ND complex with enough redundancy and resolution to perform the following in-situ measurements:

- $\Phi(E_\nu)$

The flux is the only factor in Eq.(1) to be easily factored out. All flux measurements benefit from/prefer detectors with: (a) low density to achieve high resolution and precise energy scales; (b) light A target(s) to minimize the impact of nuclear effects. The STT can measure the fluxes for all (anti)neutrino flavors with unprecedented accuracy thanks to the availability of a hydrogen target.

- $\sigma_X(E_\nu)$

The cross-section measurements require the same Ar target as the FD. Once all the fluxes are precisely measured by STT we can use the large statistics from the LAr and HPgTPC detectors to measure cross-sections on Ar. We note that the σ_X measurement requires the understanding of $R_{\text{phys}} R_{\text{det}}$. To this extent a full integrated detector system, with magnetic capability, neutron and proton identification, will be needed.

- $R_{\text{phys}}(E_\nu, E_{\text{vis}})$

Disentangling the physics response function from the detector acceptance R_{det} requires both Ar and lighter targets within the same detector. The STT can accurately constrain the physics response function with the use of the hydrogen target (for which $R_{\text{phys}} \equiv 1$) together with Ar and other lighter targets.

- $R_{\text{det}}(E_{\text{vis}}, E_{\text{rec}})$

The detector response for the FD can only be provided by the LAr detector in the ND complex. The impact of the differences in the readout on the detector response of ND and FD has to be evaluated and will possibly require dedicated test-beam exposures. We note that the determination of $\sigma_X R_{\text{phys}}$ in STT from a comparison of Ar and hydrogen allows an almost straightforward extraction of R_{det} in LAr.

In addition, the multipurpose magnetic and calorimetric detector, in combination with the STT, offers a synergy with the LAr detector in measuring σ_X of several exclusive processes e.g. π^0 and γ in NC and CC interactions. Conversely, the LAr detector offers a synergy validating in-situ the effect of the physics response function R_{phys} and the event predictions on Ar before the extrapolation to the FD.

In the following we will discuss in details the various measurements for the determination of the fluxes Φ and of the physics response function R_{phys} .

2.1.1 $\Phi(E_\nu)$ Measurements

A precise knowledge of the fluxes is a crucial requirement not only for the FD oscillation analysis, but also for all ND measurements. This is a necessary condition for the unfolding of the different terms in Eq.(1). Our proposal will provide a complete determination of absolute $\nu_\mu, \bar{\nu}_\mu$ and relative $\nu_\mu, \bar{\nu}_\mu, \nu_e, \bar{\nu}_e$ fluxes with an unprecedented precision:

- **Absolute ν_μ flux from $\nu e \rightarrow \nu e$ elastic.**
- **Absolute and relative $\bar{\nu}_\mu$ flux from $\bar{\nu} p \rightarrow \mu^+ n$ QE on H with $Q^2 \sim 0$.**
At $Q^2 = 0$ the QE cross-section σ_{QE} is a constant determined by neutron β -decay to a precision $\ll 1\%$. The proposed detector has an excellent efficiency for neutron detection down to low momenta.
- **Relative ν_μ and $\bar{\nu}_\mu$ fluxes vs. E_ν from $\nu(\bar{\nu})p \rightarrow \mu^\mp p \pi^\pm$ on H with $\nu < 0.5$ GeV.**
We select exclusive $\mu^\mp p \pi^\pm$ topologies from $\nu_\mu(\bar{\nu}_\mu)$ interactions on H and use the samples with $\nu < 0.5$ GeV for an accurate flux determination.
- **Relative $\bar{\nu}_\mu$ flux vs. E_ν from $\bar{\nu} p \rightarrow \mu^+ n$ QE on H with $\nu < 0.25$ GeV.**
We select the exclusive $\mu^+ n$ QE interactions on H and use the sample with small hadronic energy $\nu < 0.25$ GeV.
- **Ratio of $\bar{\nu}_\mu/\nu_\mu$ fluxes vs. E_ν from coherent π^-/π^+ .**
Measure the ratios within the same beam polarity (FHC or RHC) from coherent interactions on C (isoscalar) inside the radiator targets.
- **Ratio of ν_e/ν_μ and $\bar{\nu}_e/\bar{\nu}_\mu$ vs. E_ν from $\nu(\bar{\nu})$ CC interactions on CH₂ targets.**
These ratios are roughly independent of the target nucleus since the effect of the difference m_e vs. m_μ is negligible in the main DUNE energy range.
- **Ratio of ν_e/ν_μ and $\bar{\nu}_e/\bar{\nu}_\mu$ from $\nu(\bar{\nu})$ CC interactions on H.**
Provides an accurate constrain on the integral and an independent measurement of the shape vs. E_ν complementary to the one from radiator targets.
- **Determination of parent $\mu/\pi/K$ distributions from $\nu(\bar{\nu})$ CC on H and CH₂ at low- ν .**
This measurement is crucial to constrain in-situ the extrapolation of fluxes from the ND to the FD and requires a fit to both the ν_μ and $\bar{\nu}_\mu$ distributions.

The list of flux measurements is clearly dominated by interactions with hydrogen (free protons) and electrons. In particular, the availability of large statistics from a hydrogen target (STT) allows precisions far exceeding what is achievable with any nuclear target. It is worth mentioning that we will also have additional flux measurements using the radiator targets, providing independent cross-checks.

2.1.2 $R_{\text{phys}}(E_\nu, E_{\text{vis}})$ Constraints

In order to constrain R_{phys} in STT we need an Ar target integrated within the same detector. The Ar target in STT must be thin ($< 1X_0$) and with a geometry similar to the straw modules in order to guarantee a similar detector response R_{det} with respect to the lighter targets.

Once the fluxes are precisely measured in STT (Sec. 4.1), we are left with the convolution of the three terms $\sigma_X R_{\text{phys}} R_{\text{det}}$ in Eq.(1). The unfolding of $\sigma_X R_{\text{phys}}$ requires comparisons between the Ar target and the lighter target(s) integrated within STT (same R_{det}). To this end, a key role is played by the hydrogen target for which $R_{\text{phys}} \equiv 1$.

Given the large expected statistics we can accurately measure the cross-sections σ_X on hydrogen (flux is known from STT). Since $R_{\text{phys}} \equiv 1$ for hydrogen, the unfolding of the neutrino energy E_ν only depends on the detector response R_{det} , which is essentially defined by the $\delta p/p$ (calibrated to 0.2% from the K_0 mass peak). From a comparison of Ar interactions in STT we can therefore determine the product $\sigma_X R_{\text{phys}}$ on Ar in STT. Alternatively, we can determine the product of R_{phys} times the ratio of cross-sections in Ar and hydrogen. This latter quantifies the nuclear modifications of cross-sections in Ar.

Since final state interactions (FSI) in Ar largely modify the visible final state topologies, we need to initially use the inclusive CC samples in Ar and H to obtain the product $\sigma_X R_{\text{phys}}$. The inclusive samples effectively integrate over all visible topologies resulting in the actual average smearing for CC interactions. It is worth noting that the knowledge of $\sigma_X R_{\text{phys}}$ allows to directly extract and calibrate the detector response R_{det} in the LAr detector from the corresponding Ar interactions.

In order to constrain R_{phys} separately from σ_X in STT we define a complete set of kinematic variables (i.e. corresponding to the 5 degrees of freedom associated to the hadron and lepton vectors) sensitive to the effect of the nuclear smearing. Using the same inclusive CC samples, we then compare the observed distributions of such kinematic variables from events in Ar and H targets.

The measurement strategy outlined above can determine the nuclear smearing for the particular ND beam spectrum. The use of a complete set of kinematic variables sensitive to the smearing can constrain the physics response function and help resolving potential degeneracies. This latter point is particularly relevant given the fact that in the FD we will have a different beam spectrum. Additional handles to resolve potential degeneracies in the nuclear smearing include the following:

- Comparisons of H and Ar interactions in bins of muon variables (p_μ, θ_μ);
- Comparisons of H and Ar interactions in bins of the radial distance from the beam axis provide a variation of the input spectra;
- Analyze different exclusive topologies ($\mu p\pi$, etc.) in both H and Ar;
- Simultaneous analysis of ν and $\bar{\nu}$ to gather information about ν -n (isospin symmetry);
- Selection of Ar events with a total charge at the primary vertex $C_{\text{vtx}} = 0$ for neutrinos and $C_{\text{vtx}} = +1$ for antineutrinos to check the impact of n and p interactions.

The various comparisons between events from Ar and H targets in STT can be further used to constrain and tune the available models/inputs. Results can then be compared with similar analyses of Ca and C targets in STT.

The determination of $\sigma_X R_{\text{phys}}$ for Ar in STT and the constraints of R_{phys} can finally be compared in-situ with the large statistics of interactions collected in the LAr detector. As noted above, this comparison allows the unfolding of the detector response R_{det} in LAr, as well as a validation of Ar predictions from the ND before the extrapolation to the FD oscillation analysis.

2.2 Physics Facility for Precision Measurements and Searches

The collection of the statistics shown in Tab. 2 and the determination of the neutrino and antineutrino fluxes to unprecedented precision using $\nu(\bar{\nu})$ -H interactions (Sec. 4.1) would solve the two main limitations of past neutrino experiments. We can then exploit the unique properties of the (anti)neutrino probe for the study of fundamental interactions with a broad program of precision measurements and searches [24] complementary to the ongoing efforts in the collider, fixed-target and nuclear physics communities. In this Section we outline a few examples of measurements part of this broader program, which for the most part is unique to the proposed detector.

2.2.1 Electroweak Precision Measurements

The interest of a precise determination of the weak mixing angle ($\sin^2 \theta_W$) in (anti)neutrino scattering at the DUNE energies is twofold: (a) it provides a direct measurement of neutrino couplings to the Z boson and (b) it probes a different scale of momentum transfer than LEP did by virtue of not being at the Z boson mass peak.

The most precise measurement of $\sin^2 \theta_W$ in neutrino deep inelastic scattering (DIS) comes from the NuTeV experiment, which reported a value that is 3σ from the Standard Model [82]. The proposed addition to the DUNE ND complex can determine $\sin^2 \theta_W$ from the ratio of NC and CC DIS interactions induced by neutrinos $\mathcal{R}^\nu \equiv \sigma_{\text{NC}}^\nu / \sigma_{\text{CC}}^\nu$. A cut on the visible hadronic energy $E_{\text{had}} > 5$ GeV (the CHARM experiment used $E_{\text{had}} > 4$ GeV) is used to harden the Q^2 distribution. With an exposure of 5 years with the CP optimized beam and 2 years with the ν_τ optimized beam about 4×10^6 NC events are expected with this cut. The use of the high resolution STT significantly reduces the experimental systematic uncertainties compared to much coarser detectors like NuTeV. Two key advantages are the efficient identification of ν_e CC interactions and an event-by-event kinematic analysis separating NC and CC interactions.

The measurement of \mathcal{R}^ν will be dominated by theoretical systematic uncertainties [9, 18, 52, 53, 51] on the structure functions of the target nucleons. Assuming modest improvements over the NuTeV analysis it seems feasible to achieve a total relative uncertainty on the value of $\sin^2 \theta_W$ extracted from νN DIS of 0.35%. We note that most of the model uncertainties will be constrained by dedicated in situ measurements using the large CC samples and employing improvements in theory that will have evolved over the course of the experiment.

A second independent measurement of $\sin^2 \theta_W$ can be obtained from NC $\nu_\mu e$ elastic scattering. This channel is free from hadronic uncertainties but it is limited by the statistics due to its tiny cross section. The value of $\sin^2 \theta_W$ can be extracted from the ratio $\mathcal{R}_{\nu e}(Q^2) \equiv \sigma(\bar{\nu}_\mu e \rightarrow \bar{\nu}_\mu e) / \sigma(\nu_\mu e \rightarrow \nu_\mu e)$ [58], in which systematic uncertainties related to the selection and the electron identification cancel out. The required fluxes are measured using $\nu(\bar{\nu})$ -H (Sec. 4.1) and coherent π^\pm interactions. The proposed detector can select $\nu_\mu e$ elastic events with little backgrounds, which, most importantly, can be calibrated in-situ with data. In order to increase the available statistics we can perform a combined analysis of the events collected in STT and in the large LAr detector (fiducial volume of about 25 tons) present within the ND complex. The STT reduces systematic uncertainties while the LAr increases the statistics. An overall relative precision of $\sin^2 \theta_W$ from ν -e of 1% or better seems feasible.

The DIS and ν -e elastic channels are characterized by substantially different scales of momentum transfer, providing a tool to test the running of $\sin^2 \theta_W$ in a single experiment. To this end, another interesting channel is the NC elastic scattering off protons (Sec. 2.2.3) in which the Q^2 can be reconstructed and has

scales intermediate between ν and DIS. Another channel is the coherent ρ production through the ratio $\mathcal{R}_\rho \equiv (\nu_\mu \mathcal{A} \rightarrow \nu_\mu \rho^0 \mathcal{A}) / (\nu_\mu \mathcal{A} \rightarrow \mu^- \rho^+ \mathcal{A})$. Electroweak parameters including $\sin^2 \theta_W$ and the couplings can be extracted from a global fit including all the different channels measured, similarly to what was done at LEP.

2.2.2 Tests of Isospin Physics and Sum Rules

A compelling physics topic with the proposed detector is isospin physics using both neutrino and antineutrino interactions. The availability of large samples of $\nu(\bar{\nu})$ -H interactions [39] allows a precision test of the Adler sum rule [8], $S_A = 0.5 \int_0^1 dx/x (F_2^{\bar{\nu}p} - F_2^{\nu p}) = I_p$, which gives the isospin of the target and was tested only by BEBC [11] with a few thousand events. The Adler sum rule survives the strong-interaction effects because of the conserved vector current (CVC) and provides an exact relation to test the local current commutator algebra of the weak hadronic current. In the quark-parton model the Adler sum is the difference between the number of valence u and d quarks of the target. The value of S_A can be measured as a function of the momentum transfer Q^2 from the structure functions $F_2^{\bar{\nu}p}$ and $F_2^{\nu p}$ determined from the corresponding differential cross-sections on hydrogen. This measurement is sensitive to possible violations of the isospin (charge) symmetry, heavy quark (charm) production, and strange sea asymmetries $s - \bar{s}$. Furthermore, the measurement from H can be compared with the values of S_A obtained from the C target ($S_A = 0$) [52, 53, 51].

The Gross-Llewellyn-Smith (GLS) sum rule [46] $S_{GLS} = 0.5 \int_0^1 dx/x (x F_3^{\bar{\nu}p} + x F_3^{\nu p})$ can also be measured precisely as a function of Q^2 using $\nu(\bar{\nu})$ -H interactions. The value of S_{GLS} in the quark-parton model gives the number of valence quarks in the nucleon. This sum rules receives both perturbative and non-perturbative QCD corrections and its Q^2 dependence can be used to extract the strong coupling constant $\alpha_s(Q^2)$. The most precise measurement of S_{GLS} was performed by CCFR on a Fe target at $Q^2 = 3$ GeV 2 . The presence of both H and various nuclear targets in STT would allow an investigation of the isovector and nuclear corrections, adding a tool to test isospin (charge) symmetry.

The isospin symmetry implies that $F_{2,3}^{\bar{\nu}p} = F_{2,3}^{\nu p}$ and that for an isoscalar target $F_{2,3}^{\bar{\nu}} = F_{2,3}^\nu$. In the proposed detector we can perform various precision tests of isospin (charge) symmetry exploiting the unique combination of H and nuclear targets A. In particular, we can measure two structure function ratios as a function of Q^2 and Bjorken x : $R_{2,3}^H \equiv F_{2,3}^{\bar{\nu}p}/F_{2,3}^{\nu p} = F_{2,3}^{\bar{\nu}n}/F_{2,3}^{\nu n}$ and $R_{2,3}^A \equiv F_{2,3}^{\bar{\nu}A}/F_{2,3}^{\nu A} - 1 = \Delta F_{2,3}^{\bar{\nu}-\nu}/F_{2,3}^\nu$, in which many systematic uncertainties cancel out. Since these ratios are sensitive to charm quark effects though the Cabibbo angle $\sin^2 \theta_C$ and strange sea asymmetry $s - \bar{s}$ a combined analysis with charm production (Sec. 2.2.3) is needed. We can use three possible nuclear targets C, Ca, and Ar in order to disentangle nuclear effects from isospin effects in nucleon structure functions.

2.2.3 Measurements of the Strangeness Content of the Nucleon

The strange quark contribution to the vector and axial-vector currents of the nucleon, as well as to the nucleon spin, Δs , are important elements to improve our understanding of the nucleon structure. While the strange quark vector elastic form factors have been measured with good accuracy in parity-violating electron scattering (PVES) experiments, the strange axial-vector form factors are still poorly determined. The proposed detector can accurately determine the latter from a measurement of the NC elastic scattering off protons $\nu_\mu(\bar{\nu}_\mu)p \rightarrow \nu_\mu(\bar{\nu}_\mu)p$. In the limit $Q^2 \rightarrow 0$ the NC differential cross-section is proportional to the axial-vector form factor $d\sigma/dQ^2 \propto G_1^2 = (-G_A/2 + G_A^s/2)^2$, where G_A is the known axial form factor and G_A^s is the strange form factor. This process provides the most direct measurement of Δs by extrapolating the NC differential cross-section to $Q^2 = 0$ since in this limit $G_A^s \rightarrow \Delta s$.

We can measure the ratios of NC elastic scattering to the corresponding QE process $\mathcal{R}_{\nu p}(Q^2) \equiv \sigma(\nu_\mu p \rightarrow \nu_\mu p)/\sigma(\nu_\mu n \rightarrow \mu^- p)$ and $\mathcal{R}_{\bar{\nu}p}(Q^2) \equiv \sigma(\bar{\nu}_\mu p \rightarrow \bar{\nu}_\mu p)/\sigma(\bar{\nu}_\mu p \rightarrow \mu^+ n)$ over an extended Q^2 range, using the CC QE process to determine G_A . This latter can also be used to extract the axial current charge radius, which can be compared to the results from muon capture in hydrogen to investigate existing discrepancies on this quantity [48]. The QE process $\bar{\nu}p$ can be measured both with hydrogen and nuclear targets. With the statistics in Tab. 2 we expect to detect $\mathcal{O}(10^6)$ events in STT from NC elastic off proton for both ν_μ and $\bar{\nu}_\mu$. In addition, a combined analysis with PVES data (HAPPEX, G0, A4) would allow an accurate determination of all three strange form factors G_E^s, G_M^s, G_A^s .

The resolution of the proposed detector will enable precision measurements of exclusive decay modes of charmed hadrons (e.g., D^{*+}, D_s, Λ_c) and measurement of charm fragmentation and production parameters. In addition, the low density of STT will give access to both the $\mu\mu$ and μe inclusive semi-leptonic charm decay channels with a statistics more than one order of magnitude higher than the largest sample of charm dimuon events available from NOMAD [69]. The analysis of both neutrino and antineutrino induced charm production provides the most direct determination of the strange quark content of the nucleon [10].

2.2.4 Nucleon Structure and QCD Studies

The precise calibration of the energy scale uncertainties in the proposed detector and the unprecedented precision in the determination of the (anti)neutrino fluxes (Sec. 4.1) allow measurements of structure functions and cross-sections with accuracies comparable to electron scattering experiments. Using both neutrino and antineutrino DIS we can determine the different structure functions F_2, xF_3, F_L, F_T , elucidating the flavor

structure of the nucleon [10]. We can perform global QCD analyses of (anti)neutrino data from the proposed detector to study parton distribution functions (PDFs) as well as perturbative and non-perturbative corrections (High Twists) in a broad range of Q^2 and Bjorken x , given the statistics (Tab. 2) and energies available in DUNE. Data from both H and the various nuclear targets can be used to separate valence and sea quark distributions, d and u quark distributions, and the strange quark s and \bar{s} distributions. A study of F_L will not only provide information on the gluon distribution (e.g. Altarelli-Martinelli relation) but also a determination of $R = F_L/F_T$, which is expected to have a different behavior at small Q^2 with respect to electromagnetic interactions [52, 53, 51] as a result of the partial conservation of the axial current (PCAC). All of these studies of the nucleon structure in the proposed detector can provide unique information, complementary to the ongoing programs at colliders and fixed-target electron DIS experiments.

The availability of large statistics samples of $\nu(\bar{\nu})$ -H interactions (Tab. 2) is crucial to study the structure of the nucleon disentangling nuclear effects. In particular, using the isospin symmetry we can obtain a direct model-independent measurement of the free neutron structure functions $F_{2,3}^{\nu n} \equiv F_{2,3}^{\bar{\nu} p}$ and $F_{2,3}^{\bar{\nu} n} \equiv F_{2,3}^{\nu p}$. All other determinations from charged lepton DIS suffer from various model systematic uncertainties, typically growing with Bjorken x . This measurement allows, in turn, a precise determination of the d quark distribution and of the corresponding d/u ratio up to values of Bjorken x close to 1, testing various model predictions for the limit at $x \rightarrow 1$.

The measurement of QE and resonance production on hydrogen allows precision measurements of elementary amplitudes and form factors [47]. A determination of the axial current charge radius from $\bar{\nu}p$ QE can be compared with the results from muon capture in hydrogen to investigate existing discrepancies [48] and test μ - e universality. The available QE statistics can be used to test radiative corrections to neutron and nuclear β decay and possible violations of CKM unitarity [71]. Single photon NC processes which could provide potential backgrounds for the MiniBooNE anomaly [47] can be measured.

2.2.5 Studies of (Anti)Neutrino-Nucleus Interactions

The possibility to integrate various thin nuclear targets within STT (Sec. 3.3.1) allows detailed studies of the nuclear structure and the related nuclear effects on structure functions, form factors, and cross-sections. An important issue is how the structure of a nucleon is modified when said nucleon is inside the medium of a heavy nucleus, including the determination of nuclear PDFs as well as non-perturbative effects. The study of final state interactions (FSI) is also relevant as FSI can introduce a substantial smearing of the kinematic variables reconstructed from the observed final-state particles. The flavor separation provided by the weak current and the availability of nuclear targets with the same atomic weight like Ar and Ca would clarify the flavor dependence of nuclear effects. All of these nuclear physics measurements offer unique and complementary information to the existing programs at JLab, heavy-ion, and electron-ion colliders.

A comparison between interactions on H and on the various nuclear targets available in STT can provide a direct model-independent measurement of nuclear effects. In particular, the isospin symmetry provides a determination of the free neutron structure function and hence the one of the average isoscalar nucleon $F_{2,3}^{\nu N} \equiv (F_{2,3}^{\nu p} + F_{2,3}^{\bar{\nu} p})/2$. We can then obtain the first direct measurement of the nuclear ratios $R_A \equiv F_{2,3}^{\nu A}/F_{2,3}^{\nu N}$. An interesting issue to study, in addition to the flavor dependence of nuclear effects, is the role of the axial-vector current and the corresponding differences with electromagnetic interactions. The precision achievable with the proposed detector can clarify the many outstanding discrepancies observed among different existing measurements, as well as with various theoretical models.

2.2.6 Searches for New Physics

The precision tests of fundamental interactions described in the previous Sections are sensitive to various new physics Beyond Standard Model (BSM), which would manifest as unexpected deviations from the SM predictions in the measured quantities. A complementary approach offered by the proposed detector is through many direct searches.

The excellent electron identification capability and resolution of STT offer a way to test the MiniBooNE low-energy anomaly with a different detector and at a different energies but similar L/E . To this end, several measurements are possible searching for anomalies in all the four spectra from $\nu_\mu, \bar{\nu}_\mu$ CC (disappearance) and $\nu_e, \bar{\nu}_e$ CC (appearance). Various explanations for the MiniBooNE anomaly can be tested including both SM and BSM physics. Oscillations with sterile neutrinos can be detected using both the CC ratios $\mathcal{R}_{e\mu}(L/E) \equiv (\nu_e N \rightarrow e^- X)/(\nu_\mu N \rightarrow \mu^- X)$ and $\bar{\mathcal{R}}_{e\mu}(L/E) \equiv (\bar{\nu}_e N \rightarrow e^+ X)/(\bar{\nu}_\mu N \rightarrow \mu^+ X)$ and the NC/CC ratios $\mathcal{R}_{\nu p}$ and $\mathcal{R}_{\bar{\nu} p}$ (Sec. 2.2.3) as a function of L/E . These latter provide additional handles to distinguish between appearance and disappearance. In addition, since the STT design is based upon the NOMAD concept, it provides an excellent sensitivity to ν_τ appearance [20] as a result of either oscillations with sterile neutrinos or non-standard interactions (NSI).

The proposed detector can further enhance the sensitivity of the ND complex to searches for Dark Sector physics including heavy sterile neutrinos (e.g. Majorana singlet fermions in ν MSM models), axion-like particles, dark photons, light (sub-GeV) dark matter, etc.

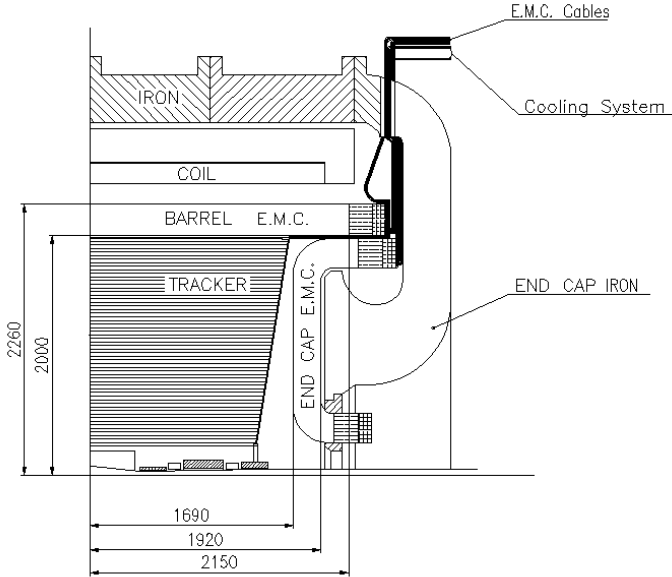


Figure 7: Vertical cross section of the KLOE detector.

3 Detector description

The proposed design aims to realize a multipurpose compact and movable detector, capable of precision tracking and calorimetry and able to detect events of different target materials including Hydrogen and Argon. The existing KLOE magnet and electromagnetic calorimeter will be complemented with an high precision internal tracker based on the straw tube technology. Even a small LAr volume could be added for inter-calibration in the extended ND detector system. *Sergio*

3.1 The KLOE magnet

The ND employs an existing superconducting magnet successfully operated at INFN-LNF for the KLOE experiment. The magnet [73] is designed in conjunction with its iron yoke to produce 0.6 T over a 4.3 m long, 4.8 m diameter volume. The coil is operated at a nominal current of 2902 A and the stored energy is 14.32 MJ [61]. The coil is located inside a cryostat (outer diameter: 5.76 m, inner diameter: 4.86 m, overall length: 4.40 m) positioned inside the return yoke, as shown in Fig. 7, and the overall cold mass is \sim 8.5 tons. The mass of the KLOE return yoke is 475 tons.

The cooling of the coil is performed by thermo-siphoning cycles: gas Helium at 5.2 K is injected at 3 bar (absolute pressure) from the cryogenic plant and liquefied through Joule-Thomson valves into a liquid Helium reservoir in thermal contact with the coil. The current leads are directly cooled by the liquid Helium while the radiation shields are cooled by gas-He at 70 K from the cryogenic plan. The heat loads are, respectively:

- 5.5 W at 4.4 K for the magnet coil
- 0.6 g/s of liquid He for the current leads
- 530 W at 70 K for the thermal radiation shields

The coil, cryostat and cryogenic system were developed by Oxford Instruments A.T.G., UK. In particular, the coil support cylinder is a rolled and welded cylinder in 5083 aluminium with cooling channels welded to the outside. The coil is a single conductor layer wound on edge using a pre impregnated insulating tape. The conductor is a composite consisting of a (Nb-Ti) Rutherford cable co-extruded with high purity aluminium. Fig. 8 shows a picture of the KLOE Magnet in the Assembly Hall before the installation in DAΦNE.

The solenoidal longitudinal field component as measured in the KLOE installation phase is plotted in Fig. 9 and compared with simulation (MAGNUS Monte carlo program) [27].

3.2 The KLOE EM calorimeter

The KLOE electromagnetic calorimeter [7] is a lead-scintillating fiber sampling calorimeter. Scintillating fibers offer high light transmission over several meters, sub-ns timing accuracy and very good hermeticity. The barrel calorimeter (see Fig. 7) is cylindrical and is located inside the KLOE magnet, close to the coil cryostat. Two additional calorimeters (end-caps) ensure hermeticity along the magnet end-caps.

The nearly-cylindrical barrel (Fig. 11) consists of 24 modules; 4.3 m long, 23 cm thick and trapezoidal cross-section, with bases of 52 and 59 cm. Each end-cap consists of 32 vertical modules 0.7 \rightarrow 3.9 m long



Figure 8: The KLOE magnet in the LNF assembly hall.

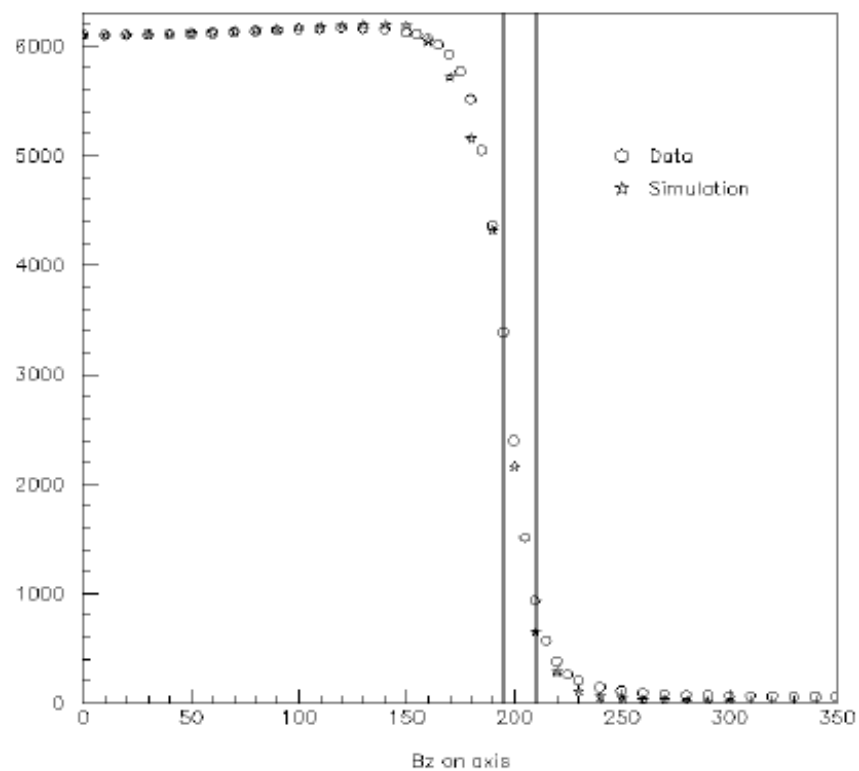


Figure 9: KLOE solenoid longitudinal field component (in Gauss) along the magnetic axis.



Figure 10: Light guides at one end of a barrel module before the installation of the photo-tubes.

and 23 cm thick. Their cross-section is rectangular, of variable width. Modules are bent at the upper and lower ends to allow insertion into the barrel calorimeter and also to place the phototube axes parallel to the magnetic field. Due to the large overlap of barrel and end-caps, the KLOE calorimeter has no inactive gap at the interface between those components. All modules are stacks of about 200 grooved, 0.5 mm thick, lead foils alternating with 200 layers of cladded 1 mm diameter scintillating fibers, glued together with a special epoxy compatible with the fiber materials.

Light guides that match almost square portions of the module end-faces to circular photo-cathodes are employed to read both ends of each module. The read-out subdivides the calorimeter into five planes in depth. The first four planes are 4.4 cm deep, the last plane is 5.2 cm deep. Each plane is subdivided in the transverse direction into 4.4 cm wide elements, except at the edges of the trapezoidal modules.

The read-out segmentation gives an $r - \phi$ or $x - z$ read-out resolution of 1.3 cm ($4.4/\sqrt{12}$ cm). A particle crossing the calorimeter deposits energy in at least five read-out regions or cells. The calorimeter weight is about 100 tons and the readout system includes 4880 photo-tubes. The energy and time resolution of the calorimeter was evaluated in the commissioning and running phases of KLOE and amounts to

- Energy resolution: $\sigma/E = 5\%/\sqrt{E(\text{GeV})}$
- Time resolution: $54/\sqrt{E(\text{GeV})}$ ps

The light readout system of one barrel module is shown in Fig. 10. The layout of the calorimeter inside the KLOE magnet is depicted in Fig. 11.

3.3 Inner Tracker

The primary goals of the inner tracker are twofold: offer a target for (anti)neutrino interactions and provide a tracking system able to accurately reconstruct the momenta of all charged particles. The detector requirements to fulfill the physics needs of the long-baseline oscillation analysis discussed in Sec. 2.1 include: (a) low density and high track sampling to guarantee momentum, angular, and space high resolutions; (b) total thickness comparable with the radiation length to minimize secondary interactions; (c) capability to accommodate various target materials; (d) particle identification for $e^\pm, \pi^\pm, K^\pm, p, \mu^\pm$; (e) fiducial target mass of ~ 5 tons. The main design parameters can be directly derived from these requirements.

All detectors for neutrino interactions suffer from a tension between the opposing requirements of a large target mass versus the detector resolution necessary to achieve the physics goals. Furthermore, in most fine-grained neutrino detectors the active detector, consisting of several different materials, also provides the target mass. A drawback of this configuration is the difficulty to precisely control the target chemical composition and size, limiting the ultimate precision achievable in the measurements. A solution to these outstanding issues is offered by the reference ND design described in the DUNE Conceptual Design Report [29]. The neutrino targets are physically separated from the actual tracking system, which has a negligible overall mass compared to the former. In order to achieve high resolution measurements, the target mass is spread out uniformly throughout the entire tracking volume, by keeping the average density low enough to have a detector transparent (about one radiation length X_0) to final state particles produced in neutrino interactions.

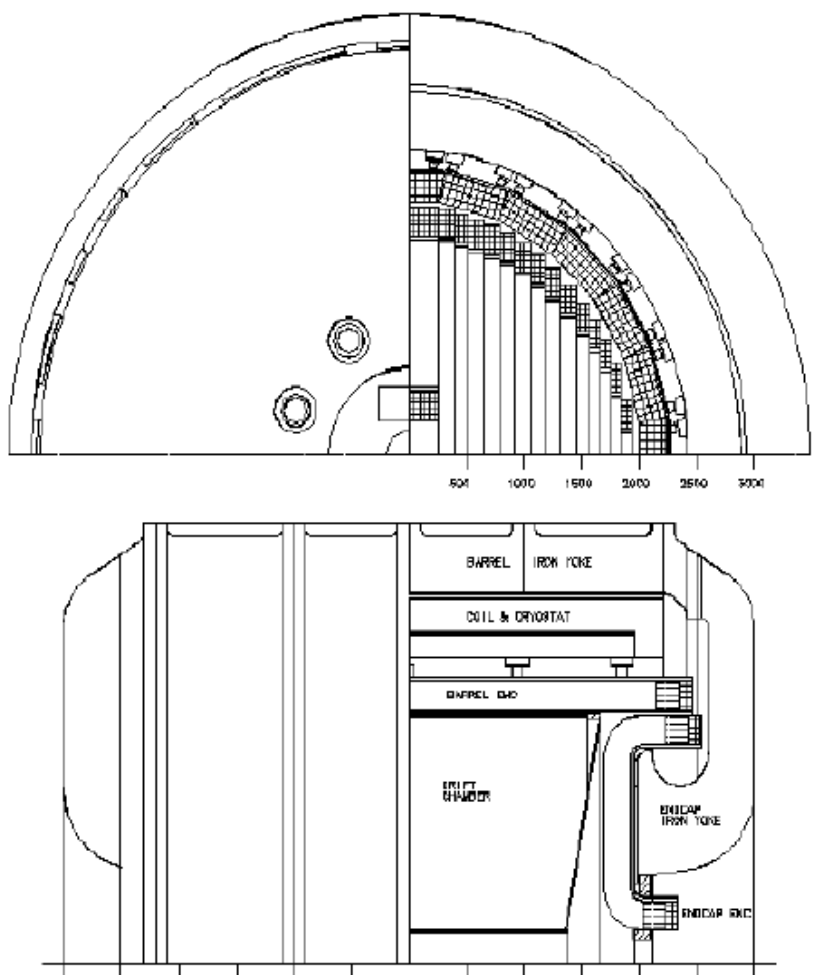


Figure 11: Front (top figure) and side (bottom figure) view of the calorimeters showing the light guides and their location inside the KLOE magnet. Units are in mm.

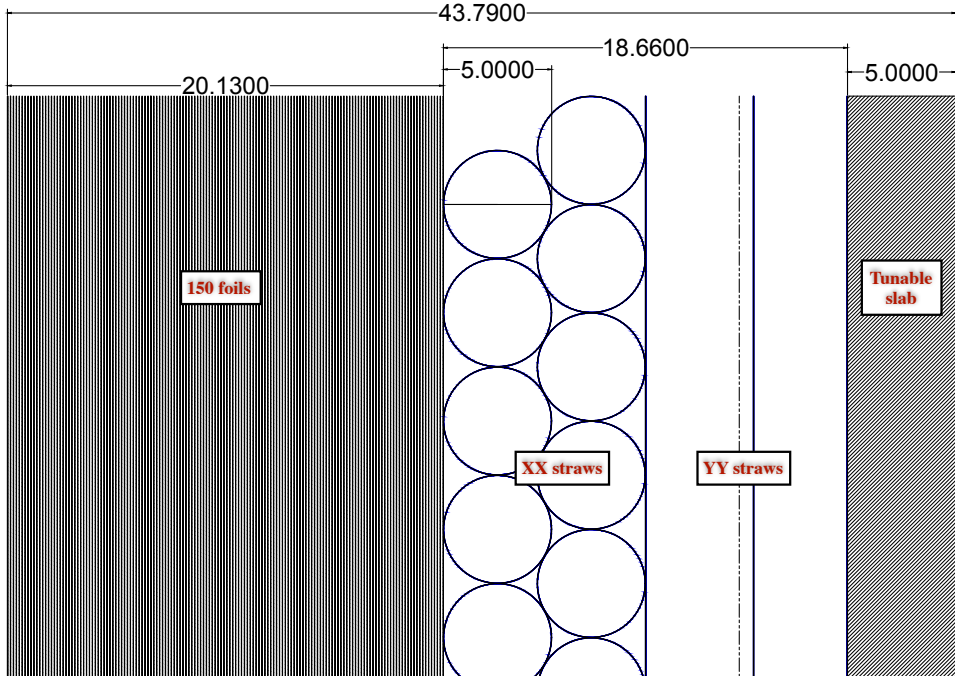


Figure 12: Drawing of a default compact STT module including three main elements (left to right): (a) a radiator with 150 polypropylene foils for e^\pm ID; (b) four straw layers XXYY; (c) a tunable polypropylene CH_2 target. The radiator and plastic target are removed for modules to be equipped with nuclear targets.

3.3.1 Straw Tube Tracker

The key detector element is a central Straw Tube Tracker (STT), which is inserted into the available magnetic volume inside the KLOE magnet. The conceptual design is a compact version of the CDR reference ND, resulting in an overall reduction of the tracking volume by close to 50%, while still retaining the same physics performance and fiducial mass. The base tracking technology is provided by low-mass straws similar to the ones used in many modern experiments for precision physics or the search for rare processes [72, 17, 64, 55]. Thin layers of various target materials (100% chemical purity) are alternated with straw layers so that they represent more than 95% of the total detector mass (less than 5% being the mass of the straw tracker). This feature, combined with the excellent vertex, angular, momentum, and timing resolutions are key factors to correctly associate neutrino interactions to each target material, as well as for an accurate measurement of the four-momenta of the final state particles. The main parameters of the proposed STT are the following: magnetic field $B = 0.6$ T, average density $\rho \sim 0.17 \text{ g/cm}^3$, radiation length $X_0 \sim 2.5$ m, tracking sampling 0.15 (0.36)% $X_0 \perp (\parallel)$. The corresponding STT modules are based upon a compact design (Fig. 12) resulting in a total width of 43.8 mm:

- The straws can be fabricated with either the ultrasonic welding or the traditional winding technologies [54]. Each module includes four straw layers XXYY glued together, with straw diameter 5 mm, mylar walls with total thickness 20 μm and 1000 Angstroms Al coating, tungsten wire with 20 μm diameter.
- The four straw layers are preceded by a radiator composed of 150 polypropylene CH_2 foils 15 μm thick, interspaced by 120 μm air gaps (Fig. 13). The configuration of the radiator is optimized for the e/π separation using Transition Radiation (TR), as discussed in Sec. 5.2.
- A solid polypropylene CH_2 target slab follows the four straw layers. The thickness of this slab, 5 mm, can be tuned in order to achieve the desired target mass and detector density.
- Both the radiator and the CH_2 target slab are removable without affecting the functionality and mechanical stability of the STT module.
- The default gas mixture for modules equipped with radiators is Xe/CO₂ 70/30 operated with an internal pressure of about 1.9 atm (Sec. 5.2).

Various thin nuclear targets can be integrated into a STT module after removing the radiator and the polypropylene target slab:

- The most important nuclear target material is graphite (pure C) for the direct measurement of the C background in the selection of hydrogen interactions (Sec. 6.1) [39]. Each graphite target is provided by a 4 mm plate mounted in front of a four layer XXYY straw assembly. The thickness of the graphite plates is tuned to match the same fraction of X_0 as the combined CH_2 radiator and target slab present in standard STT modules (Fig. 14). Modules equipped with graphite plates are interleaved throughout

the CH_2 modules in order to guarantee the same detector acceptance for CH_2 and C targets. The total fiducial mass of graphite exceeds 500 kg [39].

- Another important nuclear target is Ca, which will be installed as thin plates within the upstream modules similar to the ones used for the graphite targets (Fig. 14). The Ca target has the same atomic weight as Ar but is isoscalar, allowing a complete characterization of the $A = 40$ nucleus, as well as various measurements related to isospin physics.
- Additional nuclear targets can be installed upstream (e.g. Fe, Pb, etc.), depending upon the specific nuclear measurements requested by the community. The configuration of the various nuclear targets could also be changed for part of the exposure. To this end, STT offers a general purpose facility for precision nuclear measurements.
- A thin cryogenic (Ar) liquid target ($< 1X_0$) is added in front of the STT assembly, as discussed in Sec. 3.3.2.
- The default gas mixture used for STT modules equipped with nuclear targets (without radiator) is Ar/ CO_2 70/30 with an internal pressure of about 1.9 atm.

The STT and related nuclear targets fill the entire magnetic volume of the KLOE magnet, which roughly corresponds to a total tracking volume of 42.5 m^3 . Most of the target mass is located either in the radiator foils or in the integrated nuclear target(s), which can be fine tuned to achieve the desired fiducial mass and resolutions. The mass of the radiator targets in the default configuration corresponds to more than 95% of the total mass of the STT modules. The default target configuration includes 82 STT modules with radiators and CH_2 targets interleaved (every 9 radiator modules) with 9 STT modules with graphite targets. Assuming a fiducial cut of 20 cm from the edge, this geometry corresponds to a total fiducial mass of about 4.7 tons of CH_2 targets, out of which about 677 kg of hydrogen, and 528 kg of graphite targets. All physics sensitivity studies are based upon this configuration [39].

The support frames of the STT modules have to satisfy opposite requirements. They have to provide primarily a mechanical support for the straws and the anode wires with adequate stiffness against deformations. However, they also have to add minimal mass to the overall material budget of the STT in order to avoid significant degradations of the ECAL energy resolution and performance. A compromise is offered by the U-shaped C-composite beams shown in Fig. 15. The initial design is based upon 60 mm \times 6 mm beams at each side of the STT modules, resulting in an average amount of material crossed by the particles of a few percent of X_0 . Assuming a wire tension of about 50 g and a pre-tension of the straw walls of about 100 g each, we obtain a total load of about 233 kg for the longest horizontal beam (at the center of the solenoid) 4 m long. The maximal load in the central point of the U-beam (~ 116 kg) by splitting between the two end frames is expected to result in deflections well below 1 cm (Young's modulus of ~ 150 GPa). This result seems adequate, although more detailed studies with finite-element analysis are required.

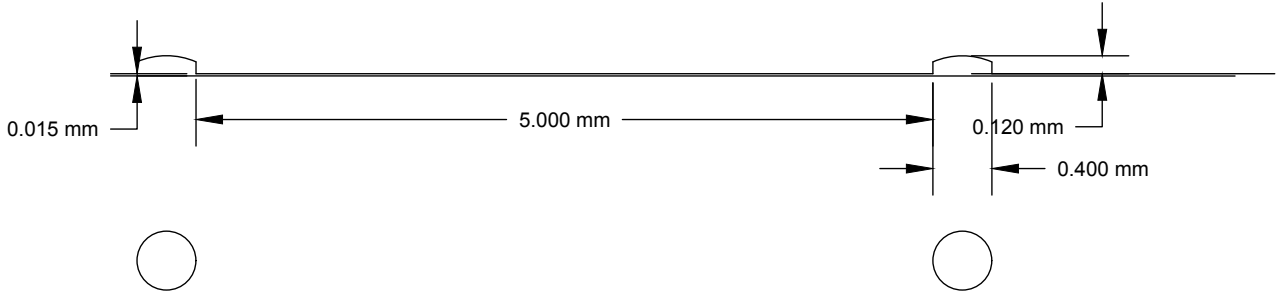


Figure 13: Drawing of one polypropylene CH_2 radiator foil showing the embossed pattern to keep the spacing between consecutive foils.

The core technology required to build STT is well established and we do not anticipate the need of major detector R&D. The conceptual design is similar to the ATLAS TRT [2, 3, 4] and COMPASS [26, 67] straw trackers. Low mass straws have been successfully developed for various modern projects including NA62 [72], COMET [64], SHiP [17], and Mu2e [55]. All the components required to build the STT can be manufactured industrially by vendors to be assembled into the final STT modules at the project production centers. Furthermore, the proposed STT is an evolution of the tracker from the reference ND design in the DUNE CDR [29]. As such, its design, cost and schedule successfully passed the technical design review (May/15) of the DUNE ND, the Director's CD1 Review (June/15) of LBNF/DUNE, and the DOE CD1-review (Jul/15) of LBNF/DUNE [32, 30, 31]. The outcome of the technical design review was positive: excerpts from the final report include: “The reference design of a straw based system is a good choice” [...] “The design is mature enough to move from the conceptual design to the preliminary design phase” [...] “an excellent team is in place to design and construct this detector” (Recommendations: none) [32]. Similar positive outcomes resulted from the following Director’s CD-1 review (“The near detector plan presented appears to be well organized and advanced.”) [30] and from the DOE CD-1 review [31]. The closeout report

of the latter concluded that “The near detector uses well validated detection techniques and its design is therefore rather advanced. Its standalone physics program is strong”.

A conservative requirement on the single hit space resolution $< 200 \mu\text{m}$ is assumed for the straws. The STT provides excellent momentum ($\sim 3\%$) and angular ($\sim 2 \text{ mrad}$) resolutions, as well as particle identification exploiting both ionization signals dE/dx and the Transition Radiation produced by e^\pm in the radiator foils. This latter capability offers π rejections $\sim 10^3$ for 90% electron efficiency.

The STT offers several unique advantages with respect to other tracking technologies:

- Polypropylene target radiators ($C_3H_6)_n$ with high chemical purity allowing a clean selection of (anti)neutrino interactions on hydrogen (free proton);
- Suite of different nuclear targets (e.g. C, Ca, Ar, etc.) to measure nuclear effects and the corresponding response (smearing) function;
- Timing resolution allowing to resolve the beam structure & withstanding high rates;
- Transition Radiation (TR) capability for the e^\pm identification (π rejection $\sim 10^{-3}$);
- 4π detection of π^0 from γ conversions within the STT volume;
- Flexible design allowing a variation of the target configuration with density $0.005 \leq \rho \leq 0.2 \text{ g/cm}^3$.

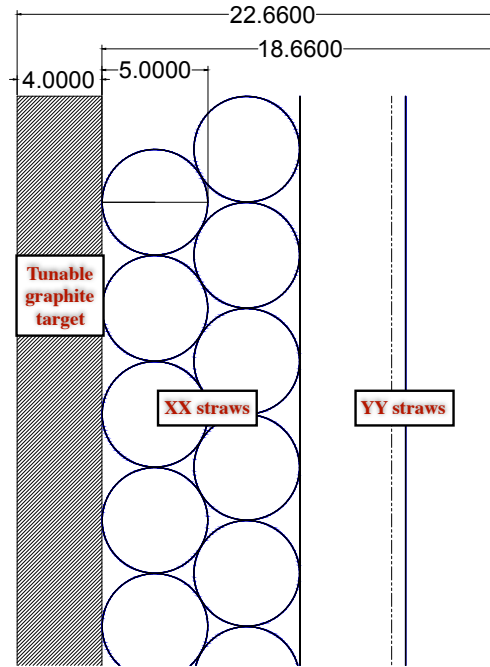


Figure 14: Drawing of one compact STT module equipped with graphite (pure C) target. The thickness of the C graphite plate is tuned to provide the same fraction of X_0 as the CH_2 modules shown in Fig. 12.

3.3.2 Internal LAr target

As described in the previous section, the combined presence of different nuclear target is an asset to understand nuclear effects, in particular effects in the Far Detector target material, Argon.

A small part of the KLOE inner volume can be filled with liquid Argon so that interactions on Argon, Hydrogen and Carbon can be detected and reconstructed with essentially the same detector.

The thickness of the LAr portion must be small enough to reduce energy loss, showering and multiple scattering. The exact positioning, size and shape of this LAr “meniscus” will be object of optimization.

For the present paper, it is assumed the LAr will be placed in (almost) direct contact with the EM calorimeter, at the entrance of the tracking volume. A double Carbon wall Cryostat with vacuum insulation is foreseen. The LAr meniscus will be instrumented with scintillation light readout for event selection and timing. Since purification is not an issue, the cryogenic system can be reduced to the essential and hosted by apertures in the endcaps.

3.4 Electronic Readout for STT

3.4.1 STT Readout Requirements

The Straw Tube Tracker (STT) detector proposal is designed for precise studies of neutrino interactions. It requires excellent vertex, angular and timing resolution to meet its physics goal, resulting in the following requirements for the straw-tube readout electronics:

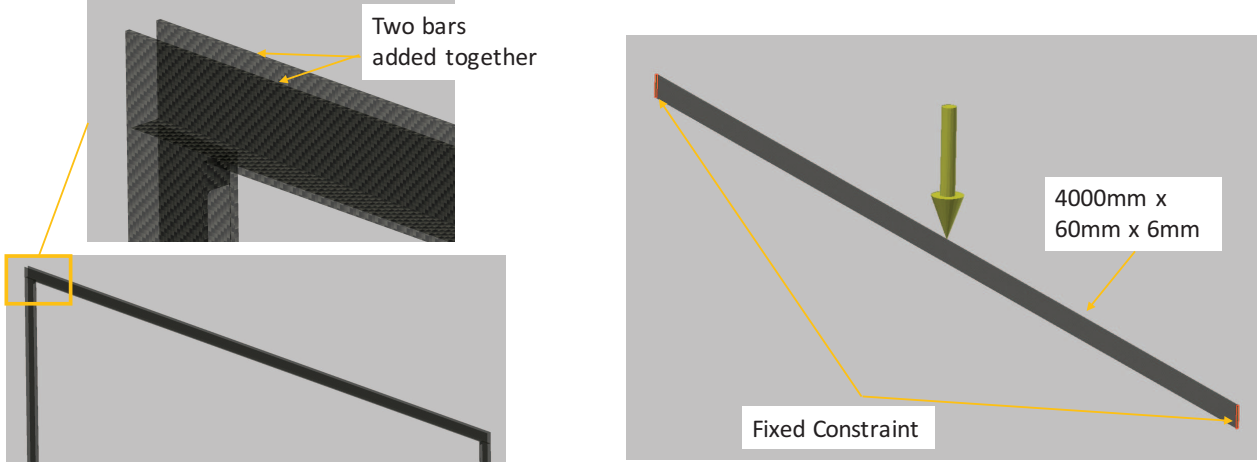


Figure 15: Drawing of the STT module frames using C-composite U-shaped elements.

- Must measure deposited charge and time
- Timing resolution much better than 1ns
- Low threshold to identify charge from a single ion pair
- Dynamic range better than 1000 for charge
- Maximum width of the readout board of 43mm
- Maximum length of the readout board: 16cm for every 64 channels
- Low power to reduce heat

To address these requirements we propose a frontend electronics readout based on the VMM3a custom Application Specific Integrated Circuit (ASIC), derived from the well established VMM1[35]. This ASIC can instrument individual straw tubes to provide precise detector hit charge and time measurements. Each ASIC chip can readout 64 individual channels, making it appropriate for compact electronic boards where high-channel density is useful. The low-power consumption and per-channel cost (~ 90 cent/ch) are similarly useful for a compact detector readout. A development plan that includes construction of a prototype for a low-energy beam test has been defined to demonstrate these ASICs can meet the STT detector design requirements.

3.4.2 VMM3a ASIC Architecture

The VMM3a is a low-power, high performance 64 channel ASIC well suited to compact detector readout electronics[49]. It was developed at Brookhaven National Laboratory and is a component of the ATLAS New Small Wheel upgrade, as well as other detectors. Each of the 64 ASIC channels is highly configurable and combines a preamplifier shaping circuit with an ADC to allow independent digitization of triggered input signals. These digitized signals can be output with four different data readout options, which provides flexibility to accommodate different detector requirements and data rates.

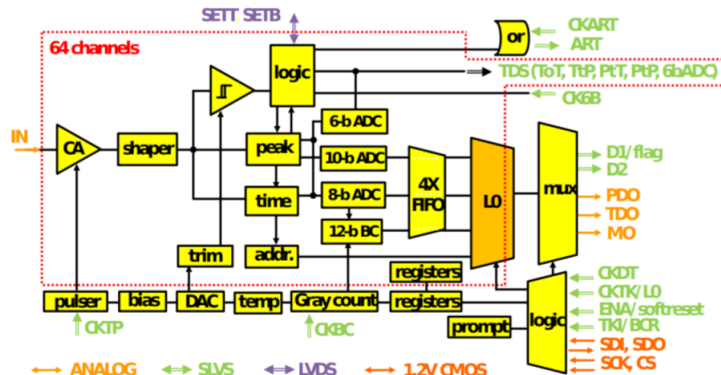


Figure 16: The VMM3a ASIC architecture [49] summarized in a schematic diagram. Each input channel possesses an individual preamplifier and dedicated digitizing logic. The various digital data readout modes are also indicated.

A schematic overview of each VMM3a ASIC channel is shown in Figure 16 [49]. Each channel can be configured to accommodate a variety of input signal sizes, polarity and capacitance. The preamplifier shaping circuit can be configured to use one of four different peaking times (25, 50, 100, and 200 ns) and eight gain settings (0.5, 1, 3, 4.5, 6, 9, 12, 16 mV/fC). A channel-specific discriminator triggers on input signals above a configurable threshold to initiate digitization of the amplified pulse with a 10-bit Analogue to Digital Converter (ADC). Discriminator thresholds are adjusted by a global 10-bit Digital to Analogue Converter (DAC) with additional channel-specific 5-bit trimming DACs. Combined these features allow the VMM3a to satisfy the STT requirement of individual channel deposited charge and time measurements.

3.4.3 VMM3a ASIC Performance

The electronic noise performance of the earlier VMM1 ASIC version has been measured in lab measurements for a range of preamplifier gain and shaping time settings as shown in Figure 17 [35]. As can be seen equivalent noise charge of better than 1000e⁻ can generally be achieved with input capacitance less than 100pF. A similar study with the VMM3a shows similar performance for a variety of shaping time settings as shown in Figure 18[50]. Based on this the VMM3a can likely meet the STT low charge threshold requirement if the straw tube gain is greater than 10⁴ with input capacitance less than 100pF.

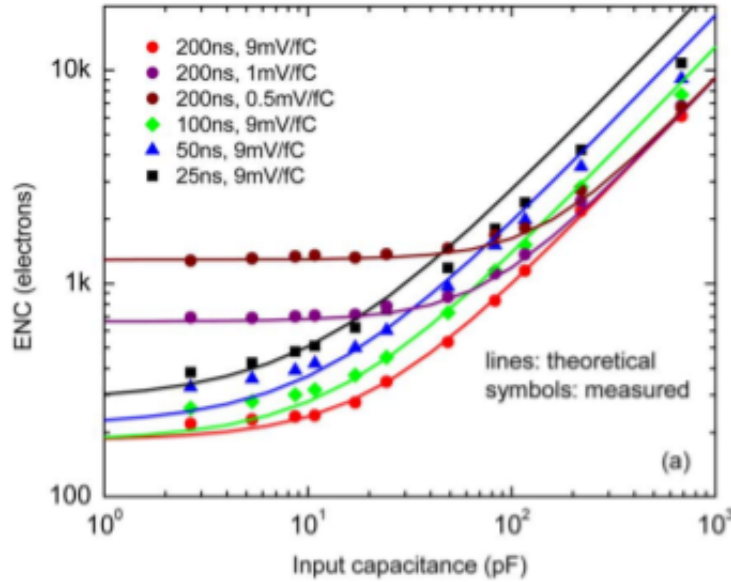


Figure 17: VMM1 equivalent noise charge for a variety of ASIC gain and shaping time settings [35]

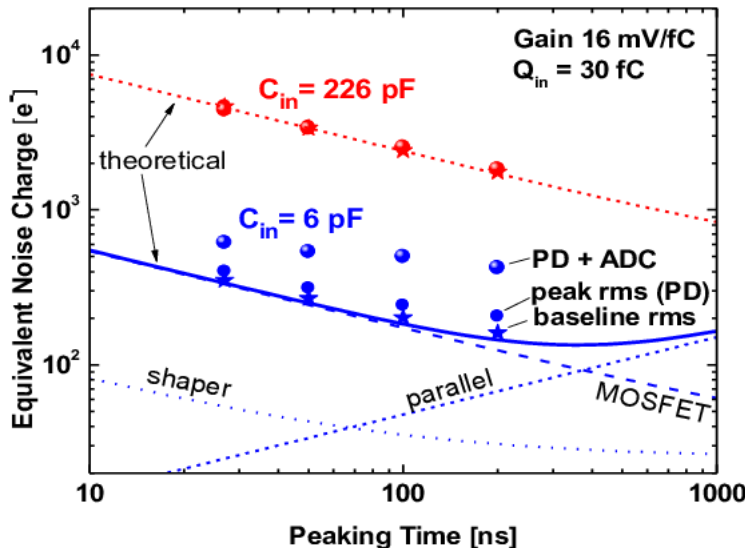


Figure 18: VMM3a equivalent noise charge vs ASIC shaping time settings compared with theoretical expectations also shown. [50]

The time resolution of the VMM3a was also measured in the lab and the results summarized as a function

of input charge in Figure 19. Time resolution better than 1 ns is obtained for 6 pF input capacitance and greater than 1 fC input charge, with much better time resolution achievable with higher input signal amplitude. This suggests the VMM3a can satisfy the STT time resolution requirements with sufficiently high gain and appropriate input capacitance.

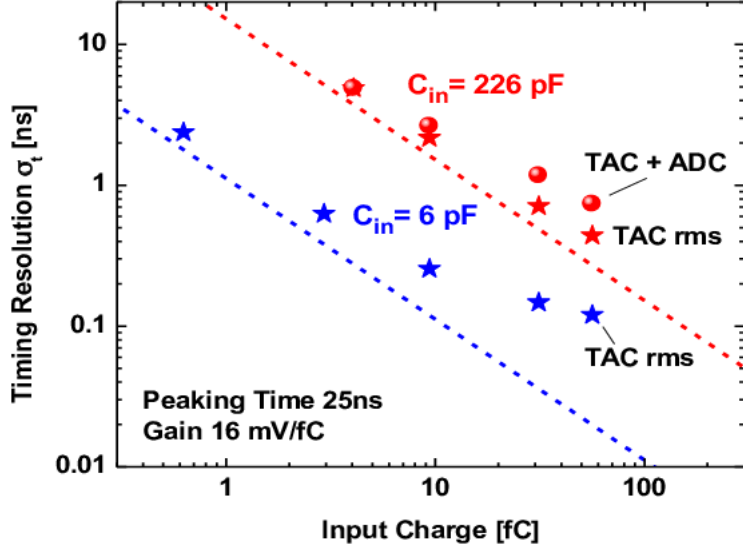


Figure 19: VMM3a time resolution as a function of input charge. Better than ns time resolution is obtained for suitably large deposited charge signals. [50]

More study is required to demonstrate that the VMM3a meets the STT readout requirements for low threshold for charge measurements and a dynamic range greater than 1000 for charge. However the range of ASIC gain options, low electronics noise and availability of a 12-bit ADC suggests the dynamic range requirement can be met. Similarly the configurable channel trigger DAC feature (10 bits global DAC and 5-bit channel specific trim DACs) likely allows the required low charge threshold.

3.4.4 VMM3a ASIC Readout and STT Spatial Constraints

The width of a VMM3a readout board is ultimately limited by the ASIC itself or the digital logic used to co-ordinate its operation. An example of a very compact VMM ASIC readout board is the MMFE-8 developed for ATLAS, a schematic diagram of which is shown in Figure 20. The MMFE-8 can carry up to 8 VMM ASICs, resulting 512 channels in a board with dimensions 215mm x 60mm x 2.54mm. A Functional Programmable Gate Array (FPGA) co-ordinates ASIC operation and digital data readout, and provides a flexible interface to backend readout electronics. A similarly compact board could plausibly be developed for the STT, with the width reduced to meet the 49mm requirement by moving the FPGA in line with the VMM3a ASICs. The MMFE-8 has a linear channel density of 0.42 mm/ch, which is equivalent to 2.6cm for 64 channels. The STT requirement of a maximum readout board length of 16cm for 64 channels is easily achieved with a VMM3a based readout.

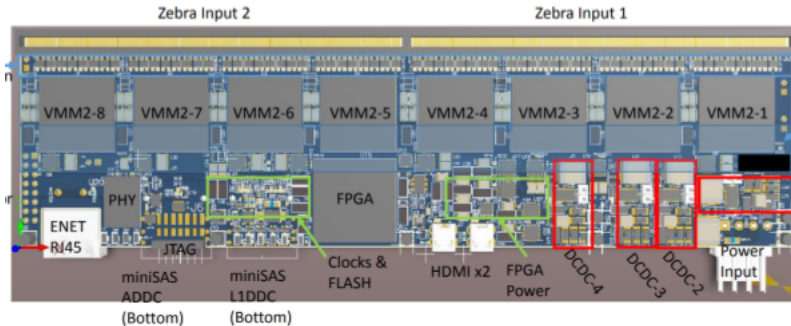


Figure 20: MMFE-8 readout board implements 8 VMM ASICs, equivalent to 512 channels, in a board with dimensions 215mm x 60mm x 2.54mm.

3.4.5 Experience with VMM3a ASIC Readout in Cathode Strip Chambers

The previously mentioned MMFE-8 readout board was adapted to readout Cathode Strip Chambers (CSC) used as a cosmic ray tracker, with a prototype board shown in Figure 21. A single VMM3a ASIC instruments 64 cathode strips, corresponding to a single chamber layer. An FPGA controls and co-ordinates the ASIC readout, and an ethernet based readout is used to transfer digital data resulting from cosmic track hits over a local network to the backend computer. This readout board design successfully tracked cosmic rays passing through a CSC, and is a potential starting point for an STT readout board design.



Figure 21: VMM3a based readout board designed to instrument cathode strip chambers.

3.4.6 VMM3a ASIC Readout DAQ Options

The VMM3a ASIC has four data readout options, including an analogue mode, a continuous mode, a selectable readout window mode (called Level-0 mode) and an Address in Real Time (ART) mode. For the STT the continuous read/write mode and Level-0 modes are most relevant, as they provide the required digitized charge and time measurements output through a pair of dedicated digital data lines. This digital readout provides flexibility towards the implementation of backend Data Acquisition (DAQ) system. A few examples of existing DAQs for VMM-based frontend electronics are briefly described here.

The New Small Wheel (NSW) upgrade for the ATLAS experiment uses the VMM ASIC to instrument Micromegas and small-strip Thin Gap Chambers. The frontend readout chain is summarized in Figure 22. In the NSW the VMM ASICs are installed on MMFE-8 boards and operate using the Level-0 readout mode. A dedicated Read Out Controller (ROC) ASIC directly reads out several VMM ASICs through their digital data lines. The ROC then transfers data via gigabit links to the backend data receivers. This readout system allows very high readout rates and tolerates the high-radiation environment of the ATLAS detector.

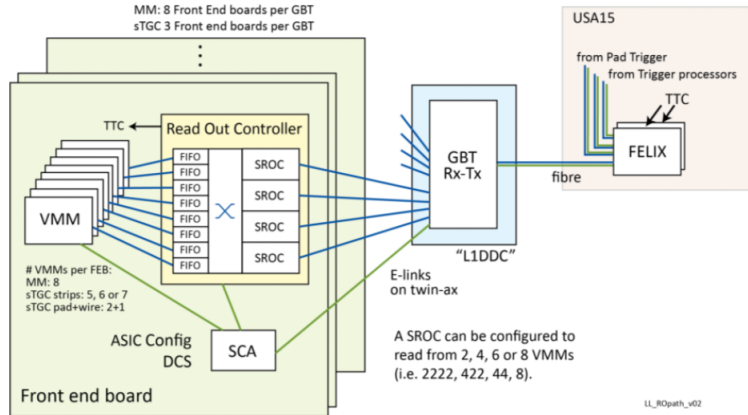


Figure 22: VMM3a based readout board designed to instrument cathode strip chambers.

The CSC VMM3 boards use an on-board FPGA to control and read out a VMM3a ASIC. A dedicated FPGA provides flexibility in terms of implementing the readout backend, and in this case the FPGA uses an ethernet interface to transfer data using the UDP protocol over a local ethernet network to the backend PC. The VMM3 ASICs operate in continuous read/write mode and transfer digitized data when requested by an external trigger signal distributed to each frontend readout board. This readout scheme is easily extended and relatively simple to implement, although is only appropriate for relatively low trigger and data rates.

The Front-End LInk eXchange (FELIX) system was developed for the ATLAS phase-I upgrade and is a detector agnostic backend readout [13]. It provides an interface between frontend electronics and backend networks, as shown for the ATLAS Trigger and DAQ system in Figure 23. One key advantage of the system is that it reduces the need for custom electronics in favour of existing commodity products. It is also a mature readout, having been used in a variety of experiments including ATLAS, protoDUNE, sPHENIX and is a

baseline DAQ option for the upcoming DUNE far detector. A FELIX readout could be implemented for VMM3a readout electronics in the STT, where the simplest option would have the frontend readout board FPGAs transfer VMM3a data over gigabit links to the FELIX PCIe cards. This would result in a simple and scalable readout option that would draw on a large existing development effort.

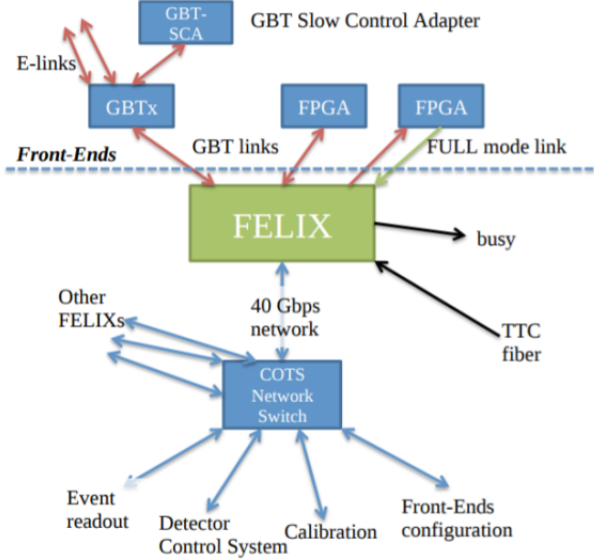


Figure 23: Diagram summarizing the role of the FELIX system in the ATLAS Trigger and DAQ system as an interface between frontend electronics and backend commercial network hardware [13].

3.4.7 VMM3a ASIC Readout Cost and Development Plan

Based on the experience developing VMM3a readout boards for CSCs, a preliminary research and development plan to design a VMM3a board for the STT was defined and summarized in the table below. This plan includes the construction of a prototype VMM3a readout electronic board instrumenting a straw tube to be tested in a low-energy beam in order to demonstrate the required performance. This beam test could make use of the Very-Very-Low-Energy (VVLE) beamline at CERN intended to support upcoming neutrino detector development.

A rough per-channel cost estimate for the proposed readout boards and associated FELIX-based backend is also presented, assuming different numbers of VMM3a ASICs per readout board. For the FELIX-based backend costs it is assumed that each frontend board is connected directly to a FELIX optical link, with each FELIX PCIe card accommodating up to 48 links. Note that these cost estimates do not include labor and certain infrastructure costs, such as low voltage power supplies.

Proposed 3-year Development Plan

Year	Tasks
1	<ul style="list-style-type: none"> • Evaluate VMM3-based readout with straw tube tracker detector • Construct dedicated electronics test stand with straw tubes • Identify potential revisions to ASIC to improve performance • Initial design of prototype electronics based on CSC boards
2	<ul style="list-style-type: none"> • Evaluate prototype electronics performance • Identify any further ASIC or board revisions • Preliminary design of detector and readout integration in STT • Technical design of detector electronics
3	<ul style="list-style-type: none"> • Demonstrate performance of VMM3 electronics and STT in low energy test beam • Full technical design of STT detector and readout

	CP optimized		ν_τ optimized	
	FHC	RHC	FHC	RHC
$K_0 \rightarrow \pi^+ \pi^-$	264,000	132,000	1,981,000	665,000
$\Lambda \rightarrow p \pi^-$	293,000	104,000	1,998,000	503,000

Table 1: Expected numbers of K_0 and Λ decays in charged and neutral current interactions for the various beam configurations and exposures considered in Sec 4.1.

Cost Estimates for STT VMM3a Readout Boards and Felix Backend

Item	Cost
Fabrication and Assembly	$\sim \$150$ per board
Component cost	$\sim \$200$ per board
VMM3a ASIC	$\sim \$25$ per ASIC, 40 cents/ch
4 ASIC board cost per channel	$\sim \$1.75/\text{ch}$
8 ASIC board cost per channel	$\sim \$1.07/\text{ch}$
Felix-backend cost per channel with 4 ASICs per board	$\sim \$0.77/\text{ch}$
Felix-backend cost per channel with 8 ASICs per board	$\sim \$0.40/\text{ch}$

3.5 External range catcher

The momentum of muons created in muon neutrino charged current interactions inside ArgonCube can be evaluated from the particles' range. The range of muons exiting the ArgonCube can be measured through additional range catcher. The catcher, hereafter called ArgonCube range catcher (ACRC), is composed by a sequence of 11 tracking devices interleaved by 10 10-cm iron slabs surrounding ArgonCube.

Muons with enough energy can pass through all iron slabs and reach KLOE magnet. Part of them will stop inside KLOE iron yoke and part will reach the electromagnetic calorimeter while very few will stop inside the coil or the cryostat walls. In order to have a rough estimation of the range of muons stopping inside the yoke, two further tracking devices are used. A tracker, hereafter called external range catcher (ERC), surrounds the upstream surface of the KLOE yoke magnet, while the internal range catcher (IRC) is inserted in the gap between external cryostat wall and the yoke.

3.6 Calibration and Monitoring

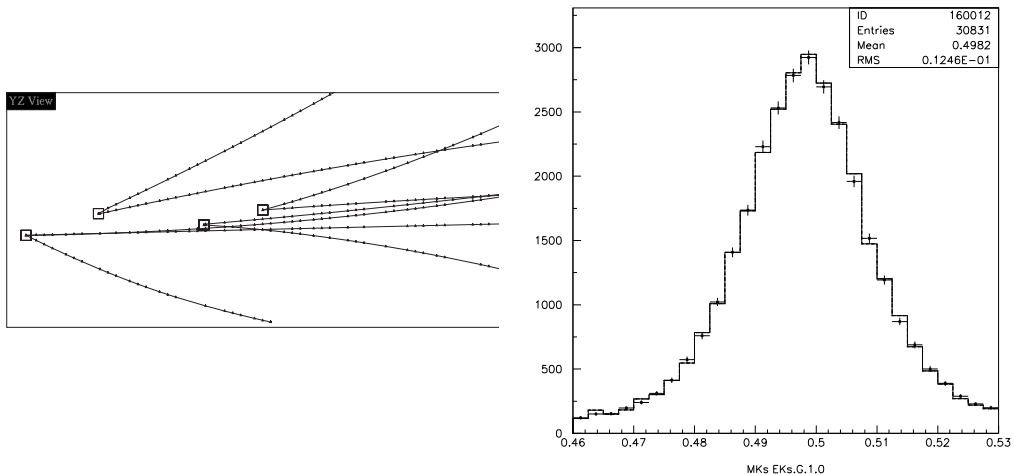


Figure 24: Left panel: example of multi-V0 event in NOMAD data. Right panel: example of reconstructed K_0 mass in NOMAD from identified V0 vertices.

The determination of the energy for charged tracks in the STT is based upon the momentum measurement in magnetic field (spectrometer). The uniformity of the magnetic field in the KLOE solenoid (Fig. 9) implies less stringent requirements on the accuracy of the corresponding B field mapping. For the absolute calibration of the track momenta we can follow the procedure used by the NOMAD experiment – based upon a similar detector concept – exploiting the mass peak of the K_0 decays reconstructed within the tracking volume (V_0 vertices), as illustrated in Fig. 24. Overall, NOMAD achieved a momentum scale uncertainty of 0.2% [80] using the K_0 calibration. We note that this uncertainty is a key parameter determining the sensitivity of the

various measurements to constrain the systematics affecting the long-baseline analyses (Sec. 2.1), as well as of all the precision measurements of fundamental interactions described in Sec. 2.2.

We expect a total statistics of about 264,000 $K_0 \rightarrow \pi^+ \pi^-$ decays within the STT volume with the standard beam configuration and 5 years of FHC data taking (Tab. 1), which is more than 5 times larger than the sample available in NOMAD. On top of that STT offers about 25 times higher segmentation (Sec. 3.3.1) compared to NOMAD. We can therefore anticipate that in STT we should be able to calibrate the momentum scale using K_0 s with an accuracy better than 0.2%. This precision can be achieved only thanks to the unique combination of low-density and relatively large fiducial mass offered by STT.

The tracking and identification of protons can be calibrated using identified V_0 vertices from the decay of Λ , as done in NOMAD. Overall, we expect a total of about 293,000 $\Lambda \rightarrow p\pi^-$ decays within the STT tracking volume with the standard beam configuration and 5 years of FHC data taking (Tab. 1). Identified Λ decays provide a good constrain on systematic uncertainties related to the hadronic energy and vertex reconstruction, since the hadron final state particles are the same as in the $\nu_\mu p \rightarrow \mu^- p\pi^+$ process on hydrogen used for the flux determination (Sec 6.1.1). Furthermore, both Λ and K_0 decays can be used to constrain the systematic uncertainty on the muon angle reconstruction, which is relevant for the analysis of the Q^2 distribution and other kinematic variables.

The electron (positron) reconstruction and identification efficiency in STT can be calibrated in-situ with the large sample of photon conversions into e^+e^- pairs.

The KLOE ECal has been extensively calibrated, with cosmic muons and with photons, as described in section 3.2 and in the literature [7, 6]. Response to neutrons has been studied on a small scale prototype in a low energy neutron beam [16]. Further checks will be performed in situ, with cosmic muons, stopping particles, neutral pions, etc. Measurements prior to the transport can also be envisaged.

4 Simulation setup and tools

Two independent simulation chains have been setup, one based on GENIE and GEANT4, the other completely based on FLUKA. The output of both simulations are ROOT trees. In both, the coordinate system is centered at the centre of the KLOE detector, the x axis is oriented along the solenoid axis and the y axis is vertical. The neutrino beams are assumed to be parallel and uniform over the detector size, oriented along the z axis, which means perpendicularly to the solenoid axis. The vertical inclination of the neutrino beam is taken into account.

4.1 Neutrino fluxes

The DUNE neutrino beam line has undergone a long optimization process, involving proton beam energy, target geometry and material, number of magnetic horns and their design. The recommended design is the 3-horns engineered one, presented at the Oct 2017 beam instrumentation review. It assumes three magnetic horns, a 2.2 m long cylindrical target, and a proton beam operated at 120 GeV. The default beam spectrum has been optimized for the CP violation search and has a 120 MW power and 1.1×10^{21} pot/year. Simulations presented in this work are based on the neutrino fluxes calculated for this baseline design, as available in tabulated form in <http://home.fnal.gov/~ljf26/DUNEFluxes/>. Their are calculated for a near detector located 574 m downstream of the start of Horn 1. Neutrino CC spectra, as obtained from these fluxes convoluted with GENIE cross sections in Argon (see Sec.4.2.1) are shown in Fig.27.

Another interesting option is provided by the LBNF beam optimized to detect the ν_τ appearance in the Far Detector. The corresponding energy spectrum is substantially higher than the one with the default beam configuration (Fig. 25), resulting in an increase of the expected event rates by a factor 2.4 with respect to the default beam (Tab. 2). A realistic scenario could be that after completing a data taking of 5 years with the standard FHC beam and 5 years with the standard RHC beam, we can have dedicated runs with the ν_τ optimized beam. Even a modest exposure of 2 years with FHC and 2 years with RHC in this configuration would substantially enhance the discovery potential of the precision tests of fundamental interactions described in Sec. 2.2. To this end, by the time we can realistically have dedicated runs with the ν_τ optimized beam (after 10 years of data taking with the standard beam) the LBNF beam intensity is expected to be upgraded from 1.2 MW to 2.4 MW.

4.2 Generators

4.2.1 GENIE

The GENIE code [15] is a neutrino event generator for the experimental neutrino physics community. It has a focus on low-energies (≤ 1 TeV) and it is currently used by a large number of experiments working in the neutrino oscillation field. The final project goal is the development of a “canonical” neutrino interaction physics Monte Carlo whose validity extends to all nuclear targets and neutrino flavours from MeV to PeV scales.

A GENIE based application to generate neutrino-induced events in the ND has been developed. The first step at the run time is defining the detector geometry from a standard *gdml* file. The user has the possibility to simulate the neutrino interactions in the whole geometry described in the input file or select

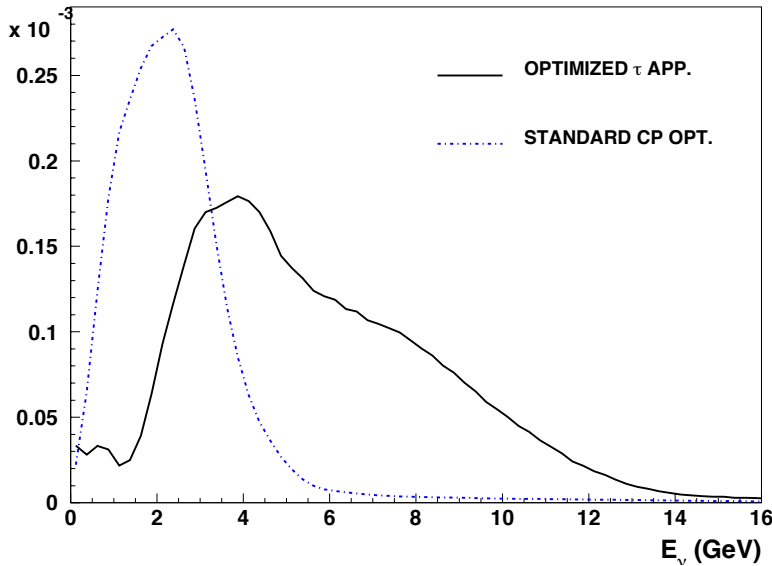


Figure 25: Comparison of LBNF ν_μ fluxes: (a) default 3 horn beam optimized for CP violation (dash-dotted); (b) ν_τ appearance optimized beam (solid).

Table 2: Number of CC interactions simulated inside the detector inner tracker for both FHC and RHC modes. Results with two different LBNF beam options are shown: (a) default 3 horn beam optimized for the CP violation search (1.2 MW, 120 GeV, 1.1×10^{21} pot/year); (b) high energy option optimized for the ν_τ appearance (2.4 MW). The number of events refer to the expected rates in the fiducial mass of the various target material: 4.7 tons of CH₂, 677 kg of H from CH₂, 528 kg of graphite (C), 1 ton of LAr. See text for details.

FHC	CP optimized beam (1.2MW, 5y)				ν_τ optimized beam (2.4MW, 2y)			
	ν_μ	$\bar{\nu}_\mu$	ν_e	$\bar{\nu}_e$	ν_μ	$\bar{\nu}_\mu$	ν_e	$\bar{\nu}_e$
CH ₂	32,525,834	1,560,825	480,295	79,755	62,178,400	1,070,280	628,733	65,144
H	3,056,440	278,935	45,989	13,892	5,921,850	190,183	60,887	11,366
C	3,867,528	168,234	56,998	8,644	7,383,050	115,503	74,524	7,058
Ar	7,785,828	303,766	115,959	16,258	14,337,700	205,101	146,976	13,035
RHC	CP optimized beam (1.2MW, 5y)				ν_τ optimized beam (2.4MW, 2y)			
	ν_μ	$\bar{\nu}_\mu$	ν_e	$\bar{\nu}_e$	ν_μ	$\bar{\nu}_\mu$	ν_e	$\bar{\nu}_e$
CH ₂	5,089,933	12,176,405	227,511	173,194	3,525,940	22,307,900	170,163	175,973
H	485,539	2,265,326	21,780	31,085	335,936	3,939,300	16,221	30,633
C	604,275	1,300,718	27,000	18,650	424,351	2,404,360	20,203	18,955
Ar	1,202,156	2,341,222	54,831	34,668	824,080	4,269,480	18,934	35,011

a part of the detector as active volume. The detector is aligned such that the beam axis pass through its centre. By default, the beam points down by 0.101 radians, being this inclination the one needed to get to the FD.

The code is able to simulate single or multi-flavour neutrino beams crossing the detector, according to standard DUNE flux [38]. The neutrino energy and type are randomly generated according to the input spectrum file and all neutrinos are simulated with a direction parallel to the beam axis.

The neutrino vertexes are generated on a circular surface perpendicular to the beam axis. The radius of generation surface would be equal to the the beam radius ($r \approx 40$ m). This radius is reduced to the minimum required by the simulated flux to cross the whole simulated interaction volume. This choice avoids the simulation of neutrinos not crossing the interaction volume, reducing in this way the number of trials. Once the neutrino is generated, the code simulates its interaction using GENIE, version 2.12.10 [43] is used in this work.

As an example we consider the neutrino events simulated inside the detector inner tracker, having a total mass of 5.13 ton. The neutrino interaction vertexes inside the whole interaction volume are shown in Fig.26, together with the neutrino vertexes generated on the generation surface. The energy spectra of charged current (CC) interacting neutrinos in the internal LAr target, having a mass of 1.01 ton, are shown in Fig.27, considering both forward-horn current (FHC) and reverse-horn current (RHC) mode fluxes. The total number CC interacting neutrinos in the inner tracker are reported in Tab.2, while the number of events in the internal LAr target for various neutrino interactions are summarised in Tab.3.

The code is also able to generate neutrino events according to beam fluxes determined through a 2D

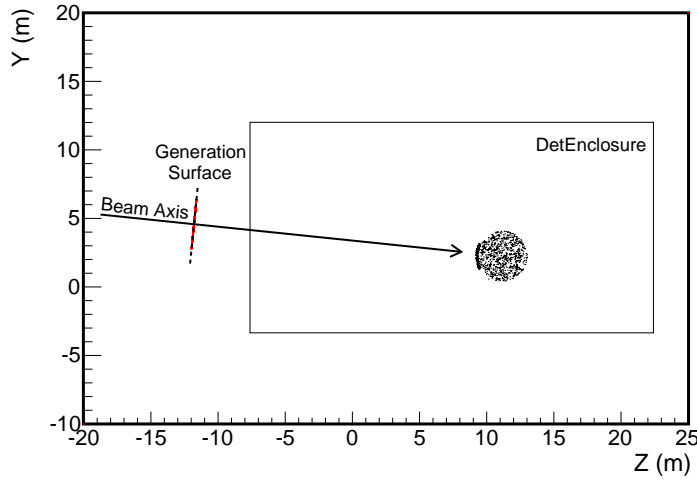


Figure 26: Interaction vertexes (black points) of simulated neutrinos crossing the inner tracker. The red points are the vertexes of the interacting neutrinos drawn on the generation surface perpendicular to the beam axis and represented by the dashed line.

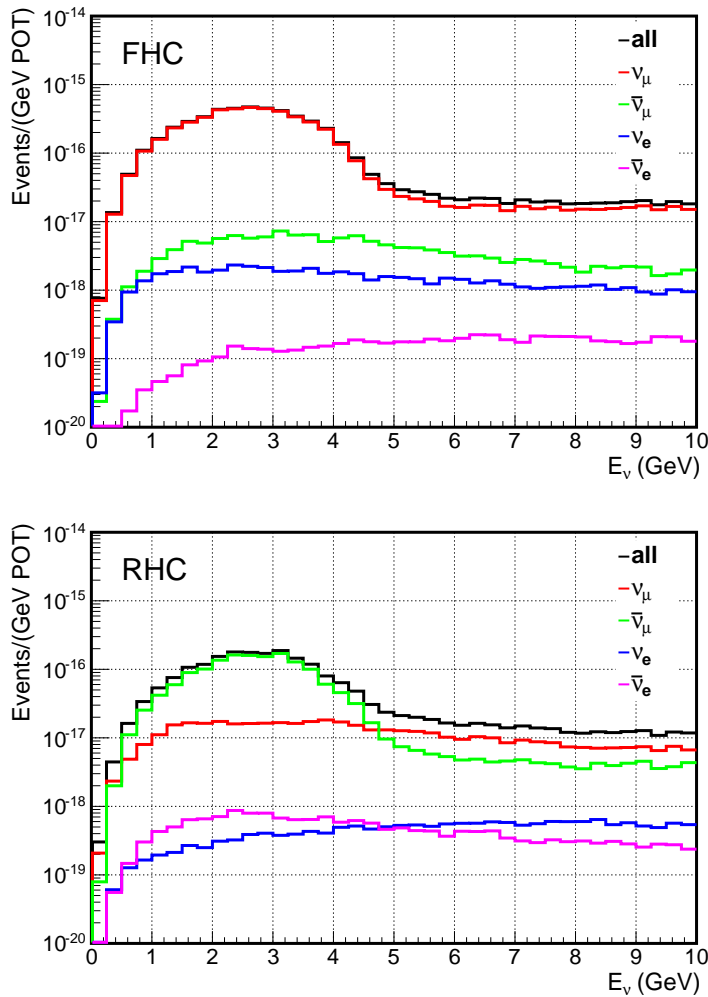


Figure 27: Energy spectra of CC interacting neutrinos in the internal LAr target, having a mass of 1.01 ton, and considering a 120 GeV proton beam in both FHC and RHC modes.

Table 3: Neutrino interaction events simulated inside the internal LAr target (1.01 ton mass), considering both FHC (second column) and RHC (third column) modes. The number of events is given per $1 \cdot 10^{20}$ POTs. Processes are defined at the initial neutrino interaction vertex and thus do not include final-state effects.

Production Mode	ν_μ Events	$\bar{\nu}_\mu$ Events
CC quasi-elastic ($\nu_\mu n \rightarrow \mu^- p$ or $\bar{\nu}_\mu p \rightarrow \mu^+ n$)	33313	12018
NC quasi-elastic ($\nu_\mu N \rightarrow \nu_\mu N$ or $\bar{\nu}_\mu N \rightarrow \bar{\nu}_\mu N$)	10256	5399
CC resonant ($\nu_\mu p \rightarrow \mu^- p\pi^+$)	20565	0
CC resonant ($\nu_\mu n \rightarrow \mu^- n\pi^+(p\pi^0)$)	22513	0
CC resonant ($\bar{\nu}_\mu p \rightarrow \mu^+ p\pi^-(n\pi^0)$)	0	7140
CC resonant ($\bar{\nu}_\mu n \rightarrow \mu^+ n\pi^-$)	0	22513
NC resonant ($\nu_\mu p \rightarrow \nu_\mu p\pi^0(n\pi^+)$)	7363	0
NC resonant ($\nu_\mu n \rightarrow \nu_\mu n\pi^+(p\pi^0)$)	9148	0
NC resonant ($\bar{\nu}_\mu p \rightarrow \bar{\nu}_\mu p\pi^-(n\pi^0)$)	0	3786
NC resonant ($\bar{\nu}_\mu n \rightarrow \bar{\nu}_\mu n\pi^-$)	0	4151
CC DIS ($\nu_\mu N \rightarrow \mu^- X$ or $\bar{\nu}_\mu N \rightarrow \mu^+ X$)	61175	13141
NC DIS ($\nu_\mu N \rightarrow \nu_\mu X$ or $\bar{\nu}_\mu N \rightarrow \bar{\nu}_\mu X$)	19573	5643
CC coherent π^+ ($\nu_\mu A \rightarrow \mu^- A\pi^+$)	655	0
CC coherent π^- ($\bar{\nu}_\mu A \rightarrow \mu^+ A\pi^-$)	0	601
NC coherent π^0 ($\nu_\mu A \rightarrow \nu_\mu A\pi^0$ or $\bar{\nu}_\mu A \rightarrow \bar{\nu}_\mu A\pi^0$)	518	508
NC elastic electron ($\nu_\mu e^- \rightarrow \nu_\mu e^-$ or $\bar{\nu}_\mu e^- \rightarrow \bar{\nu}_\mu e^-$)	12	8
Inverse Muon Decay ($\nu_\mu e^- \rightarrow \mu^- \nu_e$)	4	0
Total CC	138226	43454
Total NC	46872	19513
Total CC+NC	185098	62967

energy-position matrix and choosing an off-axis alignment for the detector. Fig.28 shows the energy spectra of CC interacting neutrinos simulated at different detector position offsets with respect the on-axis alignment. The total number of expected events for various neutrino interactions in FHC mode is reported in Tab.4. Seven different positions, including the on-axis alignment, were simulated. Assuming an equal exposure for both FHC and RHC running, a number of $1.05 \cdot 10^{20}$ POTs per year for each position is considered. The possibility to spend half of the POT on-axis was also explored.

4.2.2 NUNDIS in FLUKA

FLUKA [42, 22] is a multi-particle transport and interaction code. Its neutrino interaction generator, called NUNDIS [23], is embedded in the same nuclear reaction module of FLUKA used for all hadron-induced reactions. NUNDIS describes interactions on single nucleons, while initial state and final state effects are treated by the FLUKA hadronic interaction model, called PEANUT. Quasi elastic reactions are modeled according to [56]. For Deep Inelastic Scattering (DIS), NUNDIS uses available parton distribution functions (PDFs) in order to obtain probability distributions for the kinematical variables Q and Bjorken-x. GRV98[45] is the default PDF-set. Extrapolations are performed for Q2 and Bjorken-x whenever these variables are beyond the ranges defined by the PDF-set. The cross section is obtained according to standard formulation and standard expressions for the structure functions [75]. NUNDIS borrows the same chain hadronization algorithm used in the hadron-hadron interaction model. This FLUKA-native model includes a special treatment of low-mass chains, as described in [25], that is important for a correct description of neutrino interactions at low energies.

Neutrino-nucleon resonance interactions are built on the basis of the Rein-Sehgal formulation [68], however keeping only the contribution from Δ production. No non-resonant background term is considered, assuming that the non-resonant contribution comes from DIS. The transition from RES to DIS is performed by imposing a linear decrease of both cross sections as a function of W.

Initial state effects are accounted for by considering bound nucleons distributed according to a Fermi momentum distribution. Final-state effects include a generalized intranuclear cascade (G-INC), followed by a pre-equilibrium stage and an evaporation stage. Nucleons, mesons and nuclear fragments can be emitted during these stages. Residual excitation is dissipated through photon emission. Experimental data on nuclear levels and photon transitions are taken into account whenever available.

Neutrino interaction events are simulated in the same geometry and in the same run as used for detector simulation. Neutrino cross sections on the relevant material are calculated off-line and convoluted with the same neutrino fluxes as used for the GENIE simulation.

Reaction rates calculated by FLUKA are reported in table 5. Comparison with the GENIE rates in table 3 shows a reasonable overall agreement, with a few exceptions. The relative importance of resonant and DIS channels is different in the two codes, as expected from the different “labelling” of processes, FLUKA having only Δ as resonant channel. It is worthwhile to say that the total single-pion production cross section on nucleons is very well reproduced by FLUKA through the combined contributions of Δ and DIS. The

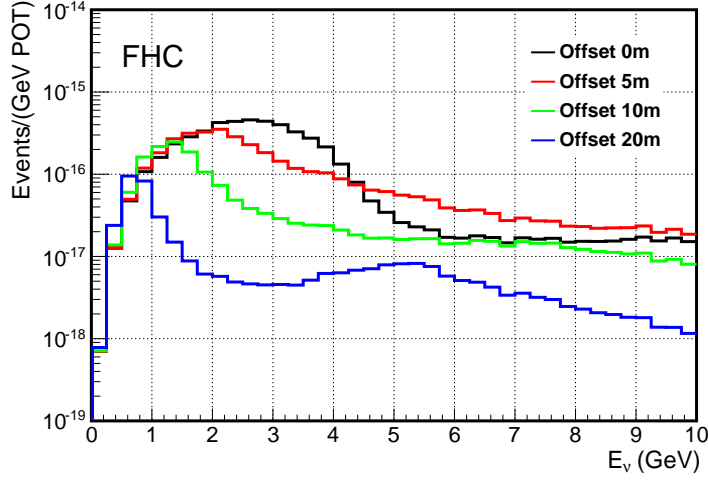


Figure 28: Energy spectra of CC interacting muon neutrinos simulated inside the internal LAr target (1.01 ton mass), considering a 120 GeV proton beam in FHC mode and different detector off-axis alignments.

Table 4: Neutrino interaction events ($E_\nu < 10$ GeV) simulated inside the internal LAr target (1.01 ton mass), considering a FHC mode beam and different off-axis alignments for the detector. The number of events is given considering two different run plans: equal POTs dedicated at each position, including the on-axis alignment and half POTs on-axis.

Equal POTs at each position						
Offset	10^{20} POT	CCInc ν_μ	NCInc	CCInc $\bar{\nu}_\mu$	CCInc ν_e	El. ν_μ -e
0 m	0.786	$9.4 \cdot 10^4$	$3.4 \cdot 10^4$	$2.9 \cdot 10^3$	$1.1 \cdot 10^3$	8.5
5 m	0.786	$7.3 \cdot 10^4$	$2.6 \cdot 10^4$	$2.5 \cdot 10^3$	$9.3 \cdot 10^2$	6.3
10 m	0.786	$3.2 \cdot 10^4$	$1.2 \cdot 10^4$	$1.5 \cdot 10^3$	$6.1 \cdot 10^2$	2.7
15 m	0.786	$1.4 \cdot 10^4$	$5.5 \cdot 10^3$	$8.0 \cdot 10^2$	$3.9 \cdot 10^2$	1.3
20 m	0.786	$7.9 \cdot 10^3$	$3.2 \cdot 10^3$	$5.2 \cdot 10^2$	$2.5 \cdot 10^2$	0.7
25 m	0.786	$4.8 \cdot 10^3$	$2.0 \cdot 10^3$	$3.4 \cdot 10^2$	$1.7 \cdot 10^2$	0.4
30 m	0.786	$3.1 \cdot 10^3$	$1.3 \cdot 10^3$	$2.5 \cdot 10^2$	$1.2 \cdot 10^2$	0.3
All	5.500	$2.3 \cdot 10^5$	$8.4 \cdot 10^4$	$8.8 \cdot 10^3$	$3.6 \cdot 10^3$	20.2

Half POTs on-axis						
Offset	10^{20} POT	CCInc ν_μ	NCInc	CCInc $\bar{\nu}_\mu$	CCInc ν_e	El. ν_μ -e
0 m	2.750	$3.3 \cdot 10^5$	$1.2 \cdot 10^5$	$1.0 \cdot 10^4$	$4.0 \cdot 10^3$	29.6
5 m	0.458	$4.2 \cdot 10^4$	$1.5 \cdot 10^4$	$1.5 \cdot 10^3$	$5.4 \cdot 10^2$	3.7
10 m	0.458	$1.9 \cdot 10^4$	$6.8 \cdot 10^3$	$9.0 \cdot 10^2$	$3.6 \cdot 10^2$	1.6
15 m	0.458	$8.5 \cdot 10^3$	$3.2 \cdot 10^3$	$4.7 \cdot 10^2$	$2.3 \cdot 10^2$	0.7
20 m	0.458	$4.6 \cdot 10^3$	$1.9 \cdot 10^3$	$3.0 \cdot 10^2$	$1.5 \cdot 10^2$	0.4
25 m	0.458	$2.8 \cdot 10^3$	$1.2 \cdot 10^3$	$2.0 \cdot 10^2$	$9.7 \cdot 10^1$	0.3
30 m	0.458	$1.8 \cdot 10^3$	$7.7 \cdot 10^2$	$1.4 \cdot 10^2$	$6.8 \cdot 10^1$	0.2
All	5.500	$4.1 \cdot 10^5$	$1.5 \cdot 10^5$	$1.3 \cdot 10^4$	$5.4 \cdot 10^3$	36.5

Table 5: As in table 3 for FLUKA generated events.

Production Mode	ν_μ Events	$\bar{\nu}_\mu$ Events
CC quasi-elastic ($\nu_\mu n \rightarrow \mu^- p$ or $\bar{\nu}_\mu p \rightarrow \mu^+ n$)	30700	12700
NC quasi-elastic ($\nu_\mu N \rightarrow \nu_\mu N$ or $\bar{\nu}_\mu N \rightarrow \bar{\nu}_\mu N$)	14300	8890
CC resonant ($\nu_\mu p \rightarrow \mu^- p\pi^+$)	16700	0
CC resonant ($\nu_\mu n \rightarrow \mu^- n\pi^+(p\pi^0)$)	5500	0
CC resonant ($\bar{\nu}_\mu p \rightarrow \mu^+ p\pi^-(n\pi^0)$)	0	1900
CC resonant ($\bar{\nu}_\mu n \rightarrow \mu^+ n\pi^-$)	0	5500
NC resonant ($\nu_\mu p \rightarrow \nu_\mu p\pi^0(n\pi^+)$)	3700	0
NC resonant ($\nu_\mu n \rightarrow \nu_\mu n\pi^+(p\pi^0)$)	3500	0
NC resonant ($\bar{\nu}_\mu p \rightarrow \bar{\nu}_\mu p\pi^-(n\pi^0)$)	0	1600
NC resonant ($\bar{\nu}_\mu n \rightarrow \bar{\nu}_\mu n\pi^-$)	0	1600
CC DIS ($\nu_\mu N \rightarrow \mu^- X$ or $\bar{\nu}_\mu N \rightarrow \mu^+ X$)	78500	17400
NC DIS ($\nu_\mu N \rightarrow \nu_\mu X$ or $\bar{\nu}_\mu N \rightarrow \bar{\nu}_\mu X$)	36500	9600
Total CC	132000	37700
Total NC	58100	21700
Total CC+NC	190100	59400

other noticeable difference is a larger Neutral Current Quasi Elastic rate in FLUKA.

4.3 Detector simulation

4.3.1 FLUKA

The KLOE magnet has been modeled with coaxial cylindrical shells respecting the actual dimensions and material composition. For simplicity, the end caps are rendered as flat disks. An update to the real end cap shape is foreseen. The Electro Magnetic calorimeter (EM Calo) was initially described as an homogeneous mixture of Lead and scintillator. Later, the actual structure of the barrel calorimeter has been implemented, using the lattice capabilities of the FLUKA geometry and reusing part of the model already developed for the description of a KLOE sub-module and its calibration with a neutron beam [16]. Both the geometry and the material composition have been carefully reproduced. For the fibers, an average density between cladding and core has been used : $\rho = 1.044 \text{ g/cm}^3$. The glue is composed by 72% epoxy resin, $\text{C}_2\text{H}_4\text{O}$, $\rho = 1.14 \text{ g/cm}^3$ and by 28% hardener, $\rho = 0.95 \text{ g/cm}^3$, on its turn composed by four different amines. Layers of lead and fibres are stacked to build the rectangular parts of each module, as in fig 29 and triangular parts are added to obtain the trapezoidal shape, to be repeated 23 times. The inner part of KLOE contains a Liquid Argon Layer, directly adjacent to the upstream part of the barrel, having a maximum depth of 10 cm in z and spanning the whole extension in x. The LAr part is supposed to be contained by a 2 cm thick Carbon wall. The rest of the inner volume is filled with STT layers. The radiators are simulated as plastic layers with density equivalent to the foil/air content. Straw tubes and their walls are faithfully reproduced. A cross-section of the full geometry is shown in figure 30. The magnetic field is assumed to be perfectly solenoidal. An update to include a full field map is foreseen. The field intensity is 0.6 T in the inner volume and EM calorimeter, 1.5 T in the joke. All physics processes are simulated with the maximum accuracy allowed by the code. In particular, pointwise correlated cross sections are used for low energy neutron interactions on Argon, Carbon and Hydrogen. Signal quenching is applied to energy depositions in the EM calo fibres, with dE/dx dependence according to a Birks parametrization $dL/dx = kdE/dx/(1. + c_1dE/dx + c_2(dE/dx)^2)$ with $c_1 = 0.013g/(MeVcm^2)$ and $c_2 = 9.610^{-6}g^2/(MeV^2cm^4)$ (typical values from literature). Signal attenuation along the fibres is applied offline using parameters derived experimentally during the KLOE operation.

The output of the FLUKA simulation was processed to take into account light generation inside the Wavelength Shifting Fibers (WSFs), its propagation and collection.

The segmentation of the detector was implemented in the code that processes the output of the simulation, considering the real properties and the actual geometry of the modules of the KLOE calorimeter. In particular, each trapezoidal module of the barrel is divided in five planes, and 12 clovers, so that each module contains 60 cells. Fibers in the same cell are grouped together and deliver light to the same photomultiplier tube, thus, the central coordinates of each cell are used instead of the exact interaction coordinates. This applies for the coordinates orthogonal to the direction of the fibers, while in the direction of the fiber the interaction position was used. A sketch of the calorimeter barrel is visible in figure 32. Interaction points inside the calorimeter are represented in black while the center of each cell is represented in yellow.

For each particle interacting inside the fibers, the simulation gives the following information: interaction position, interaction time and the energy deposited in the fiber. Quenching is already taken into account in the simulation. The number of generated photons is extracted from a Poisson distribution with mean $25E/\text{MeV}$, where E is the energy deposited during the interaction in MeV.

Once produced, photons are divided in two groups to consider their propagation to the opposite ends

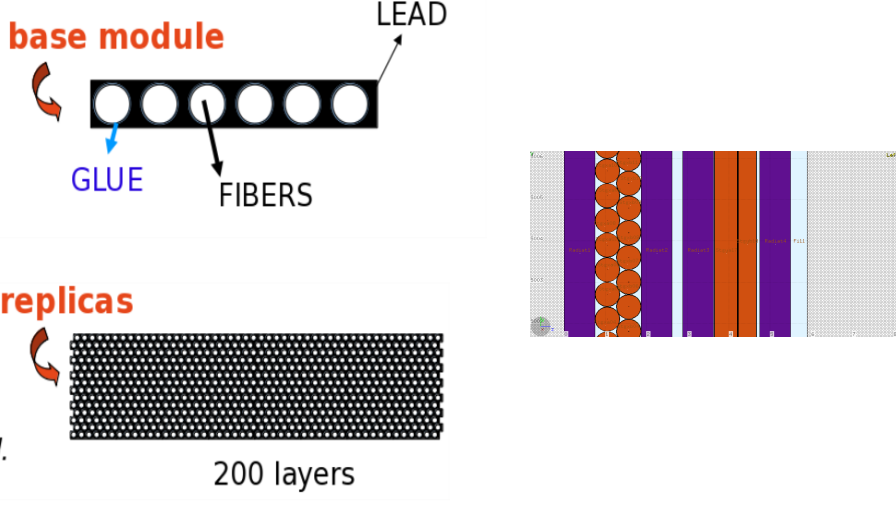


Figure 29: Details of the FLUKA geometry. On the left, the basic layer of the Kloe EM calorimeter, and its repetition to obtain a module. On the right, the STT structure, with straw tubes (orange) and radiators

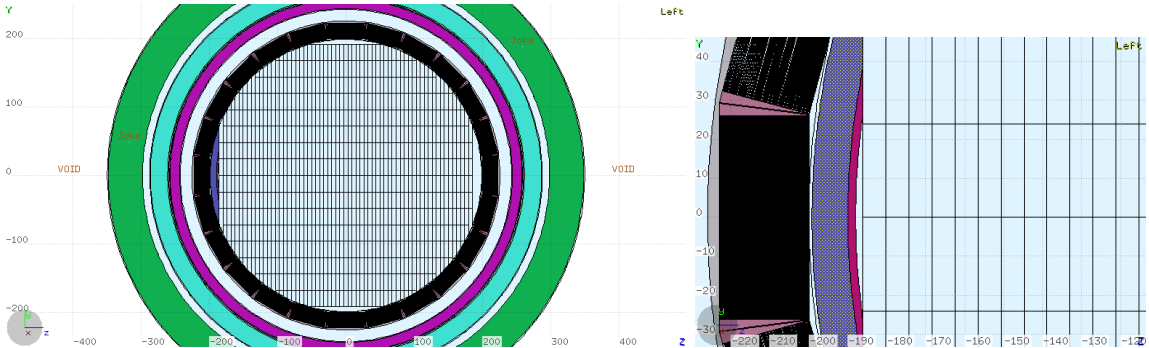


Figure 30: Left: Cross section of the implemented Kloe geometry , including Joke(green), coils, Em Calo (black), LAr insert and stt (not fully rendered in the graphics). Right:zoom on the LAr insert.

of the fiber. The propagation time t_{prop} . is calculated starting from the distances d_1 and d_2 of the PMTs from the interaction point, using a propagation speed $v_f = 1/5.85$ m/ns. A random jitter extracted from a Gaussian distribution with $\sigma = 260$ ps was added to the propagation time to simulate the time resolution of each cell after correcting the time offset (see [7] for details). The signal time t , i.e. the time of the event as seen after the PMT, is then given by

$$t = t_{event} + t_{prop.} + t_{jitter} \quad (2)$$

Being t_1 and t_2 the the time of a signal as seen by the PMTs on the opposite end of the same cell, the time of the event is obtained:

$$t_{event}^{reco} = \frac{1}{2}(t_1 + t_2 - (d_1 + d_2)/v_f) \quad (3)$$

There was no need to implement constant fraction discrimination of the signals, as the scintillation time was artificially set to zero in the simulation. Figure 31 shows the difference $t_{event}^{reco} - t_{event}$ between the reconstructed interaction time and the interaction time given by the simulation, reflecting the gaussian jitter of 260 ps.

Light attenuation was implemented by means of a negative exponential function of the distance between the interaction point and each PMT. The attenuation coefficient depends on the plane in which the light is generated inside the calorimeter module, accordingly to the features of the fibers used in that plane.

4.3.2 GEANT4-based simulation

An alternative detector simulation has been performed following the prescription of the Near Detector Concept Study Group reported in [63]. This choice allows to cross check between the findings of the two simulation chains. The geometry is created using the General Geometry Description (*gegede*) [44] extended by *dunendgdd* [37] to build proposal geometries for DUNE near detector. *gegede* is a pure Python module to generate a description of a constructive solid geometry, represented in GDML files, specifically as used by Geant4 or ROOT applications. In particular the geometry used to obtain the results presented in this

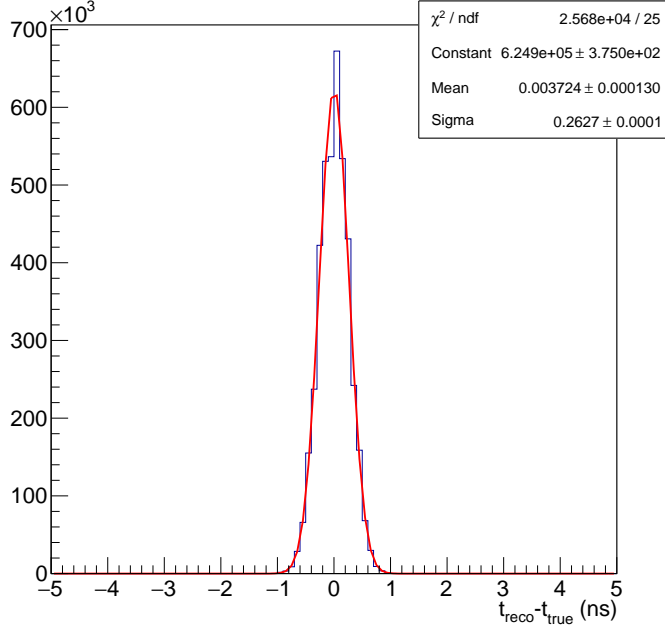
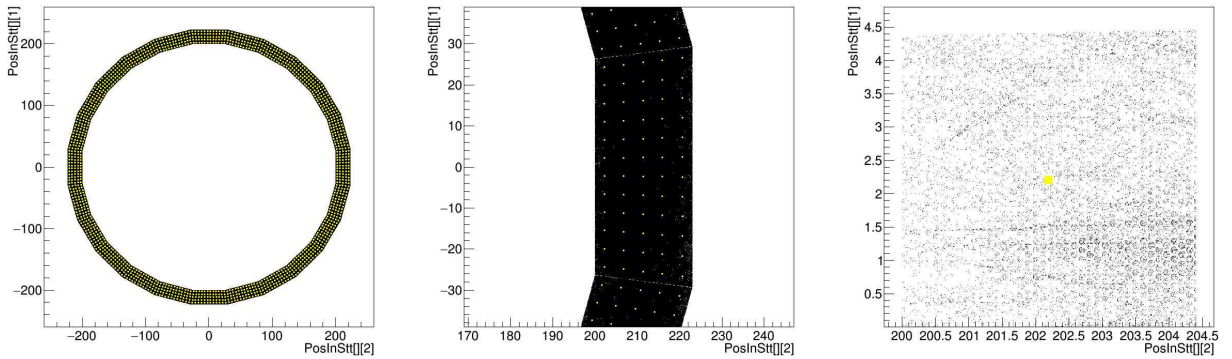


Figure 31: Distribution of the difference between the time reconstructed from the calorimeter w.r.t. time of the particle interaction in the fiber.

document is based on modifications of the ArgonCube detector and the KLOE magnet already implemented in the *dunendggd* package.

The KLOE magnet geometry is modeled by several coaxial cylindrical shells representing the barrel and flat disks representing endcaps. The right-handed coordinates system is chosen so that the positive z axis coincides with the projection of the beam direction onto the horizontal plane, the positive y axis is upward vertical and the x axis is along the symmetry axis of the magnet. The magnet is composed by an external 37-cm-thick iron return yoke and a 1-cm-thick copper coil inserted between the 1.5-cm-thick inner and outer aluminum walls of the cryostat. The barrel of the electromagnetic calorimeter consists of 24 identical trapezoidal modules. Each one is 4.3 m long, 23 cm thick and at a distance of 2 m from the center of the magnet. Two additional 2 m radius and 23 cm thick cylindrical modules form the endcaps. The modules consist of 209 700- μm -thick polystyrene scintillator slabs interleaved with 209 400 μm -thick lead foils.

The internal cylindrical volume of the magnet with a radius of 2 m and a length of 3.8 m contains a tracking system composed of modules of XX and YY straw tube planes interleaved with radiator foils. Each plane consists of two staggered planes of straw tubes. The straw tube has wall of 20- μm -thick kapton layer and is filled with a mixture of Argon (70%) and carbon dioxide (30%). Different straw tube radius, from 0.5 cm to 0.25 cm, has been studied. The radiator foils are modeled as an unique volume composed of a



(a) Side view of the entire calorimeter barrel.
(b) Zoom of a barrel module (side view).
(c) Zoom of a cell in a barrel module (side view).

Figure 32: Sketch of the calorimeter barrel and representation of its segments. Interaction points inside the calorimeter are represented in black and the center of each cell is represented in yellow.

blend of air and polypropylene. The thickness, composition and overall density is evaluated according to the foils thickness and pitch, for which different configurations have been studied. The internal region has an mean density of $\approx 0.1 \text{ g/cm}^3$ and an overall mass up to $\approx 4.9 \text{ ton}$ depending on the straw tube module configuration and on the fill factor. A solution with a 1-ton meniscus filled with liquid argon placed in the upstream part of the inner volume is also investigated. The magnetic field strength in the inner volume is 0.6 T while in the return yoke is 1.75 T in the opposite direction.

The detector simulation is performed using *edep-sim* [41]. It is a wrapper around the GEANT4 particle propagation simulation and is intended as a tool to simulate all of the particle propagation and geometry related issues. Where it's available (and in particular for argon), the simulation implements a fairly detailed model of the energy deposited as ionization and scintillation. This is implemented using the NEST model [74]. *Edep-sim* output is then converted into detector digits in order to be used for the subsequent event reconstruction. Concerning the STT digit, the position in the perpendicular plane and the time of the hits are used. For what concerns the calorimeter, each module is divided in 5 layers in the radial direction, each layer is divided in 12 cells with about $4.5 \times 4.5 \text{ cm}^2$ section. The light produced in each cell are readout on both side by two photomultipliers. The response of both photomultipliers (charge and time) are simulated, taking into account scintillator decay time, photon propagation and light attenuation, starting from the energy deposition in each cell.

5 Neutrino event reconstruction

5.1 Single particles

5.1.1 Muon momentum and angular resolutions

The measurement of the muon momentum has been studied by means of two different simulation codes (Geant 4 and Fluka). Both the models corresponding to very similar results, details are given only for the Fluka one, whereas for Geant 4 just the results are depicted.

Fluka simulation - Assuming the DUNE-neutrino beam, two different data samples have been generated. In the first sample 10^4 neutrino interactions are simulated in the LAr meniscus, in the second sample 10^4 neutrinos interact in the STT volume (mainly in the radiator). In both cases the muon-track reconstruction is based on the STT hits, assuming a spatial resolution of 0.2 mm on y and x axes and 0.01 mm on z axis (beam axis).

In order to estimate the detector performances a simplified reconstruction method has been implemented assuming that the muon track is well identified. The events are selected requiring at least 5 STT hits due to the muon in the bending plane ($y - z$ view). This cut implies the introduction of a target fiducial volume, that is the interaction vertex must be at least 30 cm from the walls of the detector. The sagitta method, the parabola-fit and the circumference-fit have been tested in order to estimate the muon momentum in the bending plane (p_{yz}). The two fit methods are preferred because they exploit the large number of STT hits and the circumference-fit results the best one.

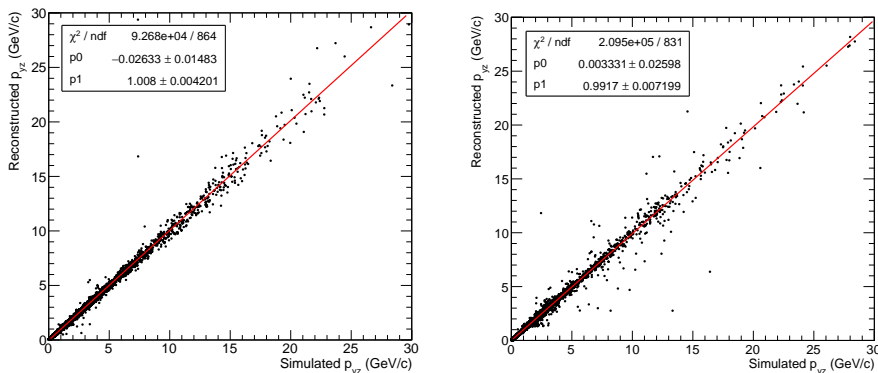


Figure 33: Fluka simulation - Scatter plot of the reconstructed muon momentum on the bending plane vs the simulated one (left: LAr meniscus, right: STT target).

Then two other very loose cuts are applied looking at the fit results. One is referred to the reduced-chisquare value, and the other one requires that the reconstructed Larmor radius is lower than 200 m, which implies a muon energy lower than $\sim 36 \text{ GeV}$. After the estimate of the muon momentum in the bending plane (Fig. 33), the dip angle (λ) is measured by the fit of the track in the $\rho - x$ plane (see F. Ragusa "An Introduction to Charged Particles Tracking", www.mi.infn.it/~ragusa/tracking_sns_28.05.2014.pdf). As a conclusion the reconstructed muon momentum is $p = p_{yz}/\cos\lambda$. Fig.s 34 and 35 show the percentage error on the measurement of p_{yz} , λ and p for neutrino interactions in the LAr and in the STT, respectively.

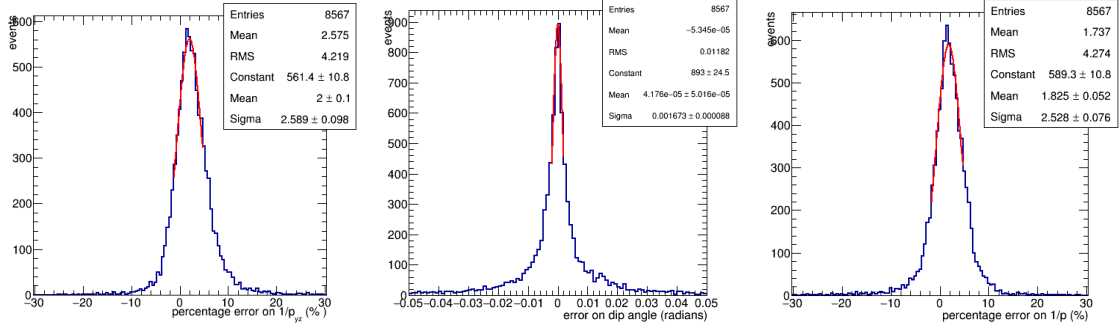


Figure 34: Fluka simulation, LAr meniscus - Percentage errors on the muon momentum measurement: momentum on the bending plane (left), dip angle (center), momentum (right).

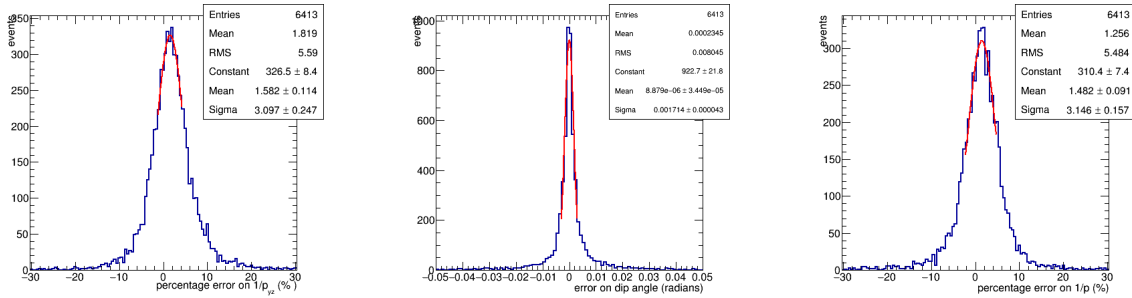


Figure 35: Fluka simulation, STT target - Percentage errors on the muon momentum measurement: momentum on the bending plane (left), dip angle (center), momentum (right).

In Fig. 36 the percentage error on p is shown for different neutrino-energy ranges. The dependence of such error on p value is finally summarized in the plots of Fig. 37 both for LAr and STT target interactions.

In the case of the LAr meniscus the reconstructed momentum is compared to the *true* momentum after the energy loss in LAr layer. In order to estimate the original muon momentum, the path-length and the energy loss inside LAr should be taken into account by means of the vertex reconstruction.

For both the samples (LAr and STT) the tracking algorithm can be improved by considering the energy losses in the STT volume. Up to now we did not update the algorithm because this energy-loss effect is estimated very small.

Geant simulation -

The results obtained with Geant4, following the *dunendggd + edep-sim* prescription described in Sec. 4.3.2, are very close to those obtained with Fluka. The muon track reconstruction, as for the Fluka simulation, is based on STT hits assuming a spatial resolution of 0.2 mm in the bending plane and on the same event selection described for the Fluka simulation. Applying a circular-fit for the estimation of the muon momentum p_{yz} and a linear fit for the dip-angle λ in the $\rho - x$ plane, the total muon momentum is reconstructed. The results in terms of percentage uncertainties, as $\delta(1/p)/(1/p) = 3.4\%$, are reported in Tab. 5. The muon charge misidentification, defined as the ratio between the number of wrong sign charges and the total number of reconstructed charges, is estimated to be 0.8% in the full momentum range.

5.1.2 Electron momentum and angular resolutions

As for the muon performances, the electron momentum and angular resolutions has been studied by means of the two - Fluka and Geant4 - simulations. The two codes give very similar results.

Fluka simulation Taking into account the same fiducial volume cut on the interaction vertex - 30 cm from the walls of the detector - and applying a circular-fit model, a percentage resolution on the electron total momentum of 5.3% is obtained (Fig. 38, center). As stated in the previous Section, the circular-fit model does not take into account for the energy loss, and this approximation is evident in the non-Gaussian tail on the right side of the distribution shown in Fig. 38. This also results in a bias on the mean of 4%. The resolution on the dip-angle λ is 1 mrad with unbiased mean, the angular error distribution is shown in Fig. 38 (right). The electron charge misidentification for reconstructed tracks is 1.2% in the full energy range.

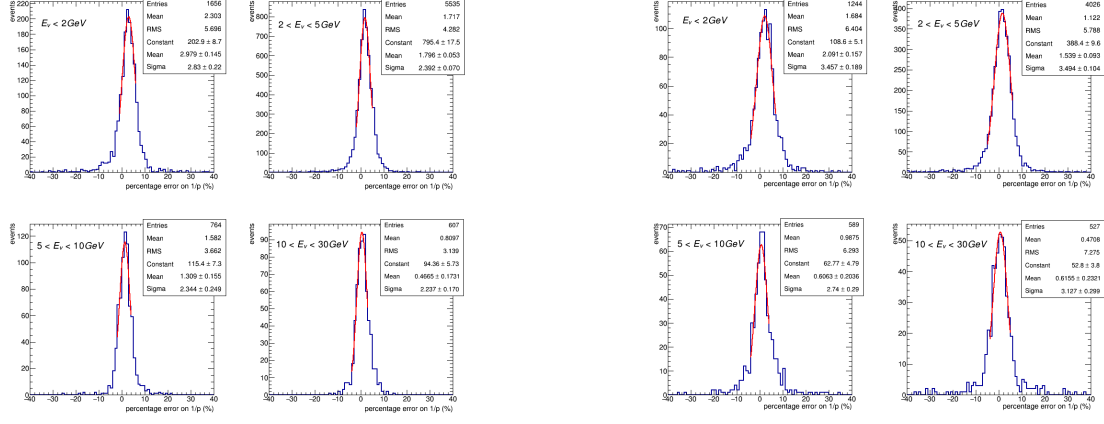


Figure 36: Fluka simulation - Percentage error on the muon momentum in different neutrino-energy ranges. Left: LAr-target. Right: STT-target.

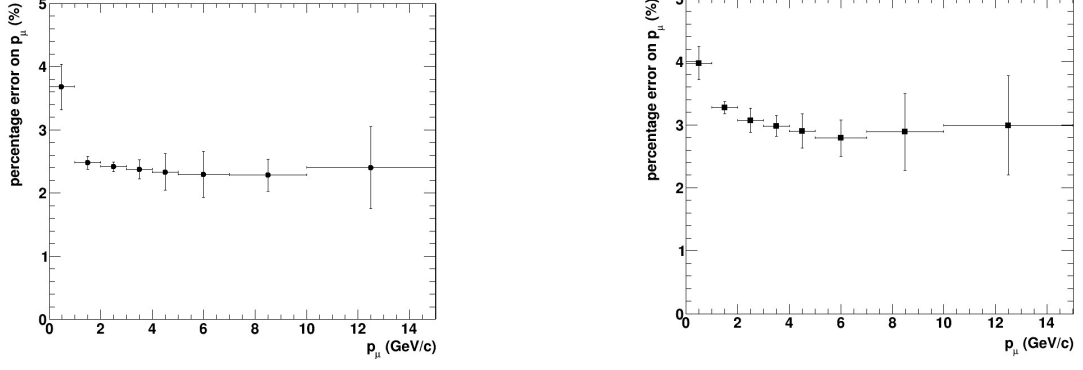


Figure 37: Fluka simulation - Percentage error on the muon momentum as a function of the momentum value. Left: LAr-target. Right: STT-target.

Geant4 simulation The results obtained with Geant4 are compatible with those obtained with Fluka. Following the same simulation chain used for muons (*dunendggd + edep-sim*) and applying a circular-fit model, the electron total momentum resolution is 5% with a bias on the mean of 3.8% and the angular resolution on the dip-angle is 0.8 mrad.

Simulation	Target	p_{yz} (%)	dip-angle (mrad)	p (%)
FLUKA	LAr meniscus	2.6 ± 0.1	1.67 ± 0.09	2.53 ± 0.08
FLUKA	STT	3.1 ± 0.2	1.71 ± 0.04	3.1 ± 0.2
Geant 4	STT	3.50 ± 0.05	1.1 ± 0.1	3.43 ± 0.05

Table 6: Uncertainties in the reconstruction of the muon momentum.

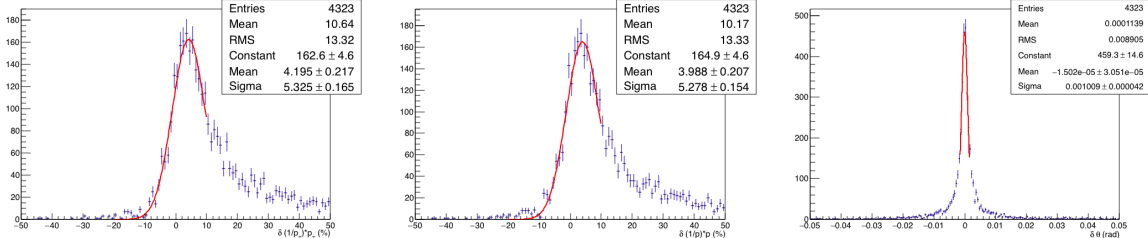


Figure 38: Percentage errors on electron momentum in the bending plane p_{yz} (left), on electron total momentum (center) and angular dip-angle resolution (right).

5.1.3 π^0 identification and reconstruction

The sample used to study π^0 's, is composed by ν_μ CC interactions with the vertex located inside the tracking volume.

To develop the algorithm for the π^0 reconstruction, we produced a dedicated sample composed by 8000 events. The number of π^0 that decay in two photons is tabulated in Tab.7.

Number π^0	number of events
0	5082
1	2135
2	589
3	139
4	44
≥ 5	11
Total	8000

Table 7: Number of π^0 that decay in two photons.

The energy spectrum of this sample is shown in Fig. 39.

In order to develop and test the algorithm, a restricted sample with only one π^0 was selected. The calorimeter hits are associated and merged into a cluster if $\Delta x = 20$ cm and a $\Delta\phi = 5$ deg. x is the distance along the axis of the KLOE magnet and ϕ is the azimuthal angle. These values were optimized using hits from π^0 maximizing the number of events with two reconstructed clusters while keeping the contamination of hits originating from other charged particles at a few per cent level.

Two cuts in energy are also applied: before the clusterization procedure, hits with energy lower than 1 MeV are discarded; after the clusterization, only clusters with total energy (defined as the sum of the hit energy) higher than 20 MeV are retained. The number of reconstructed cluster are tabulated in Tab. 8.

As first stage, only events with two reconstructed clusters were considered. The comparison between the true Monte Carlo energy and the reconstructed one (defined as the sum of the two cluster energy) is shown in Fig. 40.

The invariant mass of the π^0 is computed from the two clusters. Finite energy and position reconstruction effects are introduced at this stage smearing the true MC information of the clusters. The energy resolution is parametrized as $\sigma_E/E \simeq 5.7\%/\sqrt{E(\text{GeV})}$. The position of the cluster is defined as the energy weighted barycenter of the hits ($E_{\text{hits}} > 1$ MeV) belonging to the cluster. The barycenter is smeared according to the space resolution of the KLOE calorimeter (4.5 mm). The invariant mass resolution for the sample of ν_μ CC events with one π^0 and two reconstructed clusters is 15.1%, as shown in Fig.41 left.

The clusterization procedure was also tested considering all calorimeter hits. A deterioration of the performance is expected if the clustering algorithm merges hits that do not originate from the π^0 . To estimate such deterioration we compared the two cluster sets obtained with the full hit sample and with the subsample of π^0 hits, respectively. A π^0 cluster is associated to the closest full hit cluster using the (unsmeared) energy weighted barycenter of the clusters. The mean number of spurious hits, defined as the difference between the hit in each π^0 cluster and the hits in the associated clusters, is 1.3 . The calculation of the invariant mass is also performed using the all hit clusters, giving a resolution of 16.8%, as shown in Fig. 41.

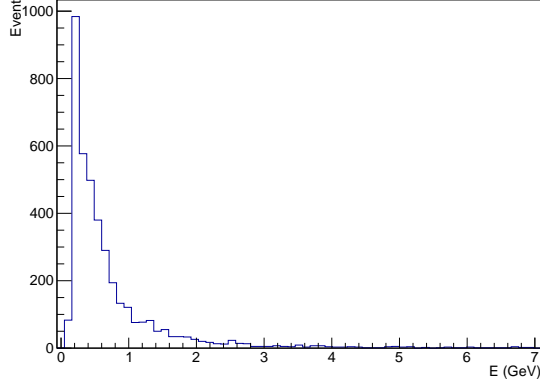


Figure 39: Energy spectrum for π^0 events.

Number of cluster	number of events
0	2
1	215
2	1366
3	376
4	112
≥ 5	64
Total	2135

Table 8: Number of reconstructed cluster with energy higher than 20 MeV, using the criteria $\Delta x = 20$ cm and $\Delta\phi = 5$ deg for one π^0 events.

The momentum of each reconstructed cluster is calculated for the evaluation of the π^0 tri-momentum resolution. After applying the energy and barycenter coordinates smearing, the sum of the momenta is compared with the true MC π^0 momentum, as shown in Fig. 42 left. The resolution is 12.1 %, compatible with the π^0 energy resolution (12.2%).

The resolution in the π^0 flight direction angle is also calculated, as shown in Fig. 42 right, considering the same smearing applied for the momentum. The angle resolution is 2.3%, as expected considering the spatial resolution of the calorimeter.

The same analysis is performed considering events with two π^0 produced by the interaction of the neutrino in the target. The clusterization procedure is the same as before and the number of reconstructed cluster, obtained considering all calorimeter hits, is tabulated in Tab. 9.

Number of cluster	number of events
≤ 2	17
3	87
4	248
5	120
≥ 6	117
Total	589

Table 9: Number of reconstructed cluster with energy higher than 20 MeV, using the criteria $\Delta x = 20$ cm and $\Delta\phi = 5$ deg for two π^0 events.

For the subsample of events with four reconstructed clusters, we computed the invariant mass resolution of each π^0 . In this case, the resolution is limited by the energy and spatial resolution of the calorimeter and by the combinatorial background. There are three possible combinations of the four clusters, each giving an invariant mass pair, m_1 and m_2 . The combination that minimizes $|m_1 - m_{\pi^0}| + |m_2 - m_{\pi^0}|$ is chosen by the reconstruction algorithm. The resolution using energy and baricenter smearing is 19.4%, as shown in Figure 43.

For this cluster combination, the π^0 momentum and angle resolutions, evaluated as previous case, give the result of 16.3% for the momentum and 2.6% for the angle, as show in Fig. 44.

As a check, the cluster combination is found using the tri-momentum p_{reco} of each cluster and choosing the combination that minimize $|p_\gamma - p_{reco}|$, where p_γ is the MC tri-momentum. The cluster combination so obtained corresponds with the combination found with the previous method in the 79.1%. As before, the

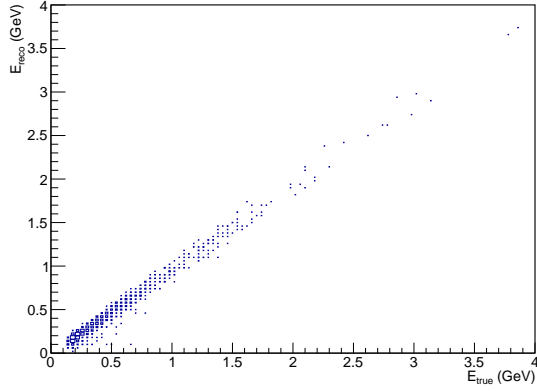


Figure 40: True energy E_{true} vs reconstructed energy E_{reco} in two reconstructed cluster for one π^0 events.

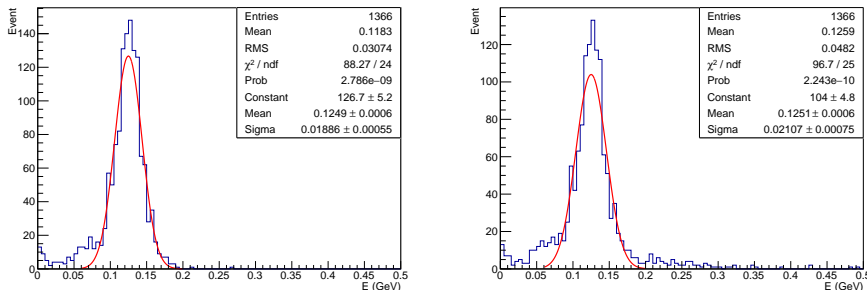


Figure 41: Invariant mass for two cluster event reconstructed by means true MC π^0 hits (left) and all hits deposited in the calorimeter (right). The red curve is the gaussian fit function.

invariant mass is calculated, giving a resolution of 17.6%.

5.1.4 Neutron detection

The signal induced from neutron interaction can be observed in the calorimeter or with lower probability in the Straw Tube Tracker (STT). In the KLOE calorimeter, thanks to the large percentage (about 50%) of lead in a structure of organic fiber scintillators, the neutron detection efficiency is enhanced due to the abundant production of secondary particles in inelastic interactions of the neutrons with high Z material. The signal collected from each cell (see section 3.2 for the details) can be acquired if the total energy released in the scintillating fibers is higher than 100 keV. On the other hand, neutron interactions in the STT detector are not as probable as in the calorimeter, due to the STT low mass. Nevertheless, the signal can be detected when the deposited energy in an interaction is higher than 200-300 eV.

A detection efficiency study was performed using the FLUKA simulation described in section 4.3.1, where the STT tracker and the full geometry of the KLOE calorimeter with fibers and lead was implemented. In particular, the quenching effect for the generated light was taken into account, as well as light attenuation and the time spread due to photon propagation inside the fibers. By analyzing the signal coming from each cell, the neutron efficiency was studied for the two detectors as a function of the kinetic energy of the neutrons emitted in the interaction vertex inside the LAr target.

The kinetic energy distribution of more than 100000 neutrons generated from the neutrino interaction in the LAr layer is shown in red in figure 45. The distribution is peaked at low energy, where a smaller fraction of neutrons is detected from the STT and the calorimeter, but it extends up to few GeV, where the global detection efficiency is very high. In figure 45 the detection efficiency is shown as a function of the neutron kinetic energy at the vertex, for the calorimeter (blue), the STT (green) and their combination (black). The energy threshold considered for STT was 250 eV. As expected, the calorimeter efficiency is much higher than the STT efficiency even if the STT contribution is relevant at lower energy. For a neutron kinetic energy higher than 1 GeV the calorimeter efficiency is close to 1. Taking into account the total number of neutrons generated in neutrino interactions in the LAr target, 17% was detected by the STT, while 55% was detected by the calorimeter. In conclusion, if we take into account the cases in which the neutron is detected from both the detectors, the global neutron detection efficiency of the whole apparatus is about 64%, rising to more than 72% for if the neutron kinetic energy is higher than 100 MeV.

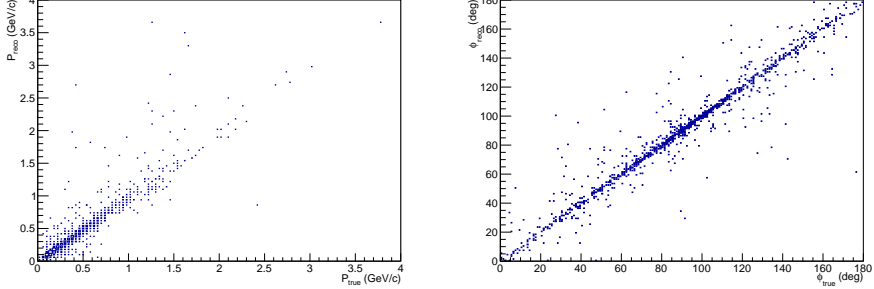


Figure 42: True momentum P_{true} vs reconstructed momentum P_{reco} in two reconstructed cluster for one π^0 events (left). True angle ϕ_{true} vs reconstructed angle ϕ_{reco} in the same subsample (right).

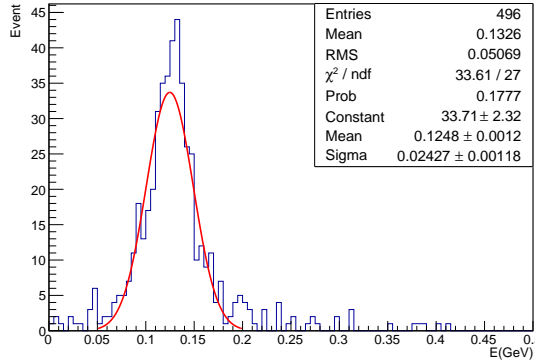


Figure 43: Invariant mass for two π^0 events, reconstructed with four. It is calculated using all hits deposited in the calorimeter. The red curve is the gaussian fit function.

5.1.5 Neutron energy reconstruction by time of flight technique

In this analysis the kinetic energy of neutrons was determined by the time of flight technique. By exploiting the knowledge of position and time of deposited energy in the calorimeter or in the STT detector and by using the vertex information from the Monte Carlo simulations, the neutron kinetic energy was reconstructed for each detected neutron. If the energy deposited from neutrons or neutron daughters was detected both in the STT and in the calorimeter, the hit with the smallest time was selected for reconstructing the velocity of the primary neutron. A time accuracy $\sigma = 0.8$ ns was considered for the STT. In figure 46 the histogram of β_{reco} versus $\beta_{true} = P/E$ (where P is the momentum and E is the neutron total energy) for neutrons detected only in the STT is shown. The kinetic energy is well reconstructed for neutrons with β_{true} between 0.1 and 0.6, while at higher kinetic energy the reconstructed values are more spread around the β_{true} value. In fact, when the distance between the vertex and the interaction point is very short (mainly for neutrons with smaller kinetic energy) or when the time of flight is very small (for neutron with higher kinetic energy) a small deviation in the reconstructed interaction time (due to the detector accuracy or to secondary particles interactions) can have a big effect on β_{reco} . Furthermore, neutrons with $\beta_{true} < 0.2$ scatter several times without generating a detectable signal, making the time of flight technique not able to properly reconstruct their velocity.

When the neutron velocity is reconstructed by exploiting the interactions in the calorimeter, only the cells with a deposited energy bigger than 100 keV are considered. For each cell the reconstructed time and the coordinate of the interaction were calculated as the weighted average on the deposited energy of the times and coordinates of the hits occurring inside the cell.

Thus, to calculate the kinetic energy of the primary neutron, the cell with the smallest reconstructed time was considered and the plot of β_{reco} vs β_{true} for events detected only by the calorimeter is shown in Fig. 47.

In figure 48 the plot of β_{reco} vs β_{true} for all the detected events is shown. If the neutron was detected from both the detectors, the signal with the smallest time was used for the kinetic energy reconstruction. Since the calorimeter detects the biggest fraction of the events, the plot in figure 48 is very similar to the plot in figure 47. Taking into account the neutron spectrum after neutrino interaction, it is clear why all the histograms are more populated for $\beta_{true} < 0.2$ with respect to the area at higher β_{true} . In figure 47, 48 and in the plots of 49, where few sections of the plot in figure 48 are shown for different intervals of β_{true} , the distribution of β_{reco} is always peaked around the β_{true} value. On the other hand, many detected neutrons are reconstructed with a very low energy. This happens when neutrons interact by elastic scattering. In fact, for these events, the signal induced in the detector is mainly due to interactions occurring very far from

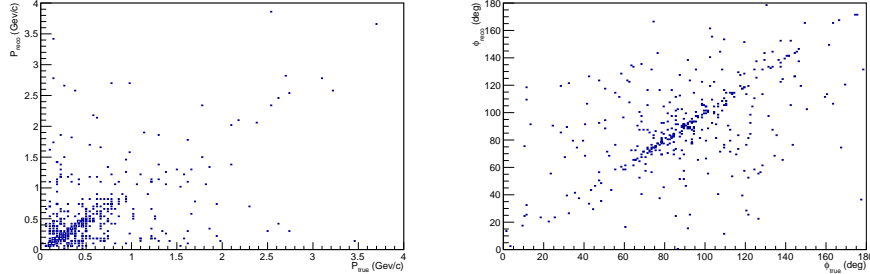


Figure 44: True momentum P_{true} vs reconstructed momentum P_{reco} in four reconstructed cluster for two π^0 events (left). True angle ϕ_{true} vs reconstructed angle ϕ_{reco} in the same subsample (right).

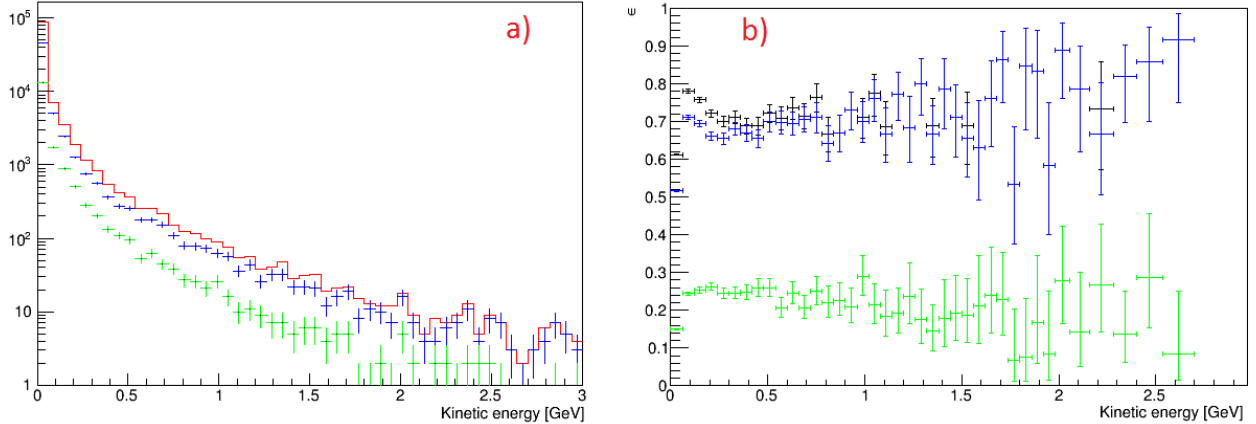


Figure 45: a)The kinetic energy distribution of neutrons generated from the neutrino interaction in the LAr layer (red) and the number of neutrons detected in the STT detector (green) and in the calorimeter (blue) as a function of the neutron kinetic energy at the neutrino interaction vertex. b) The neutron detection efficiency of the calorimeter (blue), of STT (in green), of the whole apparatus calorimeter + STT (in black) as a function of the neutron kinetic energy at the neutrino interaction vertex. The points at higher energy were calculated by grouping the adjacent bins.

the first interaction of the primary neutron.

Since the neutron energy distribution is peaked at low energy, where the cross section of elastic scattering is high, about 51% of detected neutrons are reconstructed with a very low energy. In the other cases, the kinetic energy is better reconstructed and the fraction of neutrons for which $\frac{\beta_{reco}-\beta_{true}}{\beta_{reco}} < 0.3$ is about 60%.

In conclusion, taking into account both the detectors, the neutron kinetic energy can be reconstructed with 30% precision for about 28% of the detected neutrons.

5.2 Particle Identification

The STT combines a high resolution tracking with an efficient particle identification throughout its entire volume. The detector design was optimized for the reconstruction and identification of e^\pm and γ since the most critical measurements in DUNE ND involve e^\pm : ν -e elastic scattering, $\nu_e(\bar{\nu}_e)$ CC, π^0/γ , etc.

A unique feature of STT is the availability of Transition Radiation (TR) for the identification of e^\pm with $\gamma > 1000$. Figure 50 shows that the use of TR in NOMAD provided a rejection factor of 10^3 for π with an e^\pm efficiency of 90% or better [21]. We performed detailed simulations of the TR in the STT modules by using the code developed by P. Nevski at BNL for the ATLAS TRT detector. Tabl 10 summarizes the average number of TR photons detected in the straws for 10 consecutive STT modules equipped with radiators and a 5 mm CH₂ target plate (Fig. 12). The presence of the 5 mm CH₂ target slab practically decouples individual STT modules since it absorbs most of the undetected TR photons exiting from the modules. The dependence of the number of TR photons detected in a STT module (average over 10 consecutive modules) from the electron energy is shown in Fig. 51. To this end, it is instructive to compare the STT performance with the corresponding one in NOMAD, since this latter has been extensively demonstrated with neutrino data. Figure 52 shows that an electron crossing 17 STT modules (corresponding roughly to a track length of 74 cm) results in about the same number of detected TR photons as in the complete NOMAD TR detector (9 modules) for $E > 1.5$ GeV. However, at lower energies the STT performance is substantially better than the NOMAD one [21], with an increase in the number of TR photons detected by more than 60% at E=0.5 GeV. We note that the total length of STT is 4 m and therefore, on average, we expect a substantially better e^\pm identification than in NOMAD (Fig. 50) at all energies.

Reconstructed vs true β (STT)

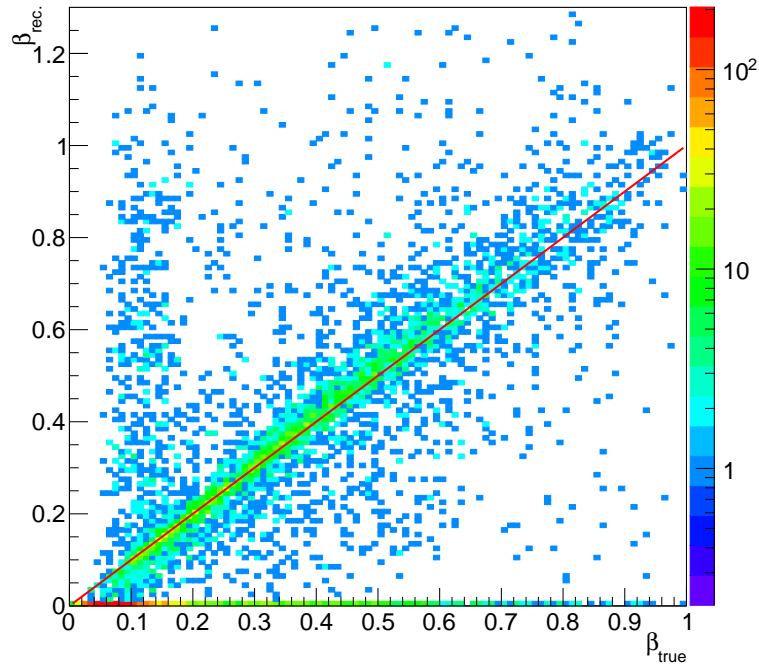


Figure 46: β_{reco} vs β_{true} as a function of β_{true} in the STT.

Reconstructed vs true β (calorimeter)

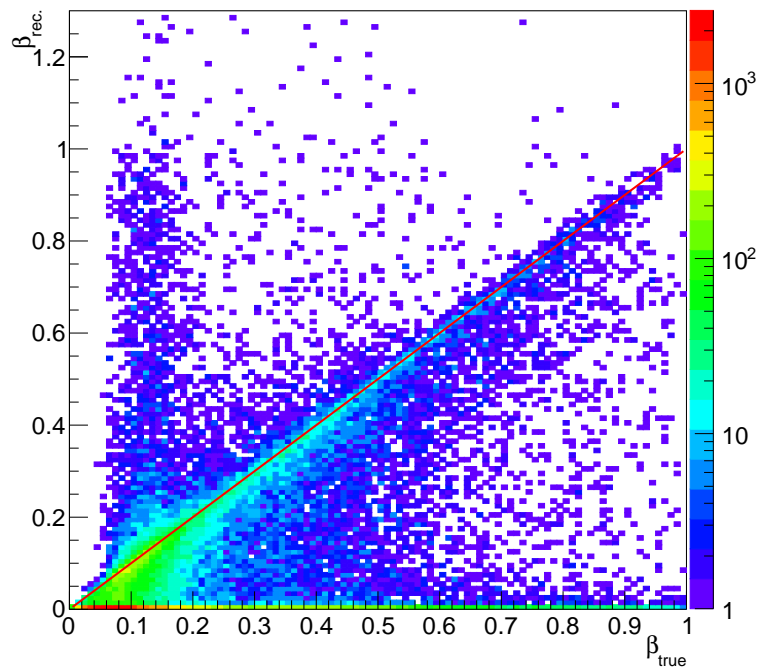


Figure 47: β_{reco} vs β_{true} as a function of β_{true} in the calorimeter.

Reconstructed vs true β

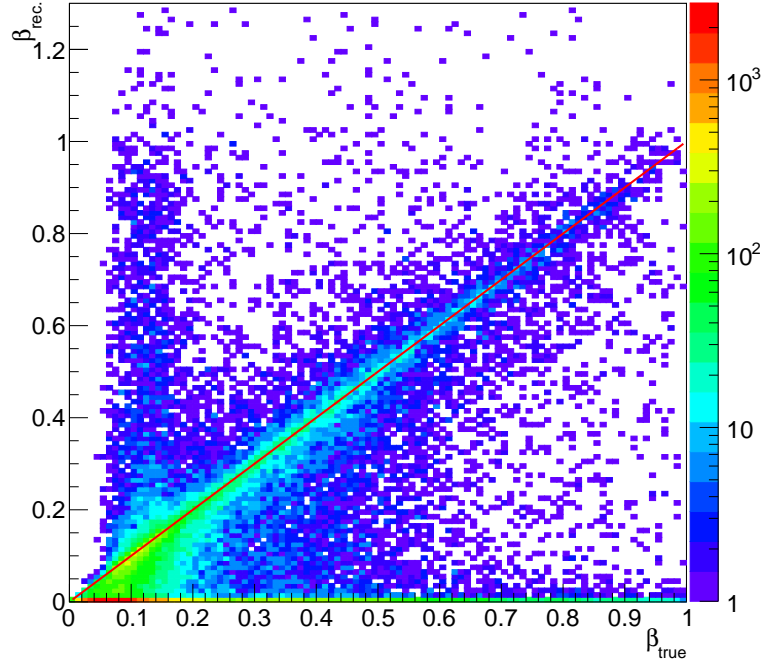


Figure 48: β_{reco} vs β_{true} as a function of β_{true} for the combination of STT and calorimeter.

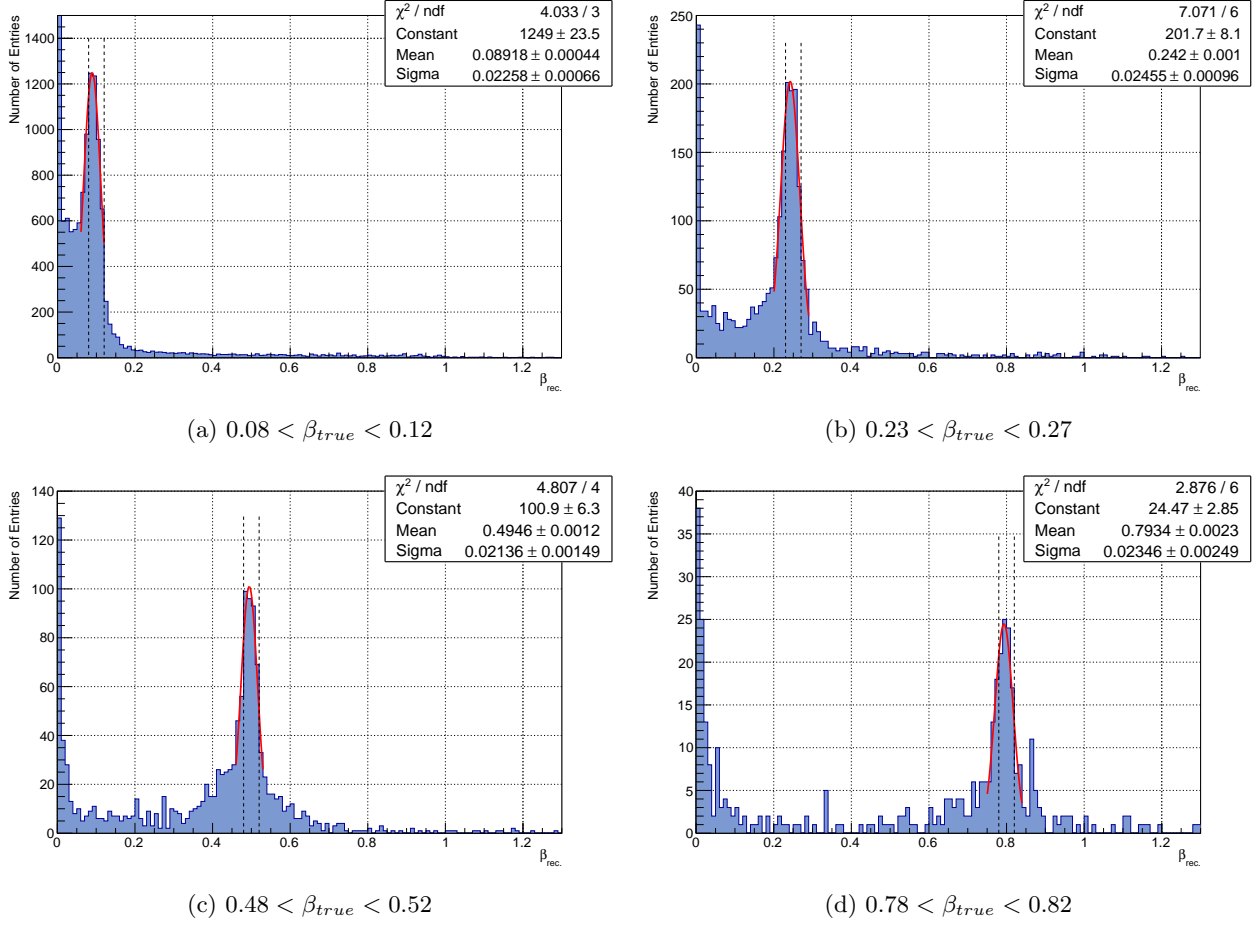


Figure 49: Sections of figure 48 at different β_{true} . Two vertical dashed lines in each figure indicate the corresponding β_{true} interval.

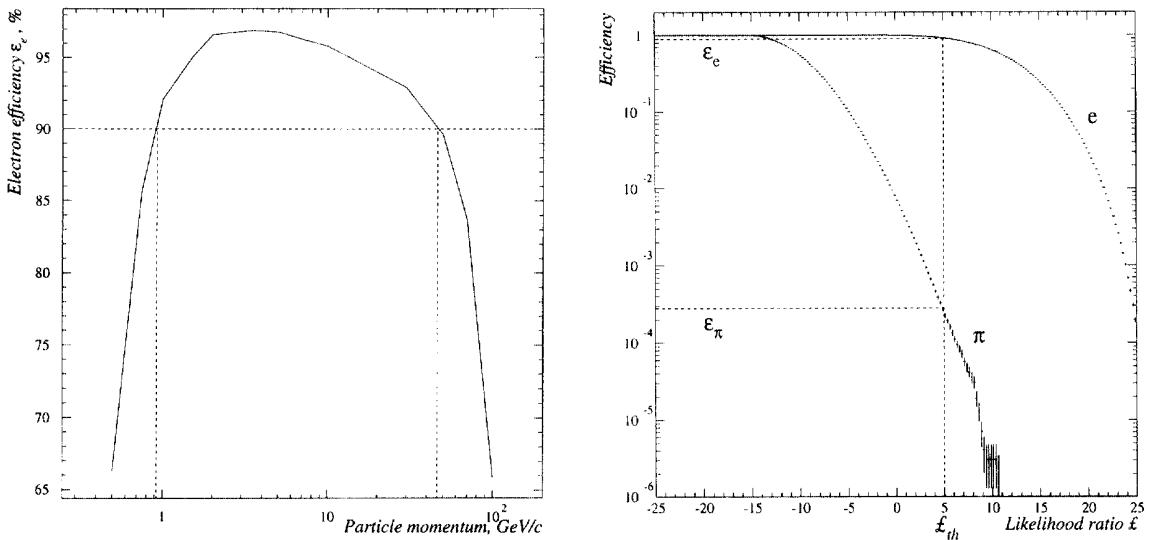


Figure 50: Electron identification with transition radiation (TR) in NOMAD. Left panel: e^\pm efficiency as a function of momentum for a fixed π rejection factor of 10^{-3} . Right panel: e^\pm and π^\pm efficiencies as a function of the TR discriminant variable.

At lower electron energies the use of TR for e^\pm identification is complemented by the measurement of the ionization dE/dx in the active volume of the straws. Multiple measurements from all the straws crossed by the charged track are combined in order to achieve a good identification efficiency. Additional handles for e^\pm identification are the matching of the charged tracks with ECAL clusters and the ECAL shower shape.

The STT offers a 4π detection of photon conversions into e^+e^- pairs, which can be identified using the displaced V_0 vertex and the TR+ dE/dx . The effect of the track bending in the magnetic field allows an excellent e/γ separation, while kinematic cuts on the invariant mass of the e^+e^- pair and on the corresponding opening angle can further enhance the purity.

The measurement of the energy loss dE/dx in the active gas within the straws crossed by the tracks also allows an identification of π^\pm, K^\pm, p stopping hadrons. For protons, the measured range as a function of the momentum provides additional p/π separation.

For e^\pm the limiting factor is the bending/sampling, which prevents the track reconstruction and fitting at low momenta (loopers). It is worth noting that even at very low momenta it is still possible to detect track hits/segments and measure dE/dx , thus identifying/vetoing the e^\pm .

A study of particle identification capabilities of the full system is underway. Protons, Kaons, pions stopping or slowing down in the STT or in the calorimeter can be easily identified through dE/dx and momentum/range relations. For particles escaping the calorimeter, external muon catchers as described in 3.5 will allow to discriminate escaping muons from pions. Quantitative estimates are in preparation.

5.2.1 Optimization of the STT Radiators

The radiators occupy a significant fraction of the space in the STT modules (Fig. 12). The design of the radiators has to satisfy opposite requirements: (a) maximize the production of TR to guarantee an efficient electron ID; (b) minimize the total thickness of the STT modules in order to better exploit the limited space available inside the KLOE magnet.

We performed a detailed optimization of the radiator design by simulating the TR production by electrons of various energies. To this end, the TR performance is optimized using 1 GeV electrons, which are representative of the main oscillation peak expected in DUNE. For each radiator configuration we simulate 10 consecutive identical STT modules to check build-up effects in the TR detection and to calculate the corresponding average response. The straw geometry is fixed, with 4 XXYY layers and a gas mixture of Xe/CO₂ 70/30, as shown in Fig. 12.

The first step is to select the minimal number of radiator foils (and hence the total radiator thickness) required to detect close to one TR photon per module. At this stage we keep the air gaps between consecutive foils fixed at 120 μm . Figure 53 shows that with $N = 150$ we can get a relatively compact radiator of about 20 mm, still retaining about 0.95 photons detected per module. This latter number can be further increased by increasing the gas pressure inside the straw to 1.9 atm (Fig. 54).

The second step of the optimization is to vary the thickness of both the air gaps and the radiator foils by keeping the total radiator thickness constant at about 20 mm. To this end, we effectively vary the air gaps by changing the number of radiator foils. As shown in Fig. 55, the TR response saturates for $N \geq 150$. Finally, when we vary the thickness of the radiator foils we find a clear peak in the TR response for $15 \mu\text{m} \leq \Delta \leq 18 \mu\text{m}$ (Fig. 56). We therefore conclude that the optimal compromise for the radiator design is

Module #	Electrons E=1.0 GeV			Electrons E=5.0 GeV		
	> 3.0 keV			> 3.0 keV		
	> 4.0 keV	> 5.0 keV	keV	> 3.0 keV	> 4.0 keV	keV
1	0.93	0.89	0.80	1.09	1.04	0.94
2	0.97	0.93	0.84	1.13	1.08	0.98
3	0.98	0.94	0.85	1.15	1.10	1.00
4	0.99	0.95	0.86	1.16	1.11	1.01
5	0.99	0.95	0.86	1.16	1.11	1.01
6	0.99	0.95	0.86	1.16	1.11	1.01
7	0.99	0.95	0.86	1.16	1.12	1.01
8	0.99	0.95	0.86	1.16	1.12	1.02
9	0.99	0.95	0.86	1.17	1.12	1.02
10	0.99	0.95	0.86	1.17	1.12	1.02
Total	9.81	9.41	8.52	11.51	11.03	10.01

Table 10: Average number of Transition Radiation photons detected in the straws (4 XXYY layers) for different energy thresholds. The result of the simulation of 10 consecutive STT modules equipped with radiators and a 5 mm CH₂ target plate (Fig. 12) is shown together with the corresponding total TR detected. The straw operating conditions assumed are a Xe/CO₂ gas mixture at 1.9 atm.

to have 150 foils 15 μm thick, separated by 120 μm air gaps, with straws operated at an internal pressure of 1.9 atm.

5.3 Full event reconstruction

A full realistic event reconstruction is based only on detected quantities, avoiding to use MC *true* informations (vertex position, number and nature of generated particles, trajectories, and so on). This full reconstruction has been performed on samples simulated with the FLUKA code, assuming the DUNE-neutrino beam and interactions both in the LAr target and in the STT volume. As a preliminary step of the procedure, the hits on each STT layer ($x - z$ and $y - z$) are grouped together, on the basis of the assumed spatial resolution (200 μm), to obtain the *STT digits* (STT-hits hereafter) on both views.

After the hit *digitisation*, a first rough reconstruction of the neutrino-interaction vertex is performed on both views separately, based on topology criteria, that is on the spread profile of the STT-hits normalised to the hit-number as a function of the layer z -coordinate. This first (*step 0*) vertex position estimate is used for the subsequent track-finding algorithm: it is a global algorithm based on the coordinate transforms. In the $y - z$ view the transforms are

$$z \rightarrow u = \frac{+z - z_V}{(z - z_V)^2 + (y - y_V)^2} \quad y \rightarrow v = \frac{-y + y_V}{(z - z_V)^2 + (y - y_V)^2}$$

where z_V and y_V are the coordinates of the reconstructed vertex. Similar transforms are used in the $x - z$ view. In the transformed-coordinate plane, the curved trajectories originating in (z_V, y_V) or in (z_V, x_V) become straight lines crossing the origin $(u, v) = (0, 0)$. Thus, the 2-dimensional track-finding in each view becomes a 1-dimensional search for the peaks on the distribution of the variable $\phi = \text{atan}(v/u)$. Each peak is related to a track, thus allowing the association of the STT-hits to the particle trajectories. Then the hits related to a possible track are fitted in each view. More precise the vertex reconstruction is, more easily the ϕ -peaks will be identified, then better will be the track-hits association and the resulting track fit.

After the fit of the tracks, a new estimate (*step 1*) of the interaction vertex is obtained from the crossing of the couple of tracks with greatest rigidity. Fig. 57 shows the uncertainty on the vertex reconstruction in the $x - z$ view and in the space (from both the views) at *step 0* and *step 1*. A clear improvement (lower mean value, more events with distance within 5 cm) is visible at *step 1* where the rigid-tracks crossing is used. The uncertainties on the different axes are shown in Fig. 58.

As an example to illustrate the procedure, Fig. 59 includes a MC event with a neutrino resonant interaction in the STT radiator: in the left panels, the full MC event in the $y - z$ and $x - z$ views is shown, while the right panels show the same event as it appears after STT-hit digitisation.

For such event, the vertex is well reconstructed since *step 0*, thus allowing a good identification of ϕ peaks and the proper hits-track association, as illustrated in the plots of Fig. 60. The three charged-particle tracks in the event are clearly fully reconstructed (the fit parameters are also reported in the left bottom plot).

In Fig. 61, the number of tracks reconstructed in each view through the above described procedure is compared with the *true* multiplicity of charged particle tracks (requiring at least three STT-hits), for the LAr-target interaction sample. In particular, the right plot refers to the sub-sample of quasi-elastic neutrino interactions. As can be seen, about half of events in such sub-sample contain a single charged track. Such fraction is a little bit higher when the reconstructed tracks are considered.

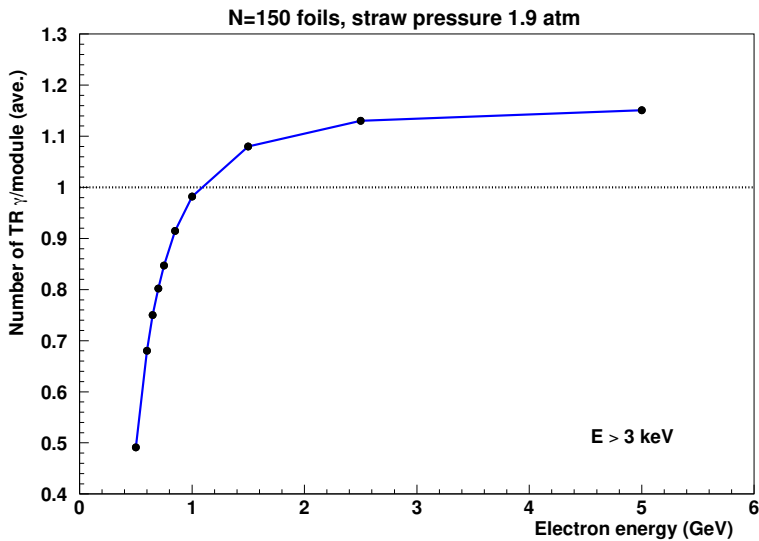


Figure 51: Number of detected TR photons in the straws (averaged over 10 consecutive modules as in Fig. 12) as a function of the electron energy. The straw operating conditions assumed are a Xe/CO₂ gas mixture at 1.9 atm and an energy threshold of 3 keV is applied.

The circular fit of tracks in the $y - z$ view allows to reconstruct the particle-momentum component in the bending plane (p_{yz}). The resulting percentage error track-by-track is shown in Fig. 62. In order to fully reconstruct the particle momentum, the dip-angle estimate is also needed (see Sec. 5.1.1), which requires an unambiguous match of the tracks in the two views. This can be easily obtained in the case of a single track reconstructed in $x - z$ and $y - z$ view. Therefore a single-track sub-sample was firstly considered for a first check of the reliability of this full-event reconstruction. The related resulting percentage errors on p_{yz} , dip-angle and p are shown in Fig. 63.

5.4 CC events

Since DUNE will be exposed to wide-band neutrino beam, the neutrino energy resolution of the near detector is a key feature in order to fulfill the experimental physics goals. In order to evaluate the energy resolution about 50k muon neutrino CC interaction in the liquid argon meniscus has been generated using GENIE. The optimized flux presented at Oct 2017 Beam Optimization Review has been used [1]. The detector response to produced particles has been simulated using *Edep-sim* and a custom digitization process. The particle identification exploits the MC truth.

The STT digits of each track are grouped using the MC truth and then fitted applying least-squares method. The track model is a circle in the $z - y$ plane perpendicular to the magnetic field [77] and a straight line in $\rho - x$ plane as defined in [14]. The track is so described by seven parameters: the circle center (z_c , y_c), the radius (R), the initial angle (ϕ_0), the sense of rotation of the circle ($h = \pm 1$), the initial x coordinate (x_0) and the dip angle (λ). Consequently the particle momentum is evaluated as:

$$\begin{aligned} p_\perp &= 0.29979 \cdot B \cdot R \\ p_x &= p_\perp \cdot \tan \lambda \\ p_y &= p_\perp \cdot \sin \phi_0 \\ p_z &= p_\perp \cdot \cos \phi_0 \end{aligned}$$

Neutrons, neutral pions and photons are reconstructed mainly using the information provided by the electromagnetic calorimeter. Time and charge of the two photomultiplier reading out the same cell are combined to obtain the energy deposit, time and longitudinal position of the hit. The hit transverse coordinate is given by the cell position. The calorimeter performances in term of time and electromagnetic energy resolution, as measured in [7], are well reproduced. The calorimeter hits related to the same particle are grouped in cluster using the MC truth. The momentum of the neutron originating from the neutrino interaction is obtained measuring its velocity. The path and time of flight is measured by the difference between the time and position of the interaction and the ones of the earlier calorimeter hit related to the neutron. Neutral pions momentum and energy are obtained by the ones of the daughter photons. The photons energy and direction are obtained either by measurements of electron and positron in case the photon converts before reaching the calorimeter or by the cluster of hits produced in the calorimeter. In the latter case, the photon energy is obtained by the sum of the deposited energy over the cluster and the direction is reconstructed linear fitting the deposited energy weighted averaged position evaluated layer by layer.

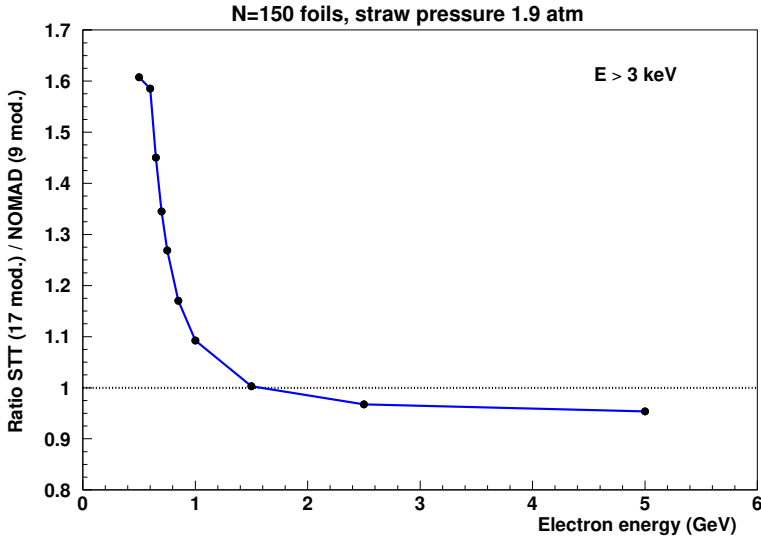


Figure 52: Ratio between the total number of TR photons detected in 17 consecutive STT modules as in Fig. 12 and the corresponding one in the complete NOMAD transition radiator detector (9 modules) as a function of the electron energy. The straw operating conditions assumed for STT are a Xe/CO₂ gas mixture at 1.9 atm and an energy threshold of 3 keV is applied.

The neutrino energy is obtained summing up the kinetic energy of nucleons, assuming they are nuclear remnants, and the total energy of all the other particles. Comparing with the true values and fitting the gaussian part of the residual distribution, a resolution of about 6% is obtained. The deviation from gaussianity and the asymmetry is probably caused by the circular fit of the track which systematically underestimates the particle momentum.

6 Expected Physics Performance

In Sec. 5 we used a full detector simulation to estimate the performance of the neutrino event reconstruction and the corresponding achievable resolutions. We can now perform sensitivity studies of the key physics measurements for the long-baseline analysis described in Sec. 2.1. To this end, we use a fast simulation for signal and background processes based upon parameterized resolutions and reconstruction effects, which are consistent with the results of Sec. 5.

6.1 Measurements of $\nu(\bar{\nu})$ -Hydrogen Interactions

The study (anti)neutrino scattering on hydrogen (free proton) with the STT is crucial for the DUNE ND physics potential (Sec. 2.1) since this is the only type of interactions, together with the ν -e elastic scattering discussed in Sec. 6.2, to be free from nuclear effects. To this end, the use of the CH₂ radiators inside STT is the only opportunity realistically available for DUNE ND [39], given the safety issues related to the use of liquid or gaseous H targets in an underground ND hall. The main issues to clarify are whether the interactions on H can be identified unambiguously and what are the corresponding uncertainties from the subtraction of backgrounds originated from the heavier C nucleus in the radiator targets.

The excellent angular, momentum, vertex, and timing resolutions of STT allow a precise location of the interaction vertex in the different target materials. Since the radiators provide about 95% of the total STT mass, the impact of the straws is negligible even for single track events (99% purity in associating 1-track events to radiators). However, the H content by weight in the radiator targets is only 14.4% of the total. Although this is about the highest H content from plastic materials, most of the interactions from the STT radiators are still originated from the C nucleus.

In order to improve the signal/background ratio in the selection of H events, we consider the complete event kinematics [39]. Since the H target is at rest, the CC events are expected to be perfectly balanced in a plane transverse to the beam direction (up to the tiny beam divergence) and the muon and hadron vectors lie in the same plane. Instead, events from nuclear targets are largely affected by the Fermi motion and binding, as well as from final state interactions within the nucleus, resulting in a significant missing transverse momentum. To illustrate the rejection power achievable with a kinematic selection, we show the results for one exclusive CC topology with 3 tracks $\mu^- p\pi^+$, mainly from resonance production (resonance events are 68% of total neutrino interactions on H, corresponding to about 2.4×10^6 events in STT). The most discriminating variable is $R_{MH} = (p_T^m - p_T^H)/(p_T^m + p_T^H)$, the asymmetry between the missing transverse momentum, p_T^m , and the transverse momentum of the hadron system, p_T^H . Since the missing

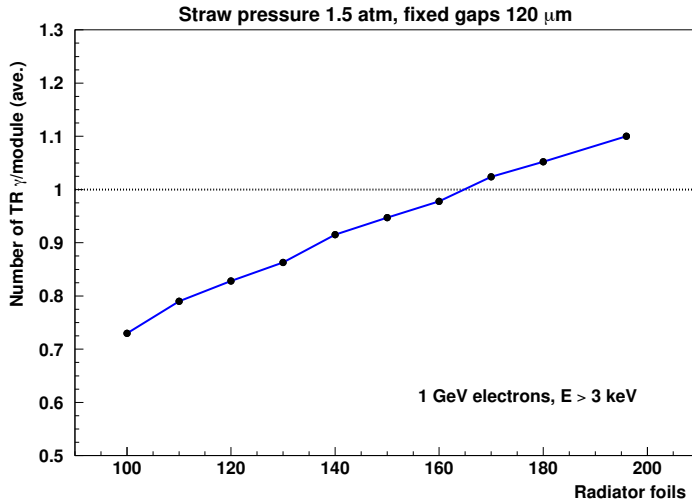


Figure 53: Number of TR photons detected per STT module (averaged over 10 consecutive modules) as a function of the total number of CH_2 foils in the radiator for 1 GeV electrons. A fixed air gap of $120 \mu\text{m}$, $15 \mu\text{m}$ thick foils, a gas mixture Xe/CO_2 70/30 at 1.5 atm, and a threshold $E > 3 \text{ keV}$ are used.

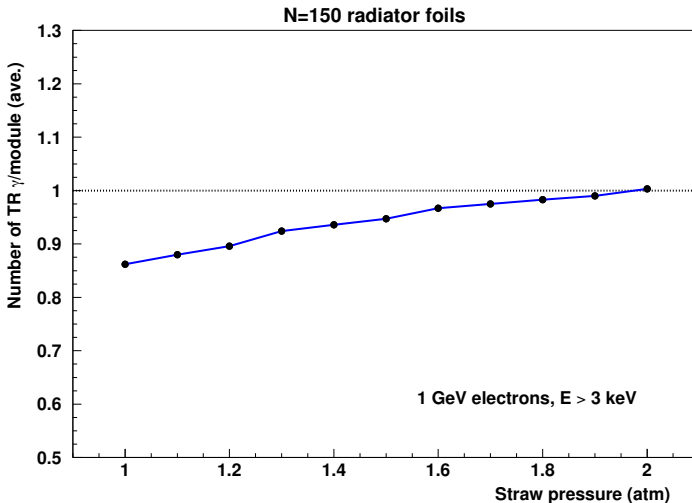


Figure 54: Number of TR photons detected per STT module (averaged over 10 consecutive modules) as a function of the operating gas pressure inside the straws for 1 GeV electrons. A fixed number of foils $N = 150$ $15 \mu\text{m}$ thick, air gaps of $120 \mu\text{m}$, a gas mixture Xe/CO_2 70/30, and a threshold $E > 3 \text{ keV}$ are used.

transverse momentum is mainly generated inside the hadron system due to the nuclear effects, it is expected to be highly correlated with the latter. Another useful variable is the magnitude of the component of the hadron transverse momentum perpendicular to the transverse momentum of the lepton, $p_{T\perp}^H$. Interactions on H are characterized by a sharp peak around zero in $p_{T\perp}^H$, while interaction from the C nucleus have a much broader distribution originating from the nuclear smearing. The use of simple cuts $R_{MH} < -0.6$ and $|p_{T\perp}^H| < 0.03 \text{ GeV}/c$ provides a clean selection of H interactions from radiator targets with an efficiency of 93% and a purity of 86%, including all backgrounds from DIS. Both the efficiency and the purity appear to be rather uniform as a function of the neutrino energy. Similarly, we can select the equivalent $\bar{\nu}_\mu$ CC topology with 3 tracks $\mu^+ p\pi^-$ with a purity of 84% and an efficiency of 89%. Similar results are obtained for antineutrino interactions, as well as for other topologies on H, including DIS events, as summarized in Tab. 11. The selection of H interactions can be further improved using a likelihood function incorporating multi-dimensional correlations among kinematic variables [39]:

$$\mathcal{L}^H \equiv \left[[R_{mH}, p_{T\perp}^H, \theta_{\nu T}], p_T^m, \Phi_{lH} \right] \quad (4)$$

where the square brackets denote correlations, Φ_{lH} is the angle between the transverse momenta of the lepton and the hadron system, and $\theta_{\nu T}$ is the angle of the total visible momentum with respect to the beam direction. As it is common practice, we use the logarithm of the final likelihood ratio between signal and background hypotheses, $\ln \lambda^H$, as discriminant (Fig. 64). The corresponding purity and efficiency achievable in the kinematic H selection as a function of the $\ln \lambda^H$ cut are given in Fig. 65 for both the $\mu^- p\pi^+$ and

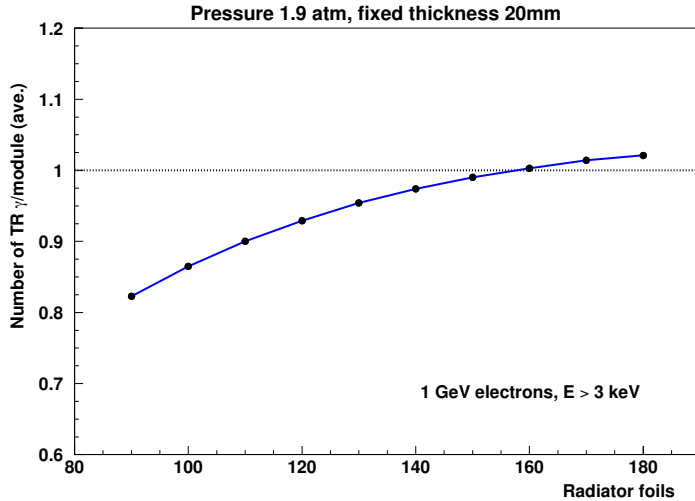


Figure 55: Number of TR photons detected per STT module (averaged over 10 consecutive modules) as a function of the total number of CH_2 foils in the radiator for a fixed total radiator thickness of 20 mm and 1 GeV electrons. The thickness of the air gaps varies according to the number of foils used. A fixed foil thickness of 15 μm , a gas mixture Xe/CO₂ 70/30 at 1.9 atm, and a threshold $E > 3$ keV are used.

Process	R_{mH} and $p_{T\perp}^H$ cuts		$\ln \lambda^H$ cut	
	Efficiency	Purity	Efficiency	Purity
$\nu_\mu p \rightarrow \mu^- p \pi^+$	93%	86%	90%	92%
$\bar{\nu}_\mu p \rightarrow \mu^+ p \pi^-$	89%	84%	90%	88%
$\bar{\nu}_\mu p \rightarrow \mu^+ n$	95%	80%		
$\nu_\mu p$ CC inclusive	83%	73%		

Table 11: Efficiency and purity for the kinematic selection of H interactions from the CH_2 plastic target using simple cuts on R_{mH} and $p_{T\perp}^H$ (described in the text), as well as on the multi-variate likelihood ratio $\ln \lambda^H$. The cuts on $\ln \lambda^H$ are chosen to retain a fixed 90% signal efficiency.

$\mu^+ p \pi^-$ samples.

Another important exclusive process is the quasi-elastic $\bar{\nu}_\mu p \rightarrow \mu^+ n$ from the hydrogen target [39]. As discussed in Sec. 5.1.4, on average about 65% of the neutrons from $\bar{\nu}_\mu$ QE interact either in the KLOE ECAL or within the STT volume. The detected neutron interactions can be associated to the primary vertex thanks to the excellent timing resolution of both the STT and ECAL. This vertex association provides the direction of the detected neutron. We then obtain the neutron energy as $E_n = E_\nu - E_\mu$, by using the QE formula for the neutrino energy as a function of the momentum and angle of the detected muon. Once we reconstruct the momentum vector of the outgoing neutron we can apply a similar kinematic selection of H interactions as described above for the RES $\mu p \pi$ sample. Fig. 66 illustrates the corresponding selection of $\bar{\nu}_\mu$ QE interactions on H based upon simple cuts $R_{mH} < -0.7$ and $p_{T\perp}^H < 0.02$ GeV/c, resulting in an efficiency of 95% and a purity of 80% (Tab. 11).

From Fig. 64 we conclude that the impact of the background subtraction in the selection of H events from the STT radiators is relatively small (< 10% background). Reconstruction effects on the charged tracks can in principle play a role by degrading the event kinematics. However, in H the response function from the true to the reconstructed kinematics is entirely defined by the momentum resolution of the tracks, which is calibrated with good accuracy as discussed in Sec. 3.3.1. Similar kinematic selections were also successfully demonstrated by NOMAD in more severe background conditions (rejections up to 10^5) in various published analyses [20, 62, 19]. We note that the normalization of the H signal and the C background is based upon the corresponding fractional weights in CH_2 , thanks to the high chemical purity (100%) of the CH_2 and C targets and to the STT accuracy in associating the interactions to the targets.

Although the interactions on H are free from nuclear effects, the subtraction of the background from C interactions can in principle be affected by the nuclear modeling. Fig. 67 shows that a substantial smearing is introduced by nuclear effects on the reconstructed energy. In order to reduce the related systematic uncertainties we perform a model-independent background subtraction using the dedicated graphite target in STT. The final H sample is therefore obtained from the difference between the events from the CH_2 radiators and the events from the graphite target, normalized to the fraction of C content in the radiator targets. Indirect effects from the acceptance corrections in the graphite targets are negligible since the acceptance is already a second order correction on a small data-driven subtraction.

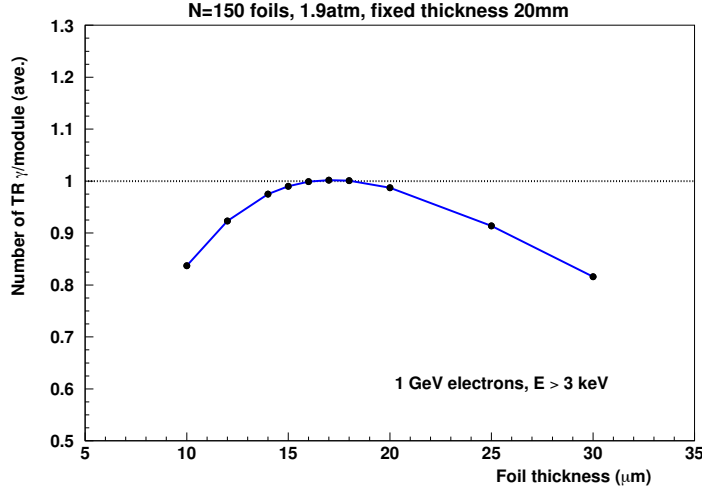


Figure 56: Number of TR photons detected per STT module (averaged over 10 consecutive modules) as a function of the thickness of the radiator foils for a fixed total radiator thickness of 20 mm and 1 GeV electrons. The thickness of the air gaps varies slightly according the thickness of the foils used. A fixed number of foils $N = 150$, a gas mixture Xe/CO₂ 70/30 at 1.9 atm, and a threshold $E > 3$ keV are used.

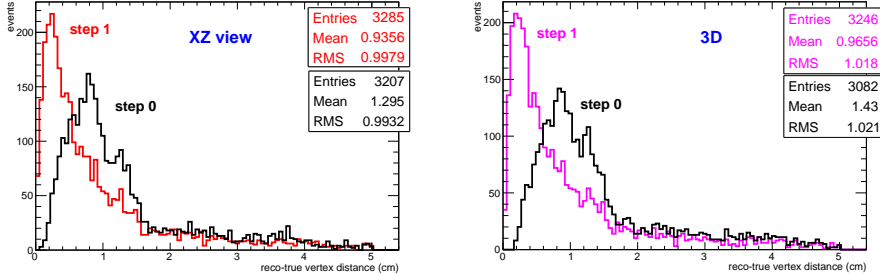


Figure 57: Fluka simulation, STT target - Uncertainty on the vertex reconstruction at *step 0* and *step 1*. Left panel: $x - z$ view. Right panel: 3-dimensional space.

6.1.1 Determination of Relative and Absolute Fluxes

For the determination of the relative flux as a function of energy the interactions on H (free proton) offer a unique tool free from nuclear smearing [40].¹ The simplest topology available in ν -H interactions is the process $\nu_\mu p \rightarrow \mu^- p\pi^+$, dominated by resonance production. Since all final state particles can be accurately reconstructed in the STT, the unfolding of the detector response is controlled by the momentum resolution $\delta p/p \sim 3\%$. These features make the $\nu_\mu p \rightarrow \mu^- p\pi^+$ topology an excellent tool for the determination of the relative ν_μ fluxes as a function of E_ν , using the absolute normalization from ν -e scattering (Sec. 6.2).

The relevant model uncertainties are the ones affecting the energy dependence of the RES cross-section on hydrogen, which is controlled by the proton form factors. These uncertainties are substantially smaller than in any nuclear target, due to the absence of nuclear effects. To estimate such uncertainties we consider the $\nu_\mu p \rightarrow \mu^- p\pi^+$ process on H and vary the axial mass by $\pm 20\%$ and the vector mass by $\pm 10\%$. The resulting uncertainties on the flux shape are of the order of 2-5% depending upon the energy. We can further reduce such uncertainties by restricting our analysis to events with low hadronic energy ν . Given the typical invariant mass of resonant processes, cuts down to $\nu < 0.5$ GeV are feasible. This effect arises from the flattening of the energy dependence of the RES cross-section at $\nu < 0.5$ GeV, associated to the reduced phase space, which is pushing the residual rise at energies lower than the range of interest for the flux measurement. As a result, the uncertainty on the energy dependence (NOT on the absolute cross-section, the overall normalization requires ν -e elastic) is reduced at the sub-percent level. The effect is similar to the usual low- ν technique, but here we have a single exclusive process with a well defined cross-section. The overall efficiency of the cut $\nu < 0.5$ GeV on the reconstructed hadronic energy is about 25% for the $\mu^- p\pi^+$ topologies on H, resulting in a total of 560,000 events expected in the flux sample. The kinematic selection described in Sec. 6.1 and the cut $\nu < 0.5$ GeV suppress resonances higher than $\Delta(1232)$ and non-resonant backgrounds. As a result, in the sample used for the relative flux determination 96.6% of the events have $W < 1.35$ GeV, 0.02% originate from higher mass resonances, and about 3.4% from non-resonant

¹Elastic scattering off electrons (mainly NC) can also provide complementary information free from nuclear effects (Sec. 6.2). However, the substantially smaller statistics and the additional smearing associated to the outgoing neutrino and the beam divergence limit the physics sensitivity of this channel to the relative fluxes.

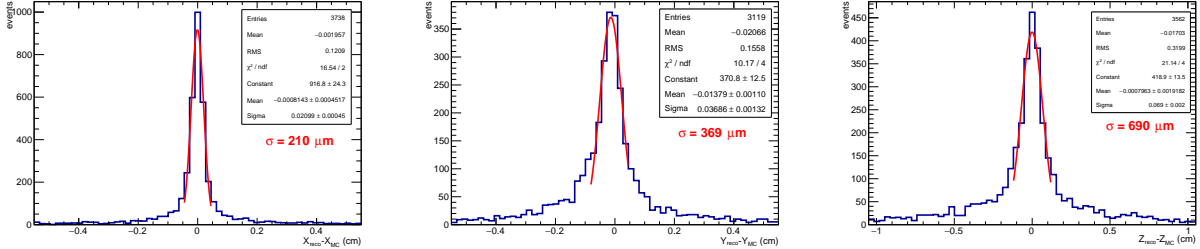


Figure 58: Fluka simulation, STT target - Uncertainty on the vertex reconstruction at *step 1* on x , y and z axes.

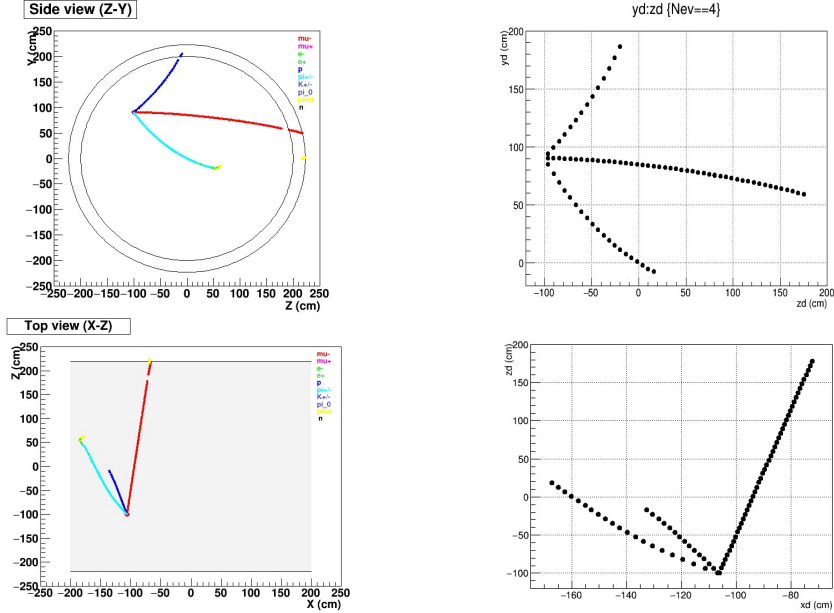


Figure 59: Fluka simulation - Event with a muon-neutrino resonance interaction in the STT radiator as it appears in the MC display (left upper and lower panels) and after STT-hit digitisation in the $y - z$ (right upper panel) and $x - z$ (right lower panel) view.

contributions, according to the GENIE simulations. Comparable results are obtained using the GiBUU and NuWro generators.

Since hadronic uncertainties are greatly reduced by using interactions on hydrogen with small energy transfer ν , one of the dominant systematic uncertainties on the relative flux determination is associated to the muon energy scale. As discussed in Sec. 3.6, we can calibrate the momentum scale of charged particles with the mass peak of the large samples of reconstructed $K_0 \rightarrow \pi^+ \pi^-$ decays. In our study we assume the same muon energy scale uncertainty of 0.2% achieved by the NOMAD experiment [80]. We note that STT would provide 25 time higher granularity than NOMAD and about 40 times higher K_0 statistics. To estimate the effects of the hadronic energy reconstruction on the flux measurements we consider a realistic detector smearing and event selection from Sec. 6.1. The acceptance for individual final state particles (p, n, π, μ) is folded into the analysis and the reconstruction smearing on the hadronic energy is evaluated as a function of ν . In addition to the detector response and event selection, we vary the ν cut applied to define the flux samples according to the expected resolution around the cut values.

The statistical and systematic uncertainties expected on the relative $\nu_\mu p \rightarrow \mu^- p \pi^+$ interactions on H are shown in Fig. 68 for both the low energy and high energy beam options considered. In the former case we use a cut $\nu < 0.5$ GeV, while in the latter a higher cut $\nu < 0.75$ GeV turns out to be more appropriate. In the energy ranges where we expect the bulk of the fluxes the total uncertainties – including both the statistical and systematic ones added in quadrature – are well below 1%. The level of accuracy on the flux determination demonstrated in Fig. 68 cannot be achieved by other known techniques using nuclear targets.

We have shown that even large variations of the form factors correspond to negligible uncertainties on the relative flux determined from RES $\mu p \pi$ at $\nu < 0.5$ GeV. However, we emphasize that we will directly measure the corresponding $\nu(\bar{\nu})$ -H form factors and cross-sections in STT from the reconstructed Q^2 distribution of

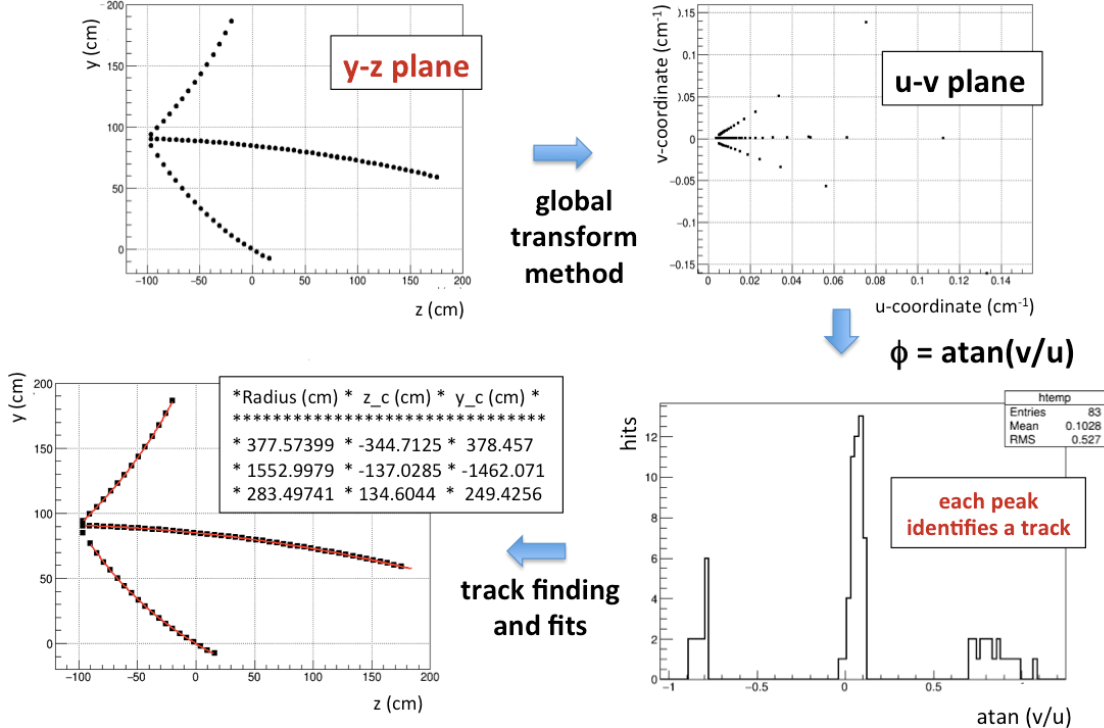


Figure 60: Full reconstruction of the event already shown in Fig. 59: the vertex is well reconstructed at *step 0* (left upper panel), the coordinate-transforms (right upper panel) allow the identification of ϕ peaks (right bottom panel) and the proper hits-track association. Finally the event is fully reconstructed and the track-fit parameters are reported in the left bottom panel.

the full $\nu_\mu p \rightarrow \mu^- p\pi^+$ sample without ν cut. Since form factors are expected to be a function of Q^2 , any modification affecting the energy dependence of the cross-section relevant for the relative flux determination would manifest as a distortion in the measured Q^2 distribution. The total statistics expected is about 2.24×10^6 selected $\mu^- p\pi^+$ events on H, providing a stringent test against arbitrary model variations. The sensitivity of the measured Q^2 distribution – including statistical and systematic uncertainties added in quadrature – to model variations is illustrated in Fig. 69 (right plot) for the $\nu_\mu p \rightarrow \mu^- p\pi^+$ sample on H. The same variations of form factors resulting in sub-percent uncertainties on the relative fluxes (Fig. 68) produce large changes in the shape of the measured Q^2 distribution: changing the axial mass by +20%(-20%) results in a χ^2/dof of 1464/60 (1187/60). The difference between the GENIE and GiBUU implementations is also distinguishable (χ^2/dof of 2211/60). It is worth noting that the fraction of overlap events between the flux sample with $\nu < 0.5$ GeV and the total sample is less than 25%, allowing a robust in-situ measurement of form factors.

The exclusive $\bar{\nu}_\mu p \rightarrow \mu^+ n$ QE process on hydrogen allows an accurate determination of the $\bar{\nu}_\mu$ relative flux. As discussed in Sec. 6.1, $\bar{\nu}_\mu$ QE on H can be efficiently selected by using the neutrons interacting either in the STT volume or in the KLOE ECAL. For the measurement of the relative $\bar{\nu}_\mu$ flux as a function of energy we can use a cut $\nu < 0.25$ GeV in a way similar to the one described above for the channel $\nu_\mu p \rightarrow \mu^- p\pi^+$. This cut flattens the energy dependence of the cross-section and dramatically reduces the corresponding hadronic uncertainties level. We expect a total of about 812,000 reconstructed QE events on H, out of which 617,000 have $\nu < 0.25$ GeV (76% efficiency for the cut $\nu < 0.25$ GeV). The model uncertainties on the relative flux can be directly constrained by extracting the relevant (effective) form factors from the measured Q^2 distribution (Fig. 71). The overlap with the flux sample can be reduced below 50% with a lower cut $\nu < 0.1$ GeV. The large statistics of the complete reconstructed QE sample without the ν cut provides a good sensitivity to constrain arbitrary model variations, following the same approach discussed above for the channel $\nu_\mu p \rightarrow \mu^- p\pi^+$. Figure 71 (right plot) illustrates this sensitivity: changing the axial mass by +20%(-20%) results in a χ^2/dof of 828/30 (291/30).

The process $\bar{\nu}_\mu p \rightarrow \mu^+ n$ QE on H can also be used for the absolute $\bar{\nu}_\mu$ flux in the limit $Q^2 = 0$. In this kinematic regime the QE cross-section becomes independent of energy and is completely defined by the neutron β -decay to a precision $\ll 1\%$. The analysis determines the cross-section limit from low Q^2 events. We note that neutrons can be detected in STT up to a lower threshold than protons, thus enhancing the reconstruction efficiency of $\bar{\nu}_\mu$ QE on H at very small Q^2 values. The available statistics in STT results in about 135,000 $\mu^+ n$ reconstructed events with $Q^2 < 0.05$ GeV 2 (corresponding to $\nu < 27$ MeV). The measurement of the absolute $\bar{\nu}_\mu$ flux using the QE interactions on H requires a calibration of the neutron detection efficiency, which can be performed using dedicated test-beam exposures.

Table 2 shows that we expect a sizable statistics of ν_e CC in FHC and $\bar{\nu}_e$ CC in RHC from the hydrogen

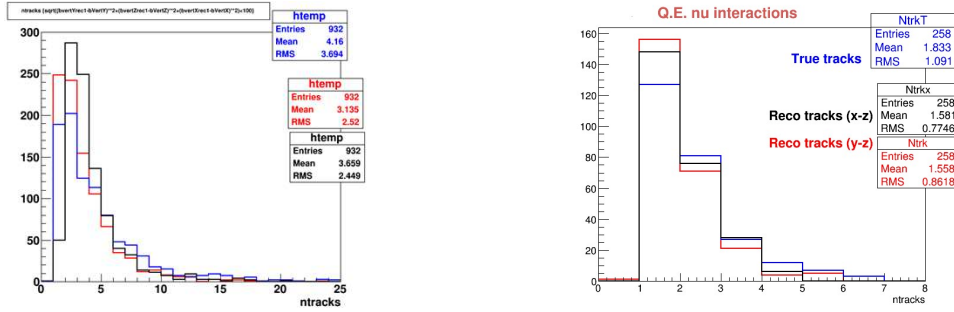


Figure 61: Fluka simulation, LAr meniscus - Multiplicity of reconstructed tracks using the procedure described in the text, compared with the MC charged particle multiplicity (requiring STT-hits ≥ 3). In the right plot the same comparison is shown for the quasi-elastic interaction sample.

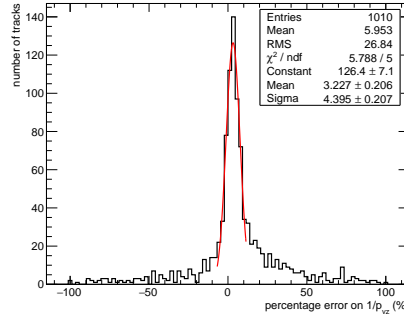


Figure 62: Fluka simulation, LAr meniscus - Percentage error on p_{yz} for each reconstructed track in the bending plane, for events with no more than three tracks.

target. Using the same kinematic selection of interactions in H as the one described for ν_μ and $\bar{\nu}_\mu$, we can measure the ν_e/ν_μ and $\bar{\nu}_e/\bar{\nu}_\mu$ flux ratios on hydrogen. Overall, we select 22,000 identified ν_e CC in FHC and 14,000 identified $\bar{\nu}_e$ CC in RHC. The measurements of ν_e/ν_μ and $\bar{\nu}_e/\bar{\nu}_\mu$ on H are complementary to the ones using the full radiator target described in Sec. 6.4 and provide a precise constraint of the integrals, as well as a verification of the cancellation of nuclear effects in the ratios.

6.1.2 Constraining the Nuclear Smearing in Ar

Nuclear effects play a major role in all oscillation measurements from the FD. The use of a heavy Ar target results in a large smearing of the reconstructed particles and energy from both primary and final state interactions (FSI). Significant uncertainties are associated to the modeling of such effects (especially on FSI), as can be seen from the wide range of predictions obtained using different event generators. Understanding the nuclear smearing and constraining the corresponding uncertainties on the FD analysis require multiple nuclear targets different from Ar in the ND (Sec 2.2).

In Sec. 2.1.2 we outlined the STT strategy to determine the nuclear smearing in Ar from detailed comparisons between interactions from the active Ar target (Sec. 3.3.2) and the hydrogen target (Sec 6.1), for which $R_{\text{phys}} \equiv 1$. The use of the additional Ca target would allow a complete characterization of the nucleus with $A = 40$. An important requirement for such measurements is that the detector response (acceptance) R_{det} is similar for Ar and H interactions. We found that the acceptance and resolutions for various particles are similar for events originated in the active LAr meniscus and in H (Sec.5.1.1). This result can be understood with the geometry of the LAr meniscus, which is arranged in a thin plane $\sim 1X_0$ followed by the STT tracking modules.

In Sec. 2.1.2 we outlined the measurement strategy to constrain the nuclear smearing in Ar by using reconstructed events from the active Ar target and H in STT. The first step is to compare the inclusive CC samples in order to determine $\sigma_{\text{Ar}}R_{\text{phys}}$. Fig. 73 quantifies the impact of various nuclear effects in Ar on the reconstructed neutrino energy in STT. The effects are large and result in substantial distortions of the measured spectrum. As expected, the measurement on hydrogen is close to the true neutrino energy spectrum since the effect of the detector smearing (mainly $\delta p/p$ known to 0.2%) is below 5%. We note that non only the largest smearing occurs in the region most sensitive to the oscillations, $0.5 < E_\nu < 5$ GeV, but this effect is rapidly changing as a function of energy. A comparison between Ar and H interactions offers a unique tool to measure $\sigma_{\text{Ar}}R_{\text{phys}}$ and constrain this important smearing.

In STT we can also constrain separately σ_{Ar} and R_{phys} by using a complete set of kinematic variables

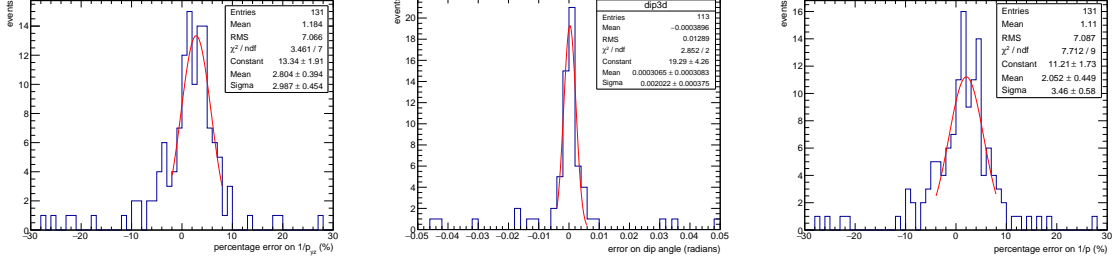


Figure 63: Fluka simulation, LAr meniscus - Percentage error on p_{yz} (left panel), dip-angle (central panel) and total p (right panel), for the sub-sample of events with a single track reconstructed in $x - z$ and $y - z$ view. The errors are referred to the particles (mainly muons) associated to the track.

Detector	Signal	Backgrounds: ν_e QE	Backgrounds: NC π^0	δ_{stat}	δ_{syst}	δ_{tot}
STT FHC	4,079	3%	2%	1.6%	1%	1.9%
LAr FHC + DUNEprism	$\sim 7,000$	11%	3%	1.2%		$\gtrsim 2\%$

Table 12: Selection of ν -e elastic scattering in the STT and LAr detectors.

(5 kinematic degrees of freedom) sensitive to the nuclear smearing and comparing Ar and H inclusive CC interactions. As illustrated in Fig. 74 for the p_T asymmetry and the angle Φ_{MH} between the missing p_T and the p_T of the hadron vector (simple examples), we have a good sensitivity to the details of the nuclear modeling in Ar.

As discussed in Sec. 2.1.2 , additional constraints on the nuclear smearing in Ar can be obtained from the analysis of exclusive topologies. We can also use the reconstructed charge at the primary vertex, C_{vtx} , to select samples of interactions originated from neutrons and protons in Ar (Fig. 75). A requirement of $C_{\text{vtx}} = 0$ in FHC inclusive ν_μ -Ar CC results in a sample of interactions on neutron with 97-99% purity. Similarly, a selection $C_{\text{vtx}} = +1$ in RHC inclusive $\bar{\nu}_\mu$ -Ar CC results in a sample of interactions on proton with 75-83% purity. The quoted ranges correspond to the model dependence estimated from a comparison between two different generators, GENIE and NuWro, as shown in Fig. 75.

Additional constraints on nuclear effects can be obtained from dedicated measurements of various exclusive topologies using the suite of nuclear targets (H, C, Ca, Ar) in STT:

- Ratios of cross-sections and structure functions for exclusive and inclusive processes;
- Difference $\Delta E = E_{\text{rec}}^\nu(2 \text{ trk}) - E_{\text{rec}}^{\text{QE}}(1 \text{ trk})$ in Quasi-elastic topologies;
- Difference between QE cross-sections determined from 1 track and 2 track samples;
- Differences between the 2 and 3 track samples from Resonance production;
- Backward going pions and protons.

6.2 ν -e Elastic Scattering

The $\nu e \rightarrow \nu e$ elastic scattering offers a purely leptonic process with well understood cross-section to be used for the determination of absolute and relative ν_μ fluxes. The experimental signature is simple with a single forward electron in the final state. The main problem to address is the statistics given the tiny cross-section for this process, requiring a fiducial mass of 5 tons or higher in order to reach a precision on the absolute ν_μ flux around 2%.

The main advantages offered by STT for the measurement of ν -e are:

- Fiducial mass allowing a precise measurement of both absolute and relative fluxes;
- Excellent electron identification with TR and dE/dx ;
- High energy and angular resolution for the kinematic rejection of backgrounds;
- In-situ measurement of background sources to reduce systematics.

The ν -e event selection in STT requires the identification of the outgoing electron with $E_e > 0.15$ GeV, a veto of additional tracks/hits or neutral cluster, and a kinematic cut $E_e \theta_e^2 < 0.0012$ GeV rad 2 . The selection efficiency is about 84% with a total background of 5%, composed of ν_e QE interactions without reconstructed proton (3%) and NC π^0 interactions (2%), as shown in Fig. 76. Table 12 summarizes the results of the STT event selection.

The same process can be also selected in the LAr detector part of the ND complex, which is characterized by a fiducial mass of about 25 tons. The LAr event selection is requiring an identified electron with $E_e > 0.5$

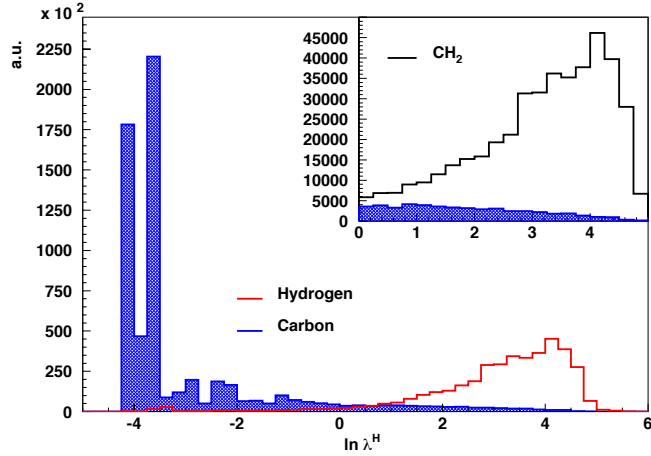


Figure 64: Distributions of $\ln \lambda^H$ for the H signal, the C background, and the CH_2 plastic (sum) for the exclusive $\mu^- p\pi^+$ CC topologies. The multiple peaks are the effect of the binning used to build \mathcal{L}^H . The H and C distributions are normalized to the expected relative abundance in CH_2 .

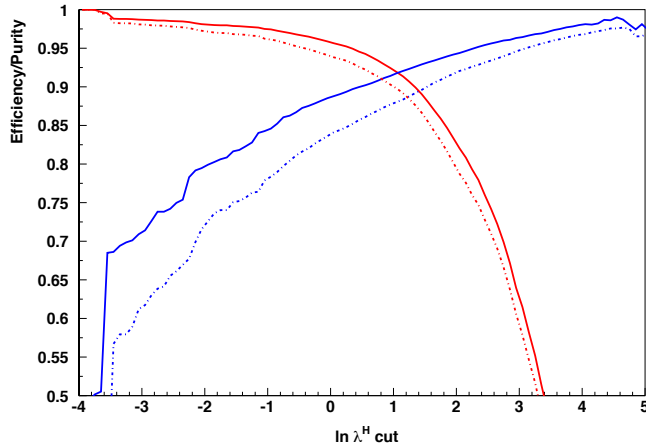


Figure 65: Efficiency (red color) and purity (blue color) as a function of the $\ln \lambda^H$ cut for the kinematic selection of the exclusive $\nu_\mu p \rightarrow \mu^- p\pi^+$ (solid lines) and $\bar{\nu}_\mu p \rightarrow \mu^+ p\pi^-$ (dashed-dotted lines) CC topologies on hydrogen from the CH_2 polypropylene target.

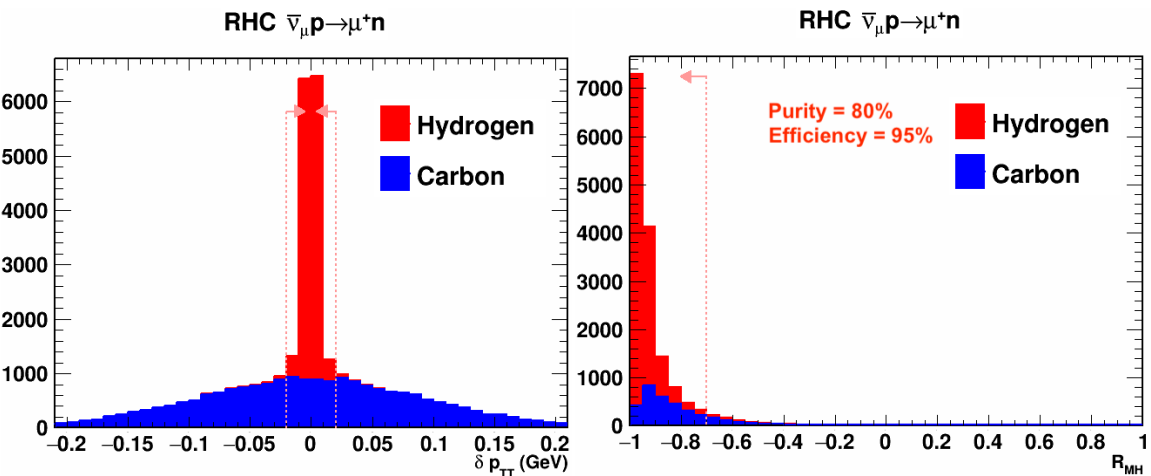


Figure 66: Selection of quasi-elastic $\bar{\nu}_\mu p \rightarrow \mu^+ n$ interactions on hydrogen (free proton) from the polypropylene radiator targets in STT.

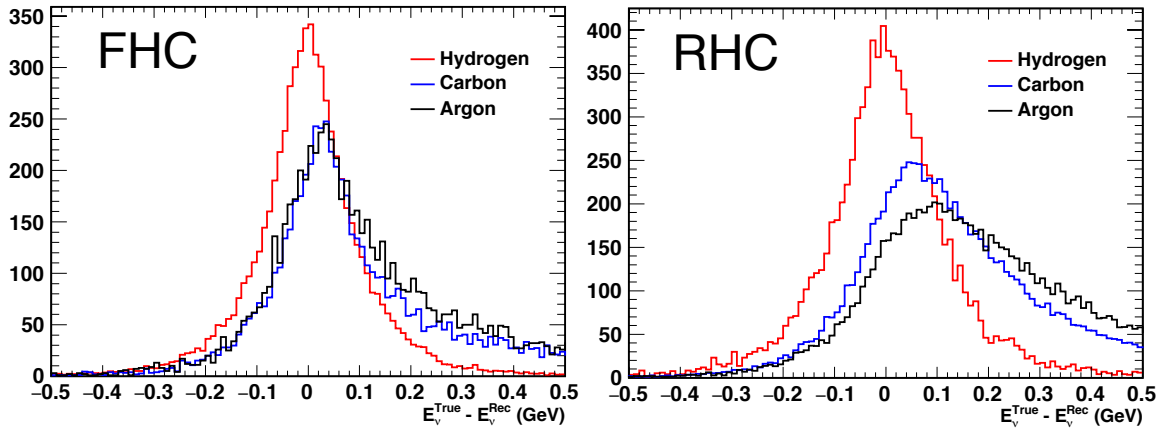


Figure 67: Difference ΔE_ν between the true and reconstructed neutrino energy for selected hydrogen events in STT from FHC neutrino (left panel) and RHC antineutrino (right panel) interactions. The comparison with results from the C (graphite) and active Ar targets in STT illustrates the effect of the nuclear smearing.

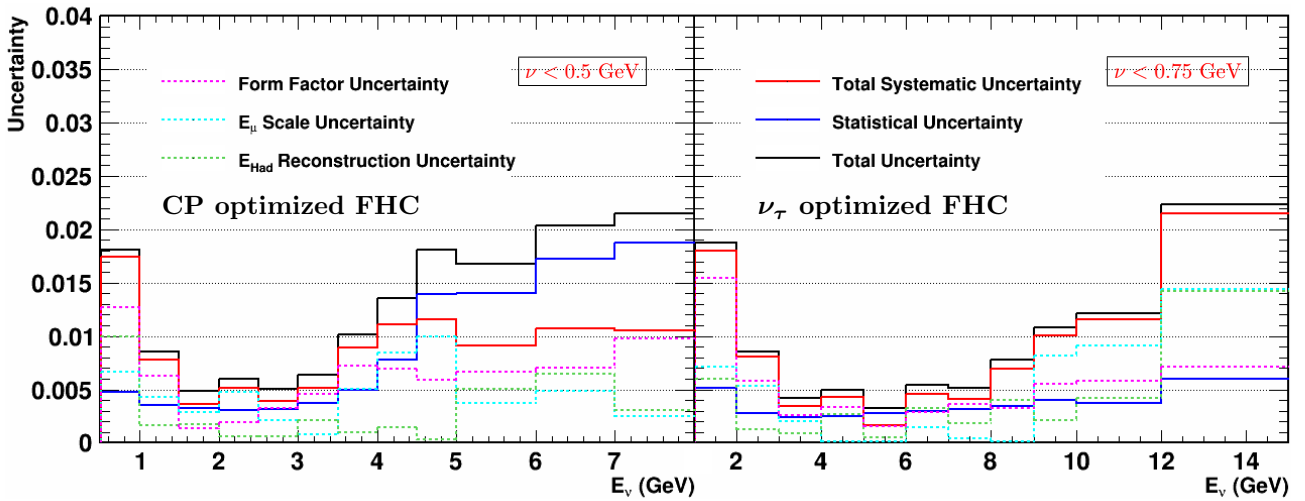


Figure 68: Summary of the expected statistical and systematic uncertainties in the ν_μ relative flux determination using $\nu_\mu p \rightarrow \mu^- p\pi^+$ exclusive processes on hydrogen. Two different input spectra similar to the ones planned in the LBNF are considered: (a) a low-energy beam optimized to search for CP violation (left plot) with a cut $\nu < 0.5$ GeV; (b) a high-energy beam optimized to detect the ν_τ appearance (right plot) with a cut $\nu < 0.75$ GeV.

GeV, a veto of additional activity related to tracks/photons, and a cut $E_e \theta_e^2 < 0.0016$ GeV rad² (Fig. 76). The less stringent kinematic cut in LAr with respect to STT is due to the worse angular resolution (about 4 mrad vs. 2 mrad). Results for the LAr detector are shown in Tab. 12 giving a larger statistics of 11,933 signal events with about 14% backgrounds (11% from QE and 3% from NC). The difference in the event samples between LAr and the STT is smaller than the corresponding ratio of fiducial masses since the ratio of electrons/nucleons is about 27% larger in STT. In addition to the detector resolutions and responses, the higher background levels in LAr can be explained by the fact that in Ar we have about 40% more ν_e CC without visible hadrons than in $(C_3H_6)_n$, due to the larger nuclear effects.

Both the STT and the LAr ν -e samples can be used for the determination of ν_μ fluxes given the sizable statistics. To this end, the most effective method is to perform a template fit to the measured 2D distribution (E_e, θ_e) for the electron to extract the input neutrino energy spectrum. Fig. 77 shows the results obtained from the fits to the STT sample, the LAr sample, and the combined sample STT+LAr, assuming only statistical uncertainties. In the absence of systematic uncertainties the fit is dominated by the LAr statistics and the STT sample adds little information to the combined fit.

We note that the template fit to the (E_e, θ_e) has a substantially better sensitivity by using both the rate and shape information than by using the shape only, suggesting that the overall rate (normalization) plays a major role in this measurement. The statistical precision of the LAr sample is about 0.9% with the detector constantly on-axis, and 1.2% with a partial off-axis data taking like DUNEprism, as seen from Tab. 12. At this level of precisions the systematic uncertainties on signal and backgrounds are expected to dominate the LAr measurement. The assessment of realistic values for the LAr systematics would require dedicated

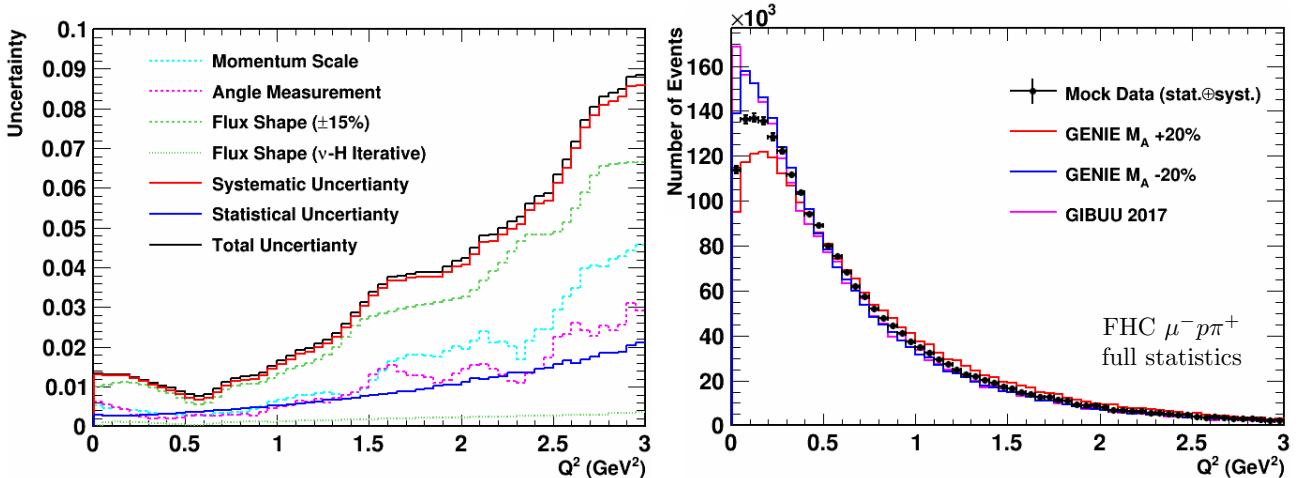


Figure 69: Left plot: expected statistical and systematic uncertainties on the reconstructed Q^2 distribution of $\nu_\mu p \rightarrow \mu^- p\pi^+$ events on H. Two results for the flux uncertainties are shown: (a) using the initial $\pm 15\%$ uncertainty; (b) after an iterative procedure using $\nu_\mu p \rightarrow \mu^- p\pi^+$ on H with $\nu < 0.5$ GeV (Fig. 68). Right plot: reconstructed Q^2 distribution of selected $\nu_\mu p \rightarrow \mu^- p\pi^+$ on H for the complete sample without ν cut. The solid circles (mock-data) correspond to the nominal GENIE cross section and include both statistical and systematic uncertainties added in quadrature (left plot). The sensitivity to a modification of the axial form factor by $M_A \pm 20\%$ is shown for illustration purpose, together with the result of the nominal GiBUU simulation. All distributions are normalized to the same integral.

detector and simulation studies of the technology and is beyond the scope of our current analysis. However, it is instructive to look at the results from similar measurements performed in existing experiments. The ν -e measurement published by MINERνA [79, 65] reports a total systematic uncertainty of 5.1%, dominated by the ν_e QE shape (3.1%) and the electron efficiency (2.7%) and energy scale (1.8%). An independent analysis performed in the NOνA ND gives comparable systematics. While we can expect significant improvements on such uncertainties in the near future, it is unlikely that the LAr systematics will ever be smaller than the STT ones (Tab. 12) considering LAr has one order of magnitude smaller measurement sampling (3.3% vs. 0.19 %), about 15 times higher density and, most importantly, a much heavier target nucleus.

From the previous discussion, we can conclude that the fit is dominated by the rate measurements and that the total uncertainty (including statistics and systematics) on the LAr rates is expected to be similar or worse than the corresponding one for STT. As a result, in realistic conditions the STT provides a valuable contribution to the sensitivity of the combined LAr+STT fit to determine the flux from ν -e and will help to recover the statistics lost with DUNEprism.

Finally, it is worth noting that the contributions of the STT for the ν -e combined fit with the LAr sample are not limited only to the smaller systematic uncertainties in STT. The STT can provide in-situ constraints of the systematic uncertainties affecting the LAr measurements, thus further improving the overall combined sensitivity. The excellent e^\pm identification and charge measurement allows a determination of the π^0 background to ν -e from the wrong sign analysis (e^+ selection). In addition, the measurements described in Sec. 6.1 can constrain nuclear effects on the ν_e CC background.

6.3 Coherent π^\pm Production

Coherent π^\pm production in CC interactions is characterized by a small momentum transfer to the nucleus $|t| < 0.05$ GeV 2 , which remains in its ground state. This channel has a clean experimental signature, with small missing p_T and only a muon and a pion in the final state without any other visible activity. Nuclear effects are much smaller than other channels involving the nucleus.

The ratio of CC coherent π^-/π^+ is an excellent tool for a precise measurement of the $\bar{\nu}_\mu/\nu_\mu$ flux ratio in the beam as a function of energy. Since both interactions have the same experimental signature ($\mu^- \pi^+$ and $\mu^+ \pi^-$, respectively) the systematic uncertainties related to the event selection largely cancel out in such a ratio. A significant cancellation of model uncertainties is also observed. In particular, theoretical models based on the partially conserved axial current (PCAC) theorem, relating the neutrino-nucleus cross section to the pion-nucleus elastic cross section, predict that the neutrino and antineutrino cross-sections are the same for an isoscalar nucleus. Small corrections from interference effects with the vector current are expected in some microscopic models. Coherent π^\pm interactions in the STT radiators occur on isoscalar C nucleus, thus offering a potential reduction of systematics.

The most critical experimental parameter is the resolution on the momentum transfer to the nucleus $|t|$, requiring high momentum and angular resolutions. The fiducial mass of STT provides enough statistics (Tab. 2) for a precise measurement of the wrong sign component of the beam through coherent π production.

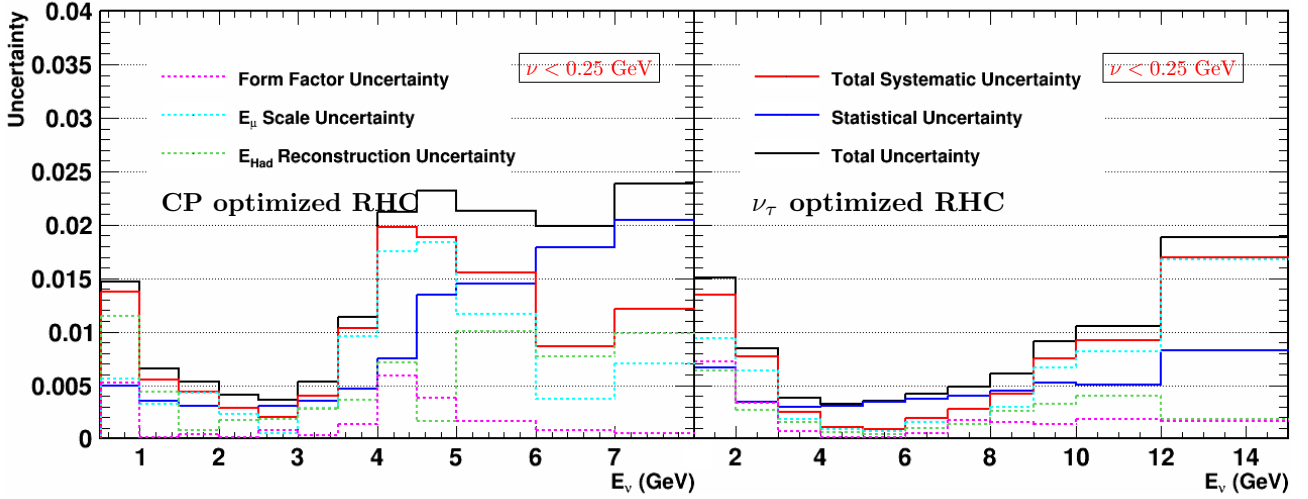


Figure 70: Summary of the expected statistical and systematic uncertainties in the $\bar{\nu}_\mu$ relative flux determination using $\bar{\nu}_\mu p \rightarrow \mu^+ n$ QE exclusive processes on hydrogen. Two different input spectra similar to the ones planned at the LBNF are considered: (a) a low-energy beam optimized to search for CP violation (left plot) with a cut $\nu < 0.25$ GeV; (b) a high-energy beam optimized to detect the ν_τ appearance (right plot) with a cut $\nu < 0.25$ GeV. See text for details.

Fig. 78 shows the corresponding results after the STT selection of coherent π^\pm in the FHC neutrino beam mode. Overall, we can achieve an efficiency of 43% (42%) with a purity of 87% (86%) for coherent $\pi^+(\pi^-)$ in STT. In Fig. 79 we summarize the corresponding precision on the $\bar{\nu}_\mu/\nu_\mu$ flux ratio achievable in STT for both the FHC and RHC beam polarities. The STT measurements offer a powerful in-situ constraint on such flux ratios, substantially reducing the uncertainties obtained from the beam simulations (Fig. 79). It is worth noting that the selection of coherent π^\pm in STT was extensively validated with NOMAD data and indicated a good agreement with MC predictions.

6.4 ν_e/ν_μ & $\bar{\nu}_e/\bar{\nu}_\mu$ Flux Ratios

The oscillation analysis in the FD is based upon a simultaneous fit to both the $\nu_\mu(\bar{\nu}_\mu)$ disappearance and the $\nu_e(\bar{\nu}_e)$ appearance samples. The key quantities to constrain with the ND measurements are then the ratios ν_e/ν_μ and $\bar{\nu}_e/\bar{\nu}_\mu$, which can be measured more precisely than the absolute spectra. It is worth noting that nuclear effects largely cancel out in the ν_e/ν_μ and $\bar{\nu}_e/\bar{\nu}_\mu$ CC ratios as effect of the lepton universality². Fig. 80 shows that the ν_e/ν_μ ratio is the same for $(C_3H_6)_n$ radiator and Ar targets. Lepton universality was also verified in NOMAD with ν_e and ν_μ CC interactions. We can then conclude that an Ar target is not needed for the measurement of ν_e/ν_μ and $\bar{\nu}_e/\bar{\nu}_\mu$. To this end, the use of a light target material in STT offers an advantage in reducing the systematic uncertainties on such measurements.

The STT non only allows a charge measurement of e^\pm (ν_e and $\bar{\nu}_e$ separation) but also the collection of a large $\bar{\nu}_e$ CC statistics (Tab. 2) in the FHC beam mode. It can therefore precisely measure all 4 CC spectra $\nu_\mu, \bar{\nu}_\mu, \nu_e, \bar{\nu}_e$ as a function of energy.

The selection of ν_e and $\bar{\nu}_e$ CC interactions in STT benefits from the unique electron identification capability with both TR and dE/dx for background rejection. As discussed in Sec. 3.3.1, the TR capability provides a rejection factor of 10^3 against pions for momenta above 1 GeV. Electrons and positrons are separated from γ conversions from the track bending in magnetic field and hits from the pair of tracks in the straws. We further apply a kinematic rejection of non-prompt backgrounds from π^0 in ν_μ CC and NC interactions using a multivariate analysis. Fig. 81 shows the efficiency and purity of the complete ν_e CC selection in STT. Overall, we achieve a 55% (55%) efficiency and 98% (95%) purity for $\nu_e(\bar{\nu}_e)$ CC. We note that the effect of the selection is similar for ν_e and $\bar{\nu}_e$, thus reducing the systematic uncertainties in the ratios ν_e/ν_μ and $\bar{\nu}_e/\bar{\nu}_\mu$. Finally, we point out that all backgrounds can be measured in-situ from data (control samples) in STT and the efficiencies can be calibrated precisely using identified photon conversions in STT, as in NOMAD.

6.5 Low- ν Relative Flux

The low-nu method allows to estimate the (anti)neutrino flux and, at the same time, to measure the inclusive charged current cross sections. The differential charged-current scattering cross section for neutrinos can be

²There is a small phase space difference in the lepton kinematics due to the difference between the muon and electron masses (m_e vs. m_μ). However, the corresponding effect on the (integrated) total cross-section $\sigma(E)$ is negligible for the energy range relevant for DUNE.

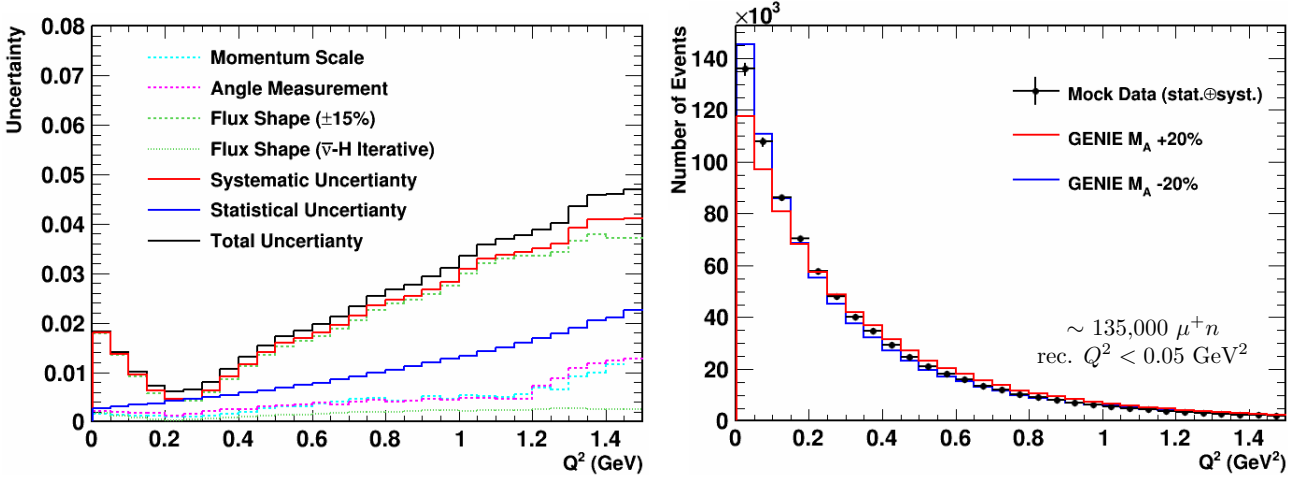


Figure 71: Left plot: expected statistical and systematic uncertainties on the reconstructed Q^2 distribution of $\bar{\nu}_\mu p \rightarrow \mu^+ n$ events on H. Two results for the flux uncertainties are shown: (a) using the initial $\pm 15\%$ uncertainty; (b) after an iterative procedure using $\bar{\nu}_\mu p \rightarrow \mu^+ n$ on H with $\nu < 0.25 \text{ GeV}$ (Fig. 70). Right plot: reconstructed Q^2 distribution of selected $\bar{\nu}_\mu p \rightarrow \mu^+ n$ on H for the complete sample without ν cut. The solid circles (mock-data) correspond to the nominal GENIE cross section and include both statistical and systematic uncertainties added in quadrature (left plot). The sensitivity to a modification of the axial form factor by $M_A \pm 20\%$ is shown for illustration purpose. All distributions are normalized to the same integral.

expressed in terms of neutrino energy (E_ν), energy transferred to nucleus (recoil energy or ν), and Bjorken scaling variable (x) as:

$$\frac{d\sigma}{d\nu} = \frac{G_F^2 M}{\pi} \int_0^1 \left(F_2 - \frac{\nu}{E_\nu} [F_2 \mp x F_3] + \frac{\nu}{2E_\nu^2} \left[\frac{Mx(1-R_L)}{1+R_L} F_2 \right] + \frac{\nu^2}{2E_\nu^2} \left[\frac{F_2}{1+R_L} \mp x F_3 \right] \right) dx, \quad (5)$$

where G_F is the Fermi constant, M is the proton mass, F_2 and F_3 are structure functions, R_L is the structure function ratio $F_2/(2xF_1)$, and the “+” is for ν_μ and the “-” is for $\bar{\nu}_\mu$. If one limits the final-state phase space to events with ν less than a cutoff value ν_0 (where $\nu_0 \ll E_\nu$) the terms proportional to ν/E_ν , ν/E_ν^2 , and ν^2/E_ν^2 are small, yielding a cross section that is approximately constant as a function of neutrino energy. Under these conditions, we can then determine the shape of the neutrino flux as a function of E_ν . The low- ν method was proposed by Mishra [60], pioneered by the CCFR collaboration [70], and used by the NuTeV [76], MINOS [5] collaborations. While the formulation in Eq. 5 is only strictly true in the DIS regime, the low- ν method is still applicable at lower momentum, as demonstrated by the MINERVA collaboration [36].

As an example we consider muon neutrinos interacting in CC inside the detector inner tracker. For the DUNE spectrum and $\nu < 0.25(0.5)$ GeV the visible energy is completely dominated by the muon and, therefore, the single most critical parameter to achieve a good accuracy is the uncertainty on the muon energy scale. In this respect two requirements are crucial: (a) a low density tracking detector; (b) a precise calibration of the measured momenta for the charged particles. The density of the STT $\rho \sim 0.16 \text{ g/cm}^3$ and its trac sampling are well suited for these measurements. Following the technique used by the NOMAD experiment – based upon a similar detector concept – we can calibrate the momentum scale of charged particles with the mass peak of the large samples of reconstructed K_0 decays and achieve similar muon energy scale uncertainties of 0.2%. Figure 82 illustrates the effect of this uncertainty on the measured flux. The typical uncertainties on the muon energy scale expected for the other ND components are about 2% for the LAr and scintillator tracker and 1% for the HPgTPC, values which are significantly worse than the 0.2% achievable in STT.

The CH₂ material also offers other advantages over Ar as target for the low- ν analysis. A significant source of uncertainty is related to the smearing of the reconstructed hadronic energy ν , which not only affects the total visible energy but, more importantly, the acceptance of the ν_0 cut used in the analysis. Neutron production in neutrino interactions play here an important role, in addition to the detector resolution of individual charged particles, since neutrons are typically associated to some undetected energy. Figure 83 shows that the fraction of hadronic energy carried by neutrons at small values of ν is about a factor of 2 smaller in CH₂ than in Ar. Similar results apply to the average number of neutrons produced. It must be noted that this result is confirmed by using different event generators, although large uncertainties are present on the neutron production (Fig. 83). We can therefore conclude that Ar is not a good target for the low- ν analysis, as it results in substantially higher uncertainties from the nuclear smearing.

The GENIE low- ν muon neutrino cross sections for the CH₂ and H targets and for different values of ν_0 are shown in Fig. 84. The cross section in low- ν regime deviates from a constant especially for $E_\nu = 1$ GeV. This is mainly due to the energy dependency in the quasi-elastic (QE) scattering with carbon nuclei

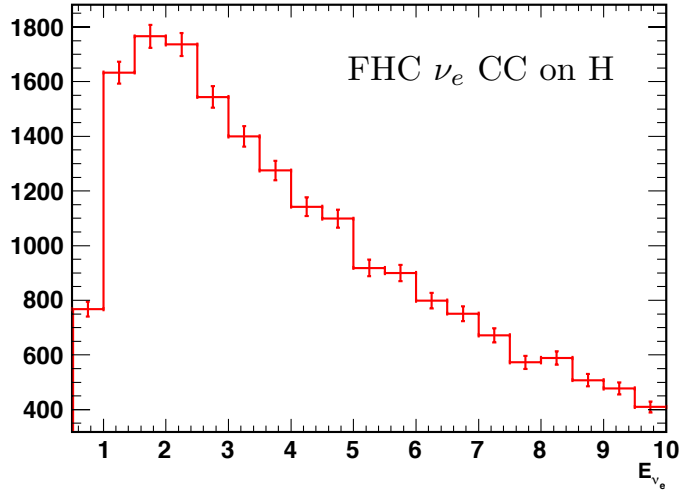


Figure 72: Reconstructed energy distribution for the ν_e CC interactions on H identified in STT with the FHC neutrino beam.

Table 13: CC muon neutrino interaction events simulated inside the detector inner tracker for different ν_0 cuts and with energy greater than the minimum energy set for each value of ν_0 .

CH ₂			
ν_0 (GeV)	E_{min} (GeV)	$N_{int}^\nu / 5.5 \cdot 10^{21}$ POT	N_{int}^ν / N_{int}
0.250	0.625	$2.75 \cdot 10^6$	0.10
0.375	0.875	$3.97 \cdot 10^6$	0.14
0.500	1.125	$5.43 \cdot 10^6$	0.19
0.625	1.500	$6.23 \cdot 10^6$	0.22
0.750	1.875	$6.38 \cdot 10^6$	0.23
H			
ν_0 (GeV)	E_{min} (GeV)	$N_{int}^\nu / 5.5 \cdot 10^{21}$ POT	N_{int}^ν / N_{int}
0.250	0.375	$2.83 \cdot 10^3$	0.00
0.375	0.500	$9.94 \cdot 10^4$	0.05
0.500	0.875	$3.10 \cdot 10^5$	0.14
0.625	1.250	$4.67 \cdot 10^5$	0.21
0.750	1.625	$5.45 \cdot 10^5$	0.25

(see Fig. 85) and a correction for this effect is then required and applied as discussed later. The possibility to select neutrino interactions on H represents therefore an important opportunity to measure the relative neutrino with the low- ν method. The GENIE low- ν muon anti-neutrino cross sections for the CH₂ and H targets are shown in Fig. 86 and 87.

Particular attention must be paid in choosing the value of the ν_0 cut. Selecting a larger value of ν_0 will select more data and yield smaller statistical uncertainties in the flux. While selecting a smaller ν_0 will reduce the energy dependence of the low- ν cross section, and hence the flux-model dependence. For these reasons, the procedure is usually repeated in parallel for different values of ν_0 . Besides, for a given value of ν_0 , a minimum neutrino energy has to be set in order to reach the low- ν regime. In this paper, the minimum neutrino energy is set to keep the fraction of simulated events that pass the low- ν cut in each bin less than 50% [36]. Fig. 88 shows, for instance, the fraction of muon neutrino events surviving different values of the ν_0 cut and the corresponding minimum neutrino energies.

A number of CC muon neutrino events induced in 5 years ($5.5 \cdot 10^{21}$ POT) by the 120 GeV primary proton beam flux in FHC mode, has been generated with GENIE (sec. 4.2.1). The same exposure for muon anti-neutrinos in RHC mode has been also simulated. The total number of generated events surviving the selection criteria are reported in Tab. 13 and 14. To take into account the detector response and test the low- ν method, we simulated an acceptance of 80% and a energy resolution of 5% for both E_ν and ν on the generated events, here used as “data”.

Under the low- ν conditions, the neutrino flux in an energy bin of width ΔE is [36]:

$$\Phi \propto \frac{U_\nu(D_\nu - B_\nu)}{C_\nu \times \Delta E}, \quad (6)$$

where D_ν is the reconstructed inclusive interaction yield, B_ν is the background yield predicted by the

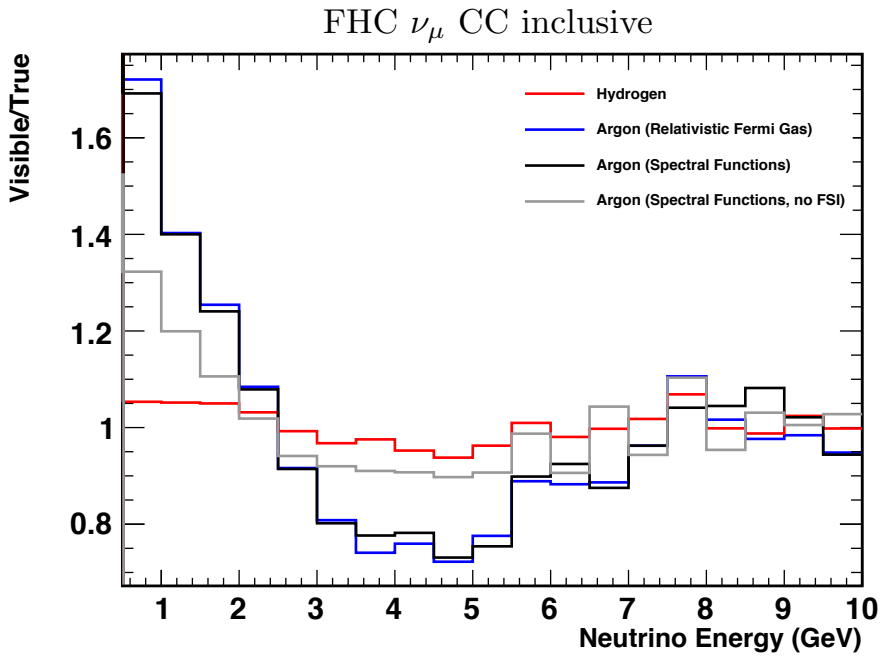


Figure 73: Ratio of reconstructed to true neutrino energy in inclusive ν_μ CC interactions from the Ar and H targets in STT. The large effects of the nuclear smearing in Ar observed in the main oscillation region can be constrained with H events in STT.

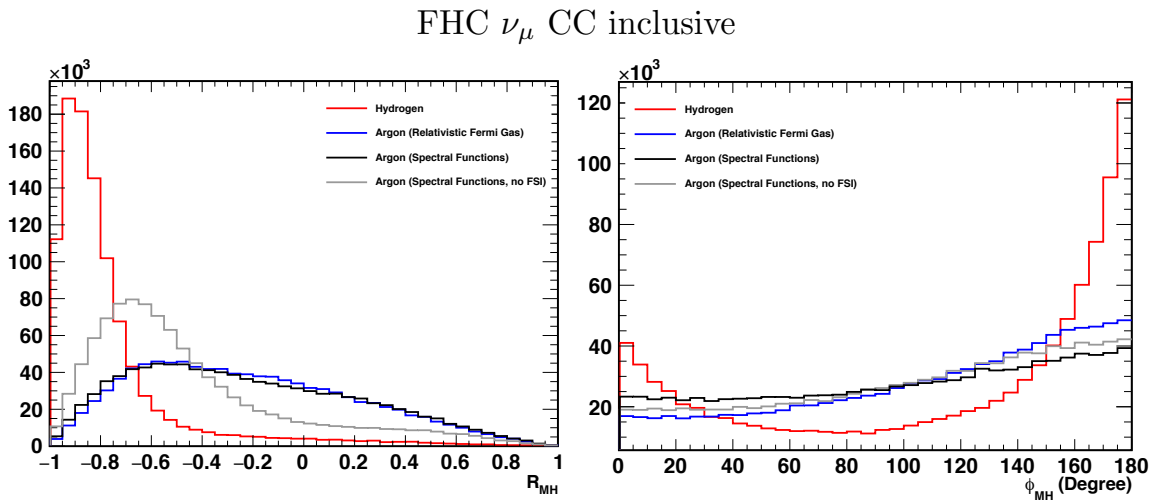


Figure 74: Left panel: comparison of the reconstructed p_T asymmetry R_{MH} from inclusive ν_μ CC interactions in Ar and H obtained with different assumptions for the input nuclear model. Right panel: same as the previous panel but for the angle Φ_{MH} between the missing p_T and the p_T of the hadron vector.

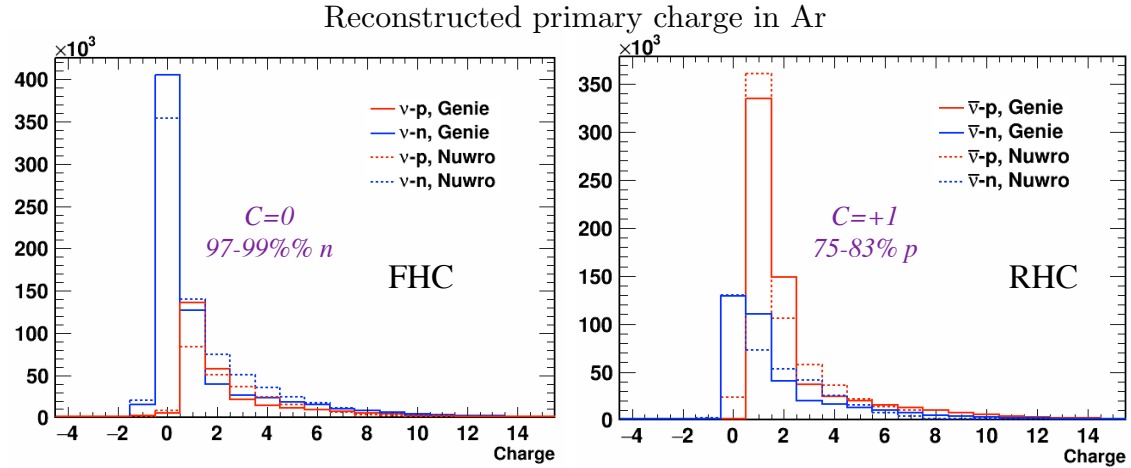


Figure 75: Left panel: Reconstructed charged at the primary vertex $C_{\text{vtx}} = 0$ in FHC inclusive ν_μ CC interactions from the Ar target in STT. The requirement $C_{\text{vtx}} = 0$ selects a high purity sample of interactions on neutron. Right panel: same as the previous panel but for RHC inclusive $\bar{\nu}_\mu$ CC interactions. The requirement $C_{\text{vtx}} = 0$ selects a sample of interactions on proton.

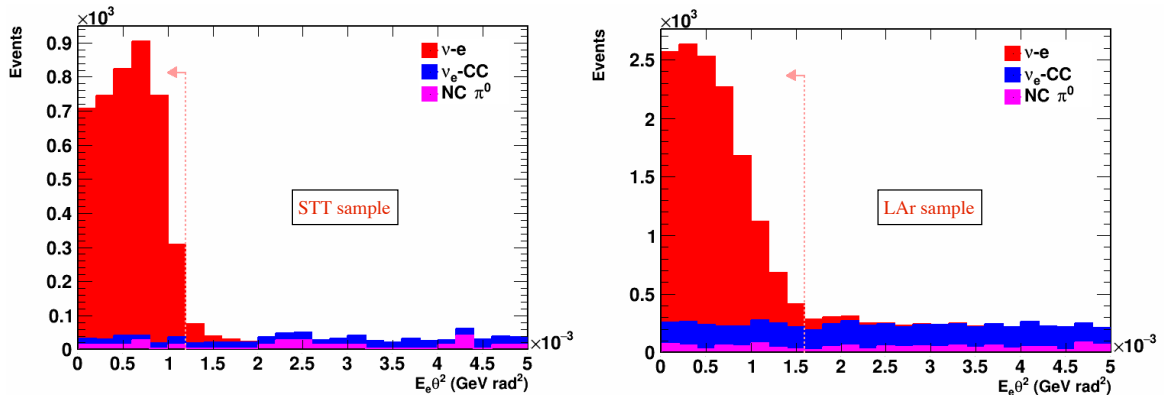


Figure 76: Signal and background selection of ν -e elastic scattering in STT (left panel) and LAr (right panel).

simulation and U_ν is an unfolding operator removing the effects of the energy resolutions and detection efficiency.

The small E_ν dependence of the low- ν cross section introduces a shape-dependence to the yield of flux sample events apart from the flux, these variations are corrected dividing the measured flux by the factor C_ν , extracted from a second Monte Carlo sample. A number of $5 \cdot 10^9$ probing muon neutrinos with a flat energy spectrum was simulated between 10 MeV and 15 GeV. The correction factor was then calculated as:

$$C_\nu = \frac{\sigma(\nu < \nu_0, E_\nu)}{\sigma(\nu < \nu_0, E_\nu \sim 10 \text{ GeV})}. \quad (7)$$

The flat energy spectrum generated events were then reweighted to the beam neutrino flux (see Fig.89) and used to calculate the detector response in the unfolding procedure. The energy spectra were then unfolded with an iterative method based on Bayes' theorem [33], assuming a null background (see Fig.90). The critical change of the energy spectrum at high energies ($E_\nu \approx 4$ GeV) causes some problems in the present unfolding procedure. For this reason, different unfolding algorithms are still under testing to avoid bias. The present results of the relative neutrino fluxes for selected values of the low- ν cut ν_0 are shown in Fig.91 and Fig.92 and compared with the simulated incident neutrino spectra.

7 Coupling with external LAr detector

Based on scientific considerations, the DUNE Near Detector Concept Study recommended (R7) a new-build dipole magnet for the multi-purpose spectrometer downstream of the DUNE near-detector complex [59]. The main purpose of the magnet is to host a tracking system in a magnetized volume in order to measure charge and momentum of the muons produced in ν_μ -Ar CC interactions in the ArgonCube fiducial volume. For this reason, muon acceptance of the KLOE + ArgonCube system was detailed studied and optimized.

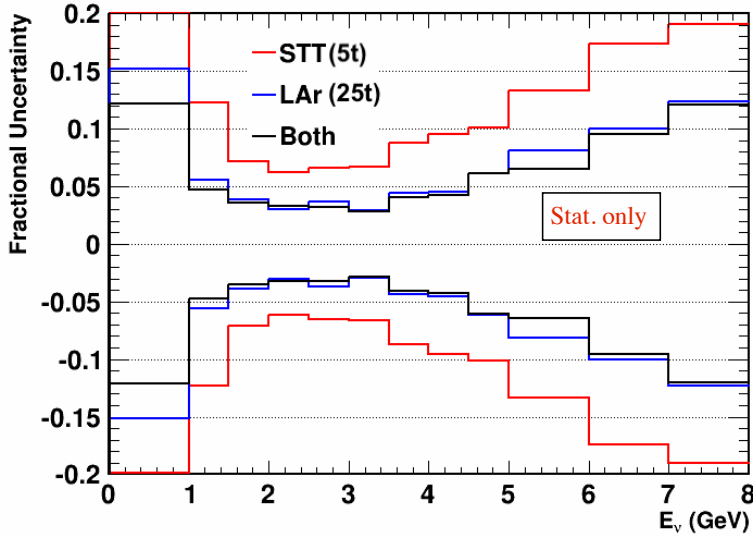


Figure 77: Uncertainties on the relative ν_μ flux as a function of energy extracted from template fits to the reconstructed (E_e, θ_e) distributions in ν -e elastic scattering events measured in STT, LAr and LAr+STT.

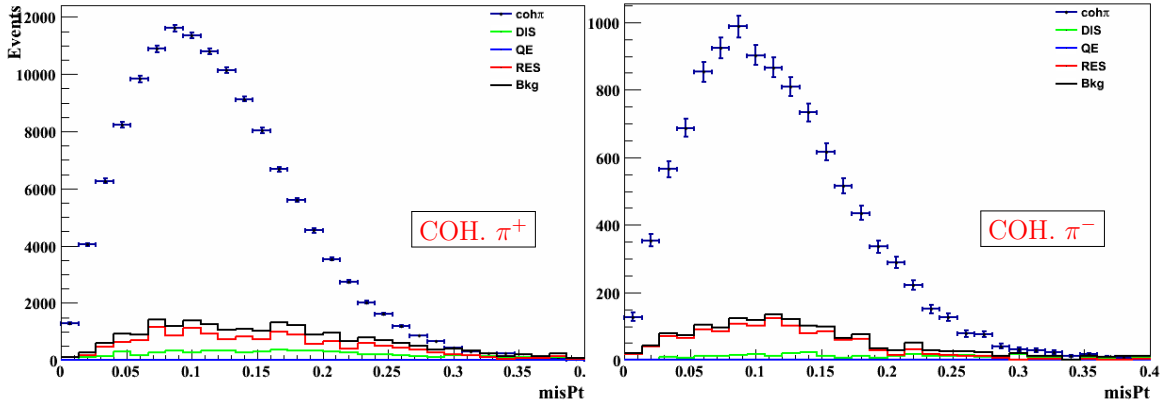


Figure 78: Reconstructed missing transverse momentum for coherent π^+ (left panel) and π^- (right panel) selected in STT with the standard FHC neutrino beam polarity. The histograms show the actual statistics expected, as well as the contributions from the various background sources.

About 18k muon neutrino CC interactions have been generated in ArgonCube fiducial volume. The location of the stopping point of the produced muons or whether they reach STT have been studied and the fraction are reported in table 7. The figure 93 shows the MC true kinetic energy distribution of the muons grouped according to the location of their stopping points.

Stopping point location	percentage
ArgonCube Volume	21%
ACRC	47%
Yoke	5%
Cryostat or Coil	0.7%
Calorimeter	1.2%
STT	10%

The missing fraction, about 15%, is due to muons exiting from the lateral walls of ArgonCube and not stopping in ACRC or exiting from the downstream wall of ArgonCube and not intercepting KLOE magnet. It is worth noting that this fraction of events is not recoverable with any reasonable detector downstream ArgonCube. The energy of stopping muons has been evaluated by means of its observed range while for that reaching STT volume their energy is reconstructed exploiting the measured bending in the magnetic volume. The resulting correlation between muon reconstructed and true kinetic energy is shown in figure 94, while figure 95 shows the muon kinetic energy resolution.

As can be seen from figure 96, showing a comparison between the muon reconstructed and true kinetic energy, the muon kinetic energy range interested by neutrino oscillation phenomena (< 2 GeV) is fully covered by the system. This can be better evaluated from figure 97, where the green crosses represent

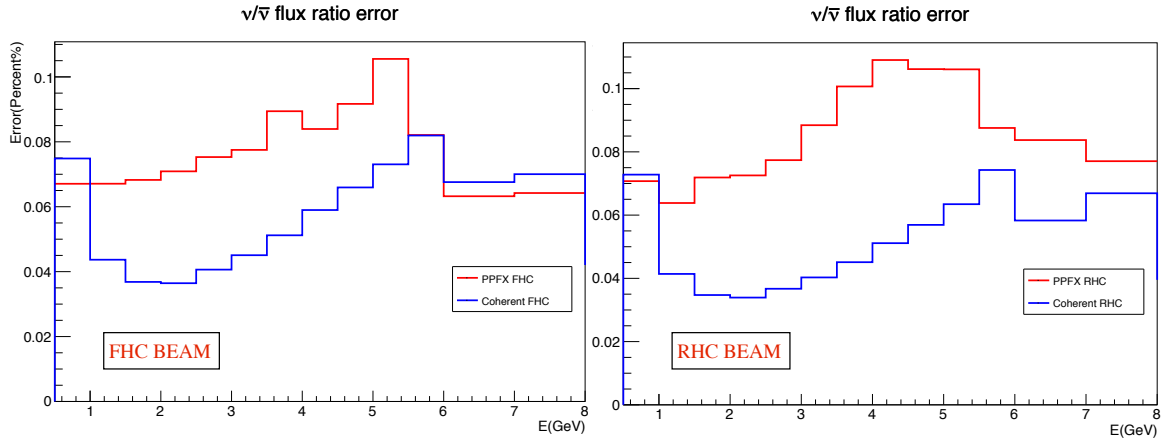


Figure 79: Uncertainty on the $\bar{\nu}_\mu/\nu_\mu$ flux ratio determined in STT from the ratio of coherent pion production in both the neutrino FHC (left panel) and antineutrino RHC (right panel) beam polarities. The corresponding uncertainties obtained from the beam simulation group are also shown for comparison.

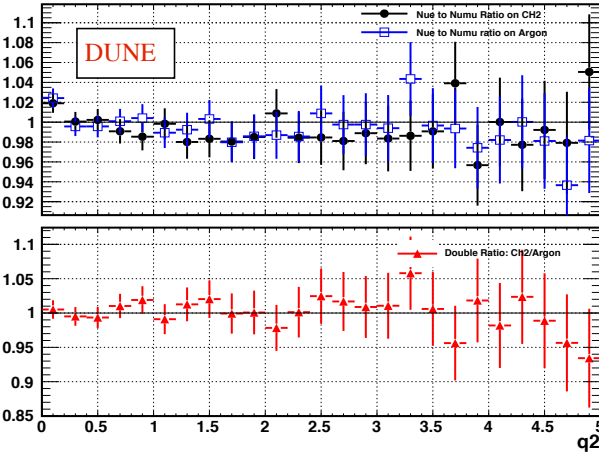


Figure 80: Left panel: comparison of the ν_e/ν_μ CC ratio in polypropylene ($C_3H_6)_n$ and Ar targets (top plot) and the corresponding double ratio (bottom plot). Right panel: measurement of e^-/μ^- universality from ν_e/ν_μ CC interactions in NOMAD.

the MC true acceptance of system defined as the fraction of muons for which the kinetic energy can be reconstructed as function of MC true kinetic energy. The blue curve represents the same quantity as function of the reconstructed kinetic energy. The blue curve and green crosses are very similar and a nearly 100% acceptance is obtained for a muon kinetic energy less than 2 GeV.

8 Backgrounds

The background at the ND site for neutrino-beam events is essentially due to the following sources:

- cosmic radiation (mainly muons and neutrons, also atmospheric neutrinos)
- natural radioactivity emitted by the surrounding rock and detector material (mainly photons and neutrons)
- beam-neutrino interactions in the material all around the detector (rock and infrastructures)

The first two background sources can be drastically suppressed by requiring coincidence with the beam spill. The third one is more critical because of the small detector mass with respect to the external mechanical structure.

Cosmic radiation - The center of the DUNE-ND shall be located under a layer of soil (~ 23 m) and one of rock (~ 34 m) [57]. Assuming a soil density of 2.24 g/cm^3 and a rock density of 2.67 g/cm^3 [78] the layer above the ND-hall has a grammage of $\sim 14200 \text{ g/cm}^2$. Simulations performed with FLUKA for a hypothetical giant detector underground [34] predict a reduction of the cosmic muon rate by more than a

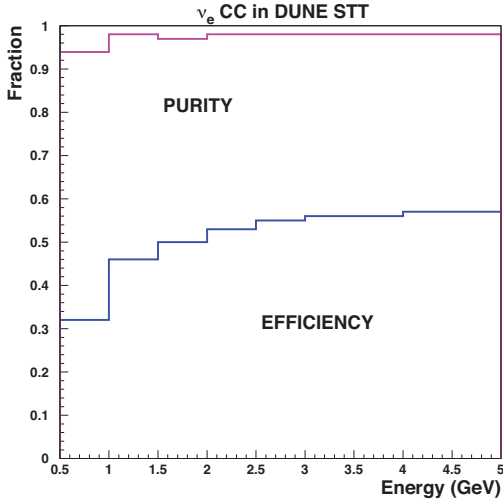


Figure 81: Efficiency and purity as a function of energy for the ν_e CC selection in STT.

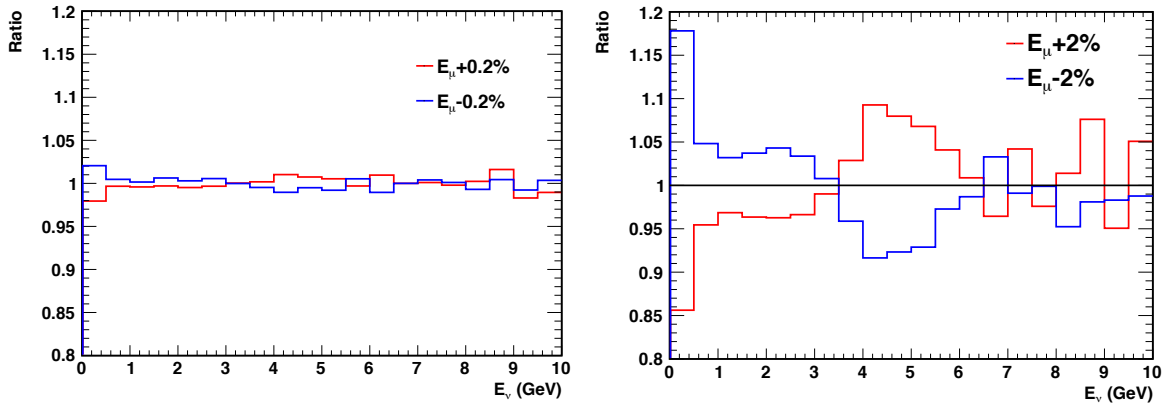


Figure 82: Comparison of the effect of the muon energy scale uncertainty on the relative flux extracted with the low- ν method. Typical values for STT (left panel) and LAr/scintillator (right panel) are shown.

factor 100 with respect to surface. Assuming a surface flux of $0.02 \mu\text{cm}^2/\text{s}$ and a total surface (including the yoke) of $2 \times 10^6 \text{ cm}^2$ one obtains 0.004 muons/spill entering the KLOE outer structure, which can be considered negligible.

Natural radioactivity - Contamination by radioactive isotopes in the cavern and detector materials produces photon background and neutron background, this last from (α, n) reactions. Ambient neutron background has been measured and calculated, for instance, for the Gran Sasso experimental halls. The order of magnitude of the neutron flux is $3 \times 10^{-6} \text{ n/cm}^2/\text{s}$, with an energy spectrum limited to $10 - 20 \text{ MeV}$ [81]. Background from the detector materials depends on specific contamination, it can be assumed in first approximation to be at the same level as ambient background. Again, by asking for in-spill events, this background can be treated as negligible.

External neutrino interactions - This background cannot be removed looking at the spill time. Therefore it has been studied generating with Fluka a sample of $19 \times 10^3 \nu_\mu$ -CC interactions in the material surrounding the STT detector (yoke, cryostat, coils and calorimeter). Taking into account that the simulated external mass is ~ 770 tons and the mass of the detector is ~ 3.68 tons, a rejection capability higher than 10^3 is required in order to reach an acceptable signal-over-noise ratio.

The algorithm presented in Sec. 5.2 has been used to reconstruct the neutrino interaction vertices and further to accept only events with the reconstructed vertex inside a fiducial volume (at 30 cm from the calorimeter internal walls). All the events surviving after this first cut have the true vertex in the calorimeter. Moreover, the events with a calorimeter signal upstream with respect to the reconstructed vertex are also rejected. Then, the external interactions are recognised by exploiting the time-resolution of the calorimeter ($\sim 0.25 \text{ ns}$) [7] and that of the STT ($\sim 1.5 \text{ ns}$) [66]. At the end it is required that the sum of the momenta of the charged tracks in each event be within 0.5 rad from the beam axis (Fig. 98).

Applying all these cuts the survival probability for external interactions is 6×10^{-4} . The same anal-

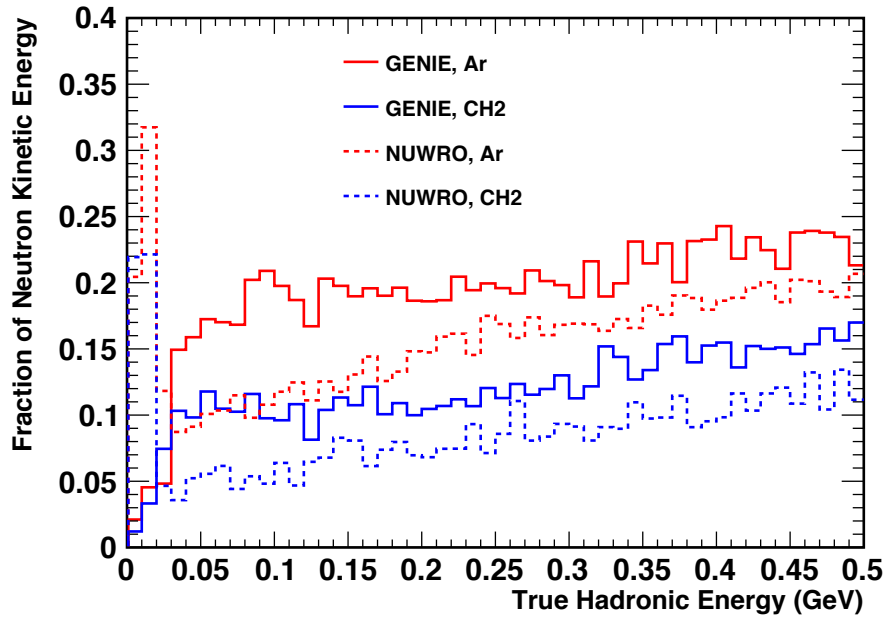


Figure 83: Effect of the nuclear target material on the measurement of the hadronic energy ν . The curves show the fractions of energy associated with neutrons in CH_2 plastic and Ar according to two different event generators: GENIE (solid lines) and NuWro (dashed lines).

ysis chain has been applied to a sample of 10×10^3 ν_μ -CC interactions inside the STT volume (internal interactions). In this case the survival probability results 48×10^{-2} .

On the basis of this first analysis the signal-over-noise ratio results 3.8. We are confident that a refinement of the reconstruction and selection algorithms will allow to improve greatly this preliminary result.

9 Technical feasibility

9.1 Disassembling KLOE

Due to the constraints posed by the available assembly hall and its related crane system, KLOE design has been optimized in term of modularity and ease of assembly. The iron yoke is built in pieces of less than 30 t, which can be precisely coupled by milling the mating surfaces and by appropriate doweling. The dimensions of any single piece are compatible with a high load transport, avoiding the need of expensive and time consuming special road transports. The solenoid, which has a weight of 43 t, is the only piece requiring a special road transport, due to its dimensions.

Dismantling of KLOE can be executed efficiently by the availability of the complete set of “as built” drawings, the compete operational manuals, of the most part of the custom mounting rigs, as well as of the

Table 14: CC muon anti-neutrino interaction events simulated inside the detector inner tracker for different ν_0 cuts and with energy greater than the minimum energy set for each value of ν_0 .

CH ₂			
ν_0 (GeV)	E_{min} (GeV)	$N_{int}^\nu / 5.5 \cdot 10^{21}$ POT	N_{int}^ν / N_{int}
0.250	1.125	$2.28 \cdot 10^6$	0.22
0.375	1.500	$2.75 \cdot 10^6$	0.26
0.500	2.125	$2.69 \cdot 10^6$	0.25
0.625	2.750	$2.03 \cdot 10^6$	0.19
0.750	3.375	$1.19 \cdot 10^6$	0.11
H			
ν_0 (GeV)	E_{min} (GeV)	$N_{int}^\nu / 5.5 \cdot 10^{21}$ POT	N_{int}^ν / N_{int}
0.250	1.750	$5.29 \cdot 10^5$	0.27
0.375	2.250	$4.86 \cdot 10^5$	0.25
0.500	2.875	$3.35 \cdot 10^5$	0.17
0.625	3.375	$2.12 \cdot 10^5$	0.11
0.750	3.875	$1.20 \cdot 10^5$	0.06

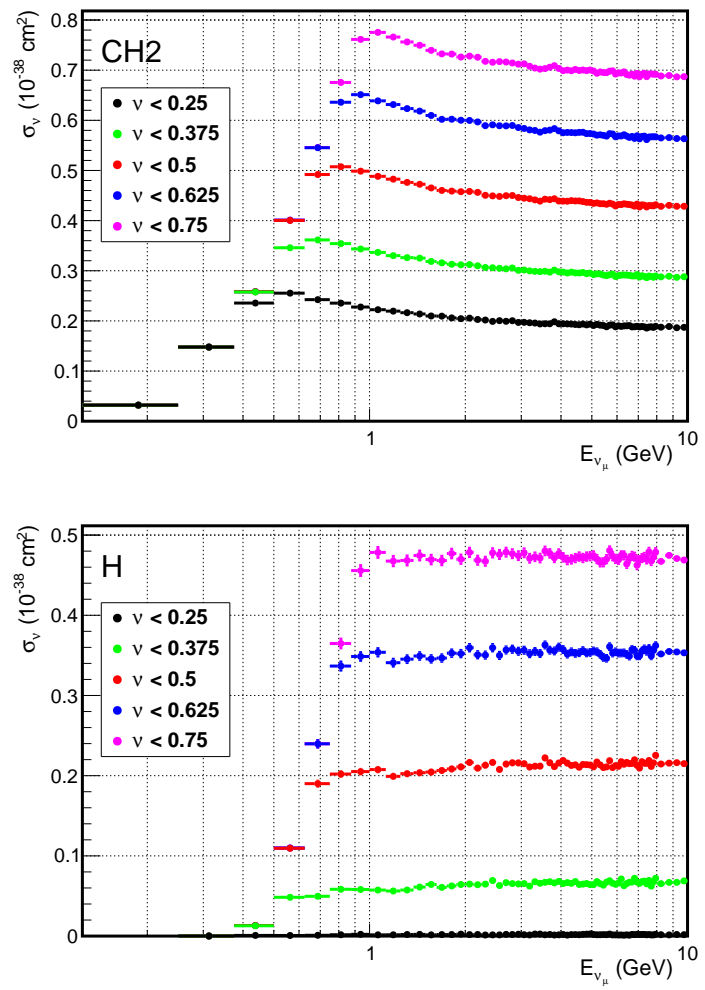


Figure 84: Muon neutrino partial charged cross sections per nucleon for low- ν events determined from GENIE for different values of the ν_0 cut.

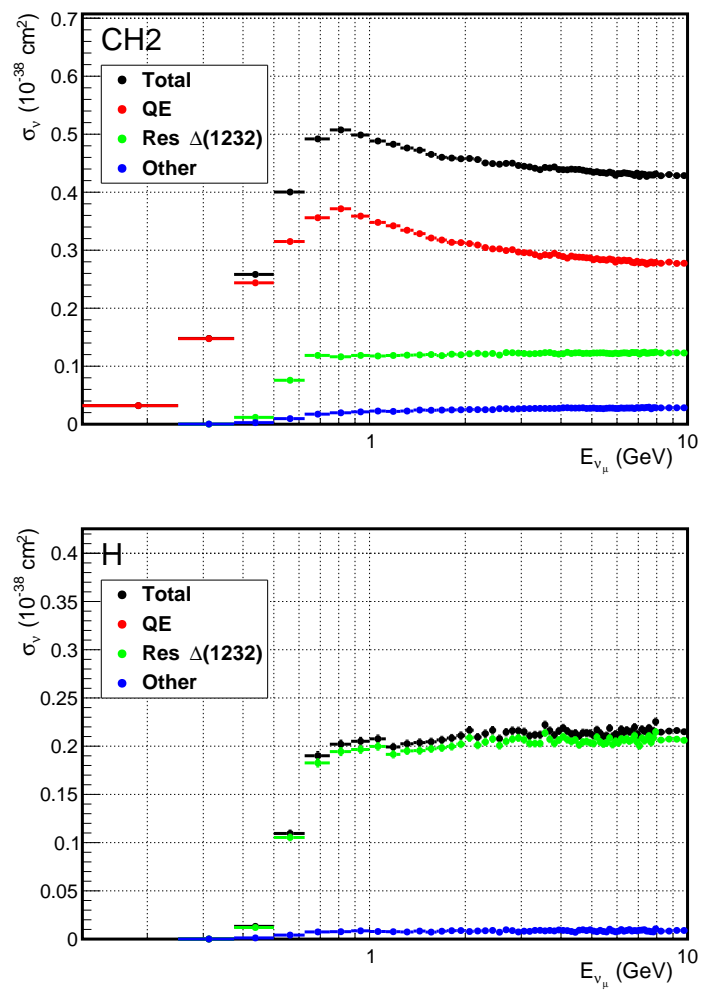


Figure 85: The $\nu < 0.5$ GeV partial charged current cross sections per nucleon from GENIE. Shown are the QE, the $\Delta(1232)$ resonance and the other contributions.

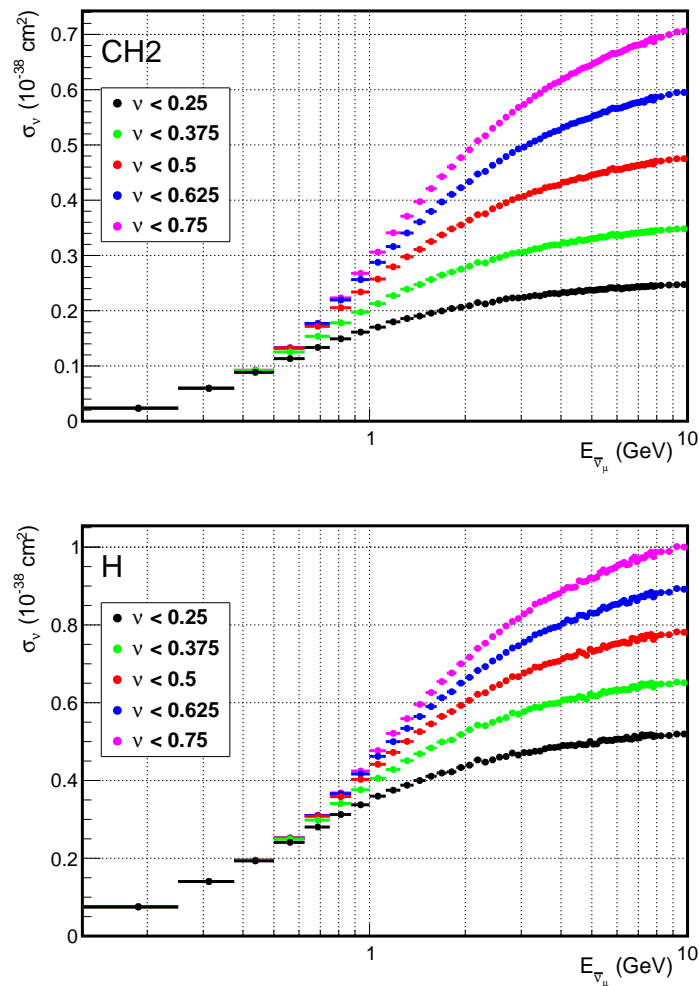


Figure 86: Muon neutrino partial charged cross sections per nucleon for low- ν events determined from GENIE for different values of the ν_0 cut.

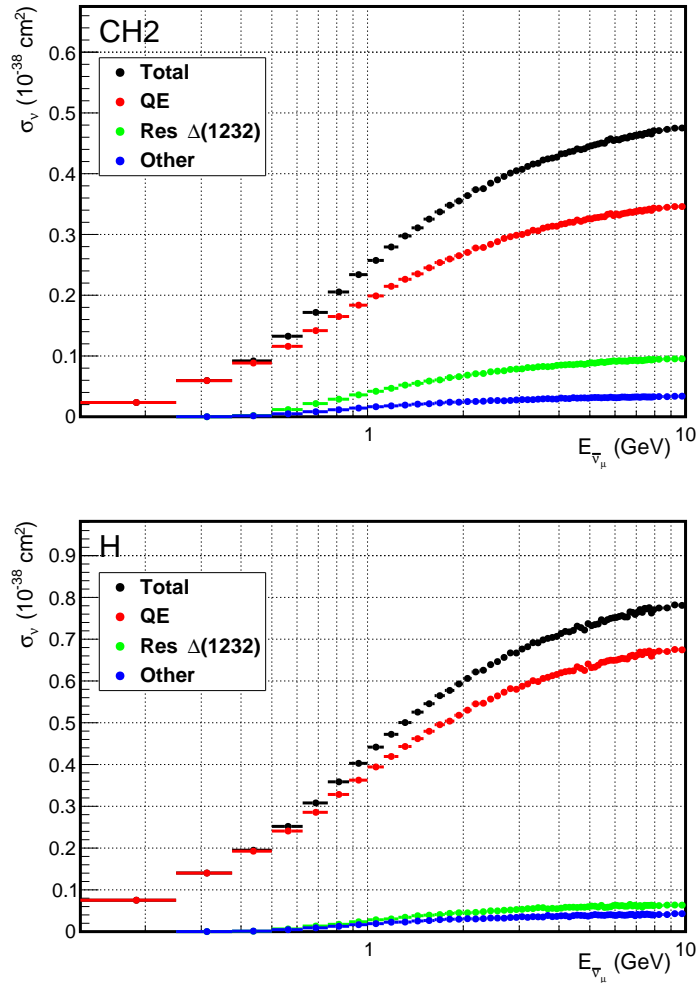


Figure 87: The $\nu < 0.5$ GeV partial charged current cross sections per nucleon from GENIE. Shown are the QE, the $\Delta(1232)$ resonance and the other contributions.

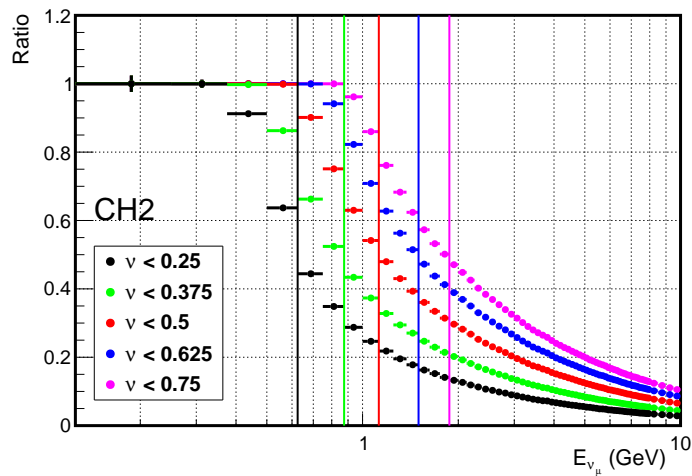


Figure 88: Fraction of low- ν muon neutrino events in the GENIE Monte Carlo simulation and interacting with the CH₂ target, for different values of ν_0 cut in GeV. The vertical lines indicate the corresponding minimum neutrino energy keeping the fraction of simulated events that pass the low- ν cut in each bin less than 50%.

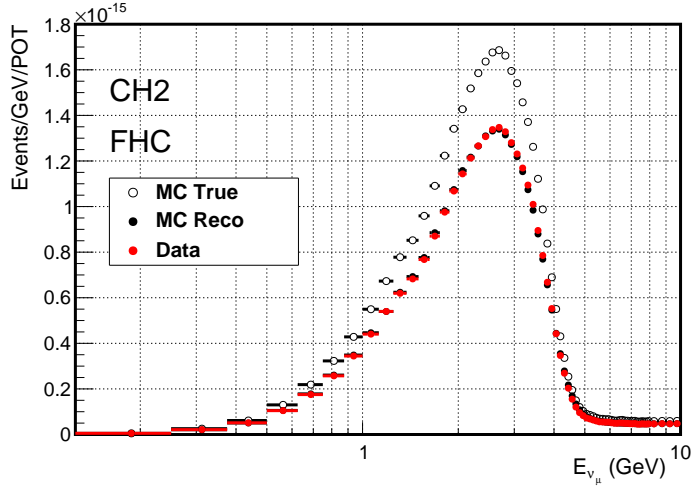


Figure 89: Event spectra at the generation level and after the detector response simulation. The detector response was simulated assuming an acceptance of 80% and a energy resolution of 5% to generate both MC and data samples at the reconstruction level.

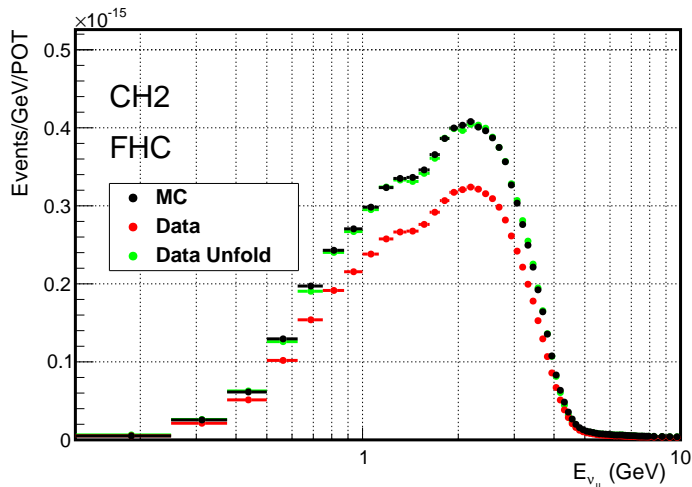


Figure 90: Energy spectra of the simulated data sample at the reconstruction level and after the unfolding procedure for $\nu_0 = 0.5$ GeV. For comparison the simulated sample used as MC truth at the generation level and under the same low- ν condition is also plotted.

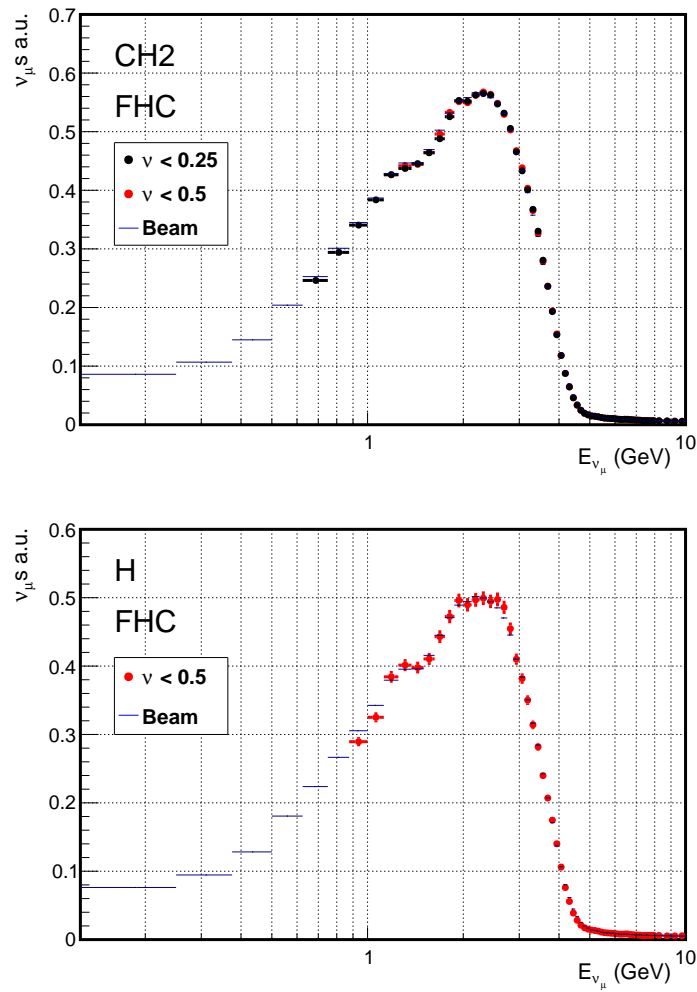


Figure 91: Muon neutrino flux in arbitrary units as evaluated using Eq.6 after the iterative unfolding procedure. For comparison the simulated flux is also plotted.

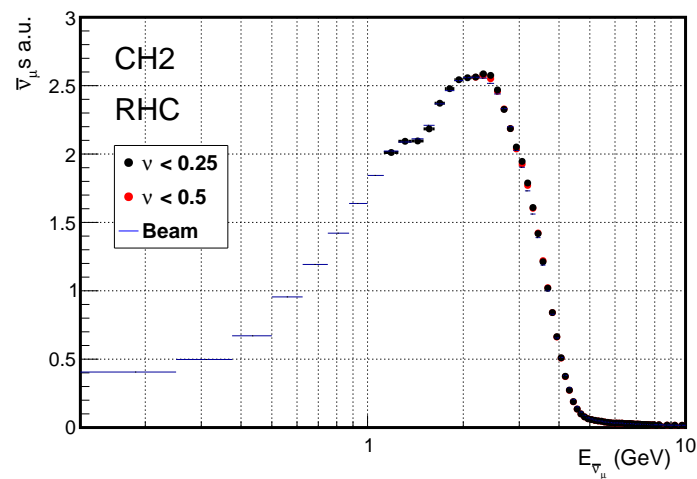


Figure 92: Muon antineutrino flux in arbitrary units as evaluated using Eq.6 after the iterative unfolding procedure. For comparison the simulated flux is also plotted.

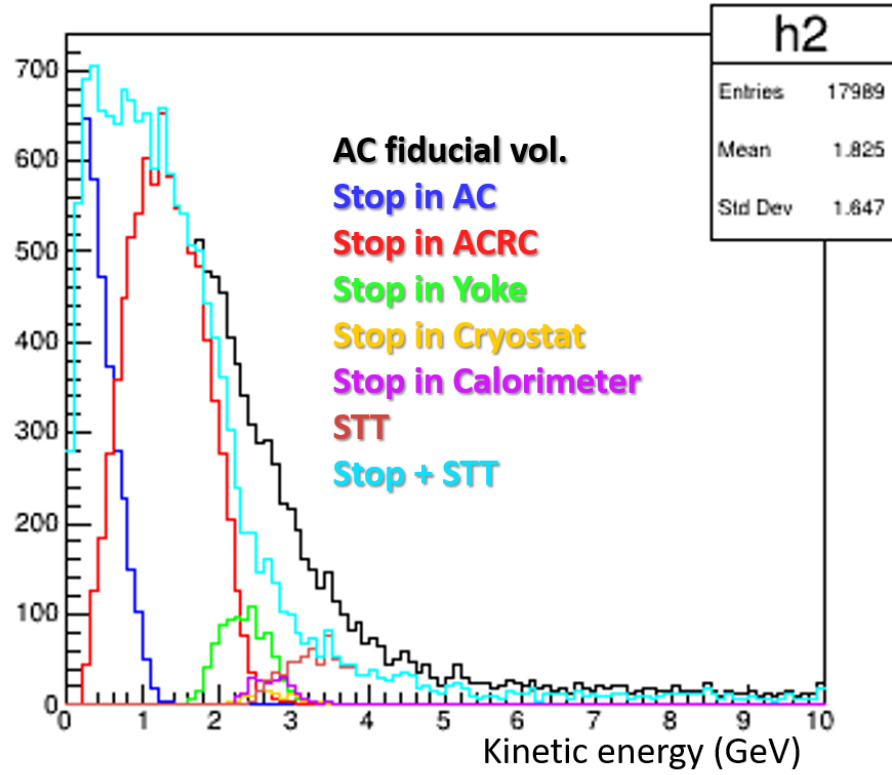


Figure 93: MC true Kinetic energy distribution of muons produced in ν_μ CC interactions with LAr in ArgonCube fiducial volume. Blue, red, green, yellow and violet lines represent muons stopping in ArgonCube, ACRC, Yoke, Cryostat and calorimeter respectively. Brown line represent muons with STT hits, while cyan line represent stopping muons and with STT hits.

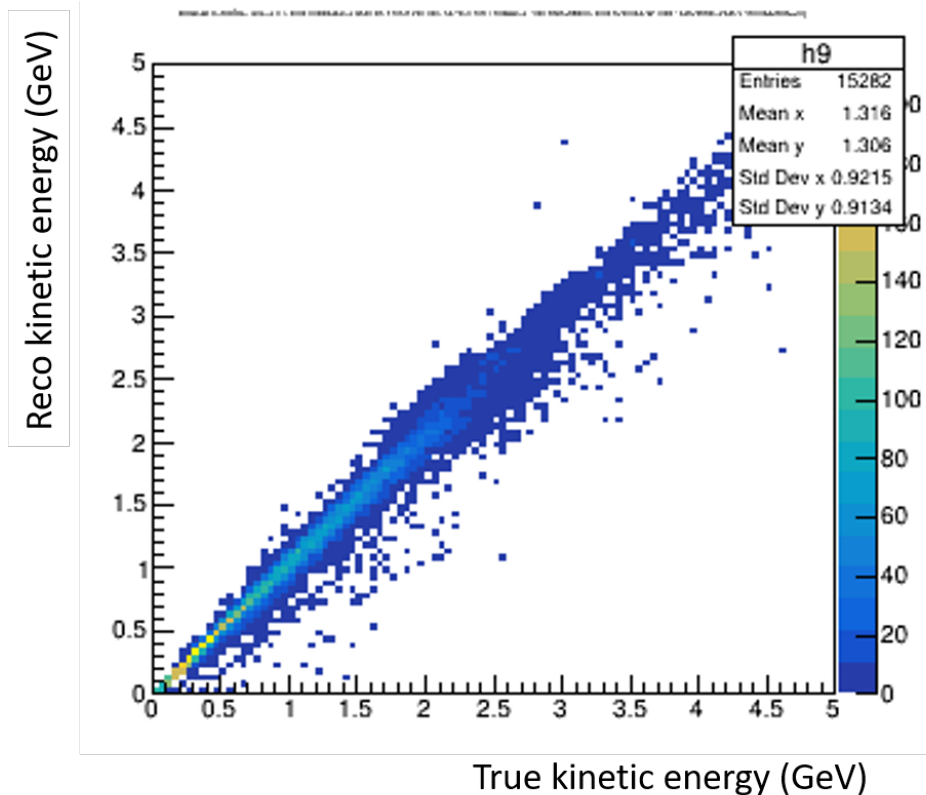


Figure 94: Correlation between muon reconstructed and true kinetic energy.

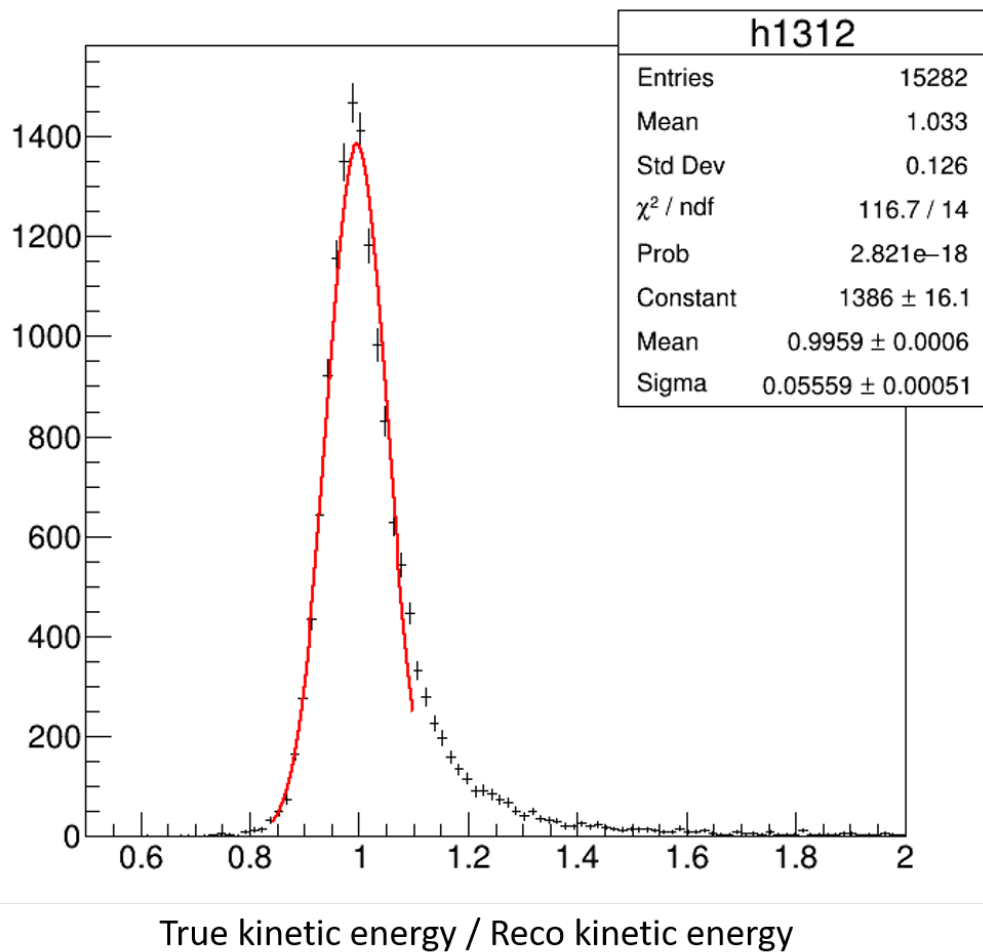


Figure 95: Overall muon kinetic energy resolution.

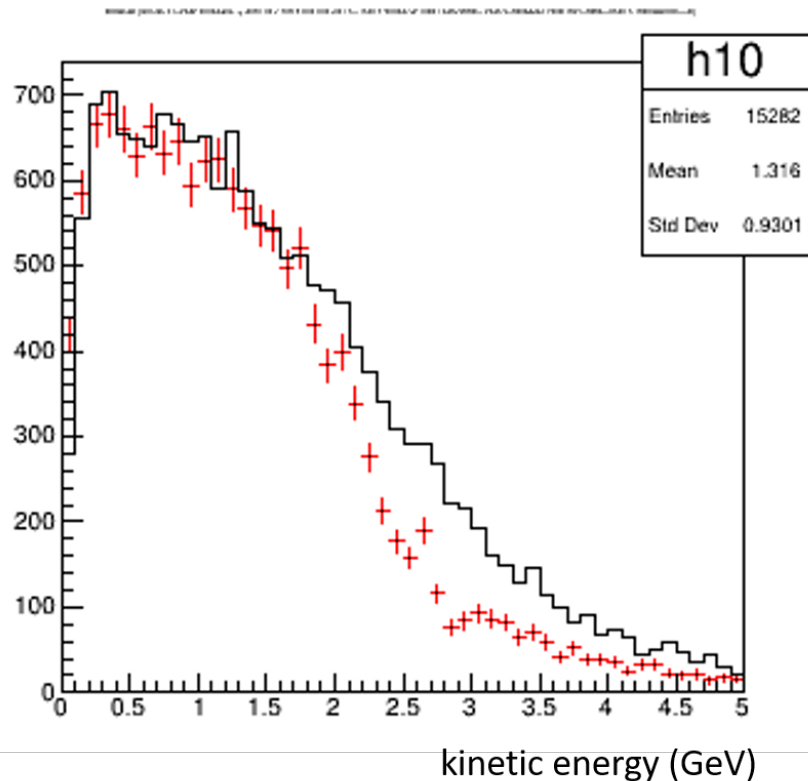


Figure 96: Comparison between the muon reconstructed and true kinetic energy.

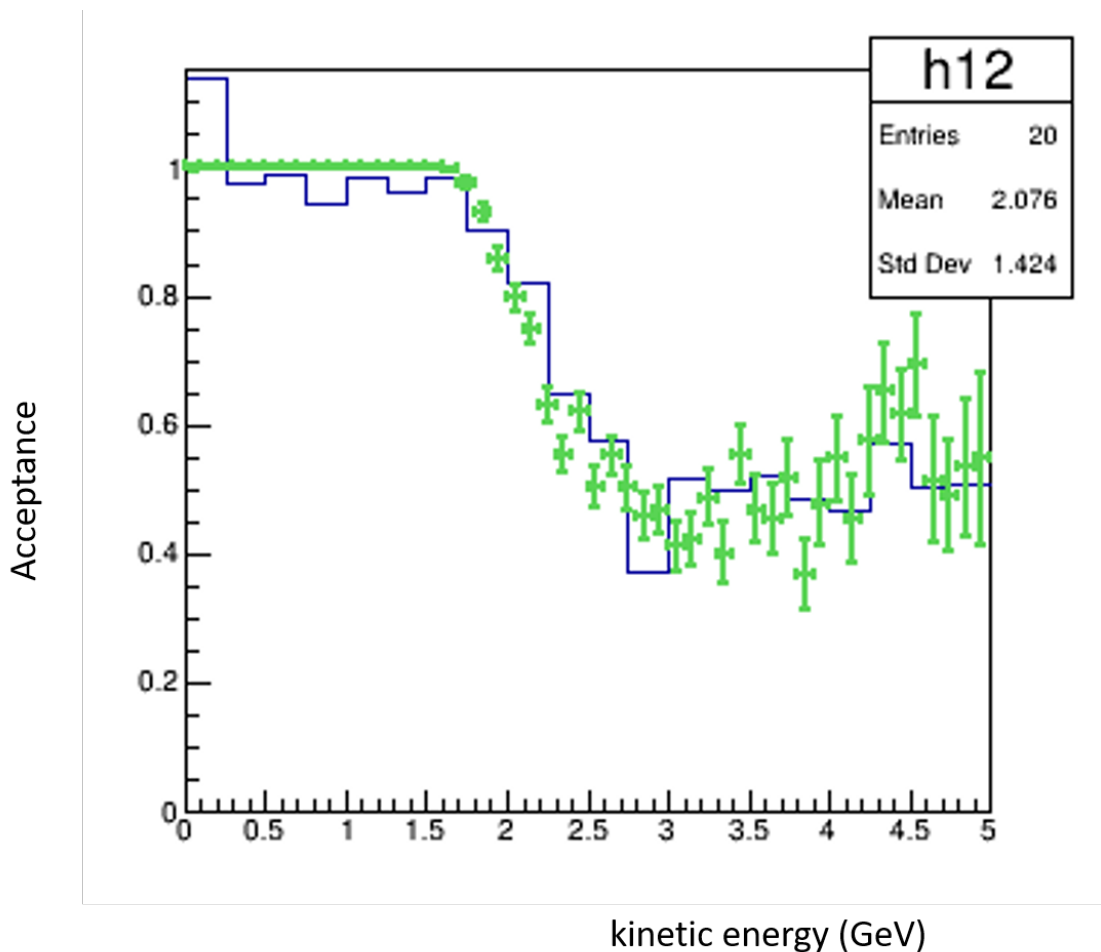


Figure 97

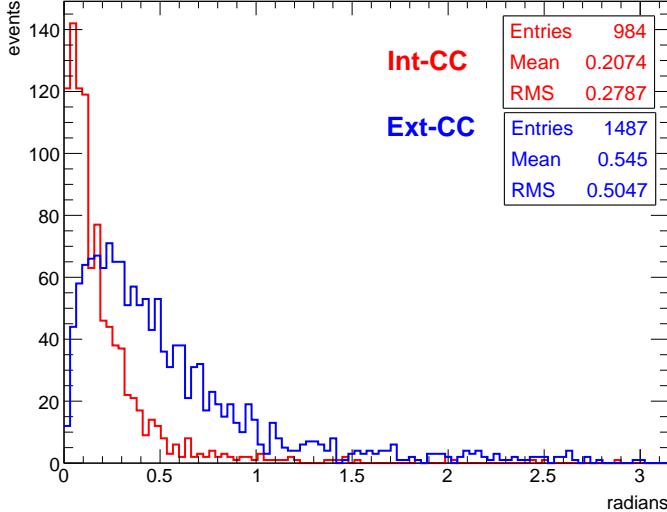


Figure 98: Distribution of the angle of the total momentum of charged tracks with respect to the beam-axis for internal and external interactions after topological and time-cuts. Looking at this distribution another cut has been applied (angle lower than 0.5 rad) in order to select internal interactions.

collaboration of some of the key personnel of the construction phase.

The EM calorimeter will be separated in 24 barrel modules and 4 endcap half-sectors. Ancillary components (magnet cryo-systems, controls and power supply) as well as calorimeter ancillary electronics, fit in two standard containers.

Estimated dismounting time is 6 months.

9.2 Cost and Schedule: STT tracker

Item	Cost (USD)
Procure straws (Lamina Tubular Technology, UK)	1,429,120
Procure end plugs	437,891
Procure wire spacers	403,647
Procure crimping pins	386,941
Procure anode wire (Luma metall AB, Sweden)	456,288
Procure other miscellaneous components	123,925
Procure radiator foils (Bloomer Plastics Inc., USA)	112,000
Procure mechanics & C-fiber frames	3,821,194
Procure STT tools	569,000
Procure safety equipment & consumables	100,838
Procure gas system	1,590,000
Procure cooling system	1,060,000
Procure target parts	122,112
Procure front-end electronics (VMM3 & boards)	1,250,000
Procure back-end electronics	1,144,236
Procure HV components	291,654
Procure LV components	302,378
Procure cables & connectors	455,000
Procure DAQ system	82,055
Total	14,138,279

Table 15: Estimated core costs for the construction of the proposed STT.

We consider a default STT configuration based upon 80 modules with variable transverse dimensions, each composed of four straw layers XXYY. Assuming a single readout at one end of the straws, the total number of electronic channels is 224,000. We estimated the core costs for the construction of the complete STT using a mixture of updated quotes from vendors, costs of similar detector components used in different experiments, as well as the cost estimate of the larger STT from the DUNE CDR [29]. Table 15 summarizes

the corresponding costs for the various items. The costs of the engineering, module assembly and test are not included as they depend upon the project sharing among the interested institutions.

We will decide upon a primary production center for the STT modules. To this end, we can benefit from the activities planned for the DUNE CDR [29] and from the technical collaboration with institutions involved in the construction of other straw detectors. It would be useful to use 2-3 different production sites for the STT modules in order to reduce the time required for the construction of the STT. Furthermore, specific items like the readout electronics, the gas and cooling systems, the nuclear targets, etc. can be allocated to different institutions. With conservative assumptions on the number of assembly lines and manpower at a single production center, we expect to complete the STT construction, testing and installation in a period of less than 4 years. This estimate is consistent with the main schedule of the DUNE experiment and would make the proposed STT ready for the first neutrino beam available in LBNF.

The risk associated to the project is relatively small. As discussed in Sec. 3.3.1, the conceptual design is based upon well established technology and is similar to the ATLAS TRT [2, 3, 4] and COMPASS [26, 67] straw trackers. Low mass straws have been successfully developed for various modern projects including NA62 [72], COMET [64], SHiP [17], and Mu2e [55]. All the components required to build the STT can be manufactured industrially by vendors to be assembled into the final STT modules at the project production centers. Furthermore, the proposed STT is an evolution of the tracker from the reference ND design in the DUNE CDR [29]. As such, its design, cost and schedule successfully passed the technical and DOE CD1 reviews [32, 30, 31].

10 Summary of conclusions

Full simulations have demonstrated the excellent performances of the proposed detector. We outline that results presented here could be even further improved by refinements in the reconstruction algorithms. That is not needed for the time being.

Charged hadron and muon tracks are reconstructed with good resolution on momentum, around 3% , and on dip angle, around 1.7 mrad. Charge misidentifying is as low as 0.2%. Results are the same for events originating in the LAr target and in the STT target.

For what concerns electrons, direction is detected with unbiased mean and ≈ 0.9 mrad gaussian resolution. Momentum is reconstructed with a slight bias (3.8%) and a resolution of 5.1%. Wrong sign contamination is limited to 1.3% . Work is ongoing on reduction of non-gaussian tails in both energy and angle.

Neutral pions are reconstructed from clusters in the EM calorimeter. The π^0 invariant mass distribution in events with one or two π^0 has a resolution of 16% and 18% respectively.

Neutrons are detected both in the STT and in the EM Calo, with global efficiency 64%, rising to more than 72% for $E_{kin} > 100$ MeV. Neutron energy can be derived measuring the ToF from the vertex in the LAr meniscus to hits in STT or EM-CALO. Using this method, the neutron kinetic energy can be reconstructed with about 30% precision for 28% of the detected neutrons. The situation improves quickly with energy: On $E_{kin} > 50$ MeV 47% of detected neutrons are reconstructed within 30% accuracy. Work is ongoing to add calorimetric information to the measurement.

A full realistic event reconstruction based only on detected quantities, avoiding to use MC true information, is under development using FLUKA simulated events. Preliminary results are very encouraging.

Preliminary studies on physics performances have been derived implementing the reconstructed resolutions and efficiency on particle-level analyses.

Good resolution on tracks reflects, for instance, in good efficiency and purity for the kinematic selection of interactions on H, where purity and efficiency around 90% can be achieved.

The good efficiency for neutron detection allows to efficiently apply the low- ν method to derive the neutrino flux shape, both on the full STT target and on QE and RES events on Hydrogen. As many as 2.4×10^6 RES and 800 000 QE events on H are expected in 5 years.

The almost identical performances for events in the LAr meniscus and in the STT allow for direct comparison of events on Ar and H (or C) for nuclear effects assessment. These measurements will be complementary to the ones in the pixelated LAr detector, that will profit from larger statistics and will have the same detector effects as the Far one.

Charge separation and electron identification enables the determination of relative fluxes ν_e/ν_μ , $\bar{\nu}_e/\nu_\mu$, and all other species with high statistics (80000 $\bar{\nu}_e$ events in FHC mode in 5 years)

The very good angular resolution on electron tracks is an asset for flux determination from scattering on electrons, both in rate and shape: The selection efficiency is about 84% with a total background of 5%. This measurement can be combined with data from the LAr pixelated detector.

The whole detector can be moved on rails, for a PRISM-like exposure. The number of collected events will depend on how the exposure is fractionated, for instance for a uniform fractionation the largest angle will collect 3×10^4 ν_μ CC events.

11 Conclusions

The Near Detector system of the DUNE project is a strategic key point of the whole setup to achieve physics outputs at best.

A complementary design to the ND baseline recommendation has been fully evaluated, providing its reliability and readiness necessity.

The possibility to add a fully integrated multipurpose detector with magnetic and calorimetric capabilities, associated to a combined straw-tube tracker with enhanced performances in terms of physics profits, should be actively pursued, to our understanding.

The added value of a easy movable setup is also very important, to fully benefit of the DUNE-Prism option.

The results presented in this note with great details should be considered as a benchmark contributing to achieve the eventual optimized system for the ND.

References

- [1] Optimized Flux presented at Oct 2017 Beam Optimization Review. <http://home.fnal.gov/ljf26/DUNEFluxes/OptimizedEngineeredNov2017>.
- [2] E. Abat et al. The ATLAS Transition Radiation Tracker (TRT) proportional drift tube: Design and performance. *JINST*, 3:P02013, 2008.
- [3] E. Abat et al. The ATLAS TRT barrel detector. *JINST*, 3:P02014, 2008.
- [4] E. Abat et al. The ATLAS TRT end-cap detectors. *JINST*, 3:P10003, 2008.
- [5] P. Adamson et al. Neutrino and antineutrino inclusive charged-current cross section measurements with the minos near detector. *Phys. Rev. D*, 81:072002, Apr 2010.
- [6] M. Adinolfi et al. Calibration and reconstruction performances of the kloe electromagnetic calorimeter. *Nucl. Instrum. Meth.*, A461:344, 2001.
- [7] M. Adinolfi et al. The KLOE electromagnetic calorimeter. *Nucl. Instrum. Meth.*, A482:364–386, 2002.
- [8] Stephen L. Adler. Tests of the Conserved Vector Current and Partially Conserved Axial-Vector Current Hypotheses in High-Energy Neutrino Reactions. *Phys. Rev.*, 135:B963–B966, 1964. [,136(1964)].
- [9] S. Alekhin, Sergey A. Kulagin, and R. Petti. Modeling lepton-nucleon inelastic scattering from high to low momentum transfer. *AIP Conf. Proc.*, 967(1):215–224, 2007.
- [10] Sergey Alekhin, Johannes Blümlein, Sergey Kulagin, Sven-Olaf Moch, and Roberto Petti. Strange and non-strange distributions from the collider data. *PoS*, DIS2018:008, 2018.
- [11] D. Allasia et al. Q**2 Dependence of the Proton and Neutron Structure Functions from Neutrino and anti-neutrinos Scattering in Deuterium. *Z. Phys.*, C28:321, 1985.
- [12] L. Alvarez-Ruso et al. NuSTEC 1 1 Neutrino Scattering Theory Experiment Collaboration <http://nustec.fnal.gov>. White Paper: Status and challenges of neutrino-nucleus scattering. *Prog. Part. Nucl. Phys.*, 100:1–68, 2018.
- [13] J. Anderson, K. Bauer, A. Borga, H. Boterenbrood, H. Chen, K. Chen, G. Drake, M. DÄ¶nszelmann, D. Francis, D. Guest, B. Gorini, M. Joos, F. Lanni, G. Lehmann Miotto, L. Levinson, J. Narevicius, W. Panduro Vazquez, A. Roich, S. Ryu, F. Schreuder, J. Schumacher, W. Vandelli, J. Vermeulen, D. Whiteson, W. Wu, and J. Zhang. FELIX: a PCIe based high-throughput approach for interfacing front-end and trigger electronics in the ATLAS upgrade framework. *Journal of Instrumentation*, 11(12):C12023–C12023, dec 2016.
- [14] Tracking systems. http://www2.fisica.unimi.it/andreazz/AA_TrackingSystems.pdf.
- [15] C. Andreopoulos et al. The GENIE Neutrino Monte Carlo Generator. *Nucl. Instrum. Meth.*, A614:87–104, 2010.
- [16] M Anelli et al. Measurement and simulation of the neutron response and detection efficiency of a pb-scintillating fiber calorimeter. *IEEE Transactions on Nuclear Science*, 55(3):1409–1412, 2008.
- [17] M. Anelli et al. A facility to Search for Hidden Particles (SHiP) at the CERN SPS. arXiv:1504.04956, 2015.
- [18] A. B. Arbuzov, D. Yu. Bardin, and L. V. Kalinovskaya. Radiative corrections to neutrino deep inelastic scattering revisited. *JHEP*, 06:078, 2005.
- [19] P. Astier et al. Updated results from the nu/tau appearance search in nomad. *Phys. Lett.*, B483:387–404, 2000.
- [20] P. Astier et al. Final NOMAD results on muon-neutrino — $\bar{\nu}$ tau-neutrino and electron-neutrino — $\bar{\nu}$ tau-neutrino oscillations including a new search for tau-neutrino appearance using hadronic tau decays. *Nucl. Phys.*, B611:3–39, 2001.
- [21] G. Bassompierre et al. Performance of the NOMAD transition radiation detector. *Nucl. Instrum. Meth.*, A411:63–74, 1998.
- [22] G. Battistoni et al. Overview of the fluka code. *Annals of Nuclear Energy*, 82:10–18, 2015.

- [23] G. Battistoni, A. Ferrari, M. Lantz, P. R. Sala, and G. I. Smirnov. A neutrino-nucleon interaction generator for the fluka monte carlo code. In *CERN-Proceedings-2010-001*, pages 387–394, 2010. Proceedings of 12th International Conference on Nuclear Reaction Mechanisms, Varenna, Italy, 15-19 June 2009.
- [24] P. Bernardini et al. Enhancing the lbnf/dune physics program. <https://indico.cern.ch/event/65096/contributions/3295805/>, 2018. Proposal to European Strategy Group for Particle Physics, December 2018.
- [25] T. T. Boehlen, F. Cerutti, M. P. W. Chin, A. Fassò, A. Ferrari, P. G. Ortega, A. Mairani, P. R. Sala, G. Smirnov, and V. Vlachoudis. The FLUKA Code: Developments and Challenges for High Energy and Medical Applications. *Nucl. Data Sheets*, 120:211–214, 2014.
- [26] =V.N. Bychkov et al. Construction and manufacture of large size straw-chambers of the COMPASS spectrometer tracking system. *Particles and Nuclei, Letters*, 2 [111]:64–73, 2002.
- [27] A. Ceccarelli et al. Survey and alignment of the kloe experiment at da ϕ ne. Technical Report LNF-97/045 (P), INFN, 1997.
- [28] DUNE Collaboration. Long-baseline neutrino facility (lbnf) and deep underground neutrino experiment (dune) conceptual design report volume 2: The physics program for dune at lbnf. arxiv:1512.06148, 2016.
- [29] DUNE Collaboration. Long-baseline neutrino facility (lbnf) and deep underground neutrino experiment (dune) conceptual design report volume 3: Long-baseline neutrino facility for dune 2. arXiv:1601.05823, 2016.
- [30] The DUNE Collaboration. Director’s cd-1 refresh review of lbnf-dune. <https://web.fnal.gov/organization/OPSS/Projects/LBNFDUNE/SitePages/Director%27s%20CD-1%20Refresh%20Review%20of%20LBNF-DUNE,%20June%202-4,%202015.aspx>, 2015. Fermilab, 2-4 June 2015.
- [31] The DUNE Collaboration. Doe cd-1 refresh review of lbnf-dune. <https://web.fnal.gov/organization/OPSS/Projects/LBNFDUNE/SitePages/DOE%20CD-1%20Refresh%20Review%20of%20LBNF-DUNE,%20July%202014-16,%202015.aspx>, 2015. Fermilab, 14-16 July 2015.
- [32] The DUNE Collaboration. Dune near detector design review. <https://web.fnal.gov/project/LBNF/ReviewsAndAssessments/DUNE%20ND%20Design%20Review/SitePages/Home.aspx>, 2015. Independent ND technical review, Fermilab, 28-29 May 2015.
- [33] G. D’Agostini. A Multidimensional unfolding method based on Bayes’ theorem. *Nucl. Instrum. Meth.*, A362:487–498, 1995.
- [34] Zuxiang Dai. *Proton Decay Search with LAr TPC Detectors*. PhD thesis, ETH Zürich, 2005. Diss. ETH No. 16133.
- [35] G. De Geronimo, J. Fried, S. Li, J. Metcalfe, N. Nambiar, E. Vernon, and V. Polychronakos. Vmm1: An asic for micropattern detectors. *IEEE Transactions on Nuclear Science*, 60(3):2314–2321, June 2013.
- [36] J. Devan et al. Measurements of the inclusive neutrino and antineutrino charged current cross sections in minerva using the low- ν flux method. *Phys. Rev. D*, 94:112007, Dec 2016.
- [37] Dune-ND-GGD. <https://github.com/gyang9/dunendggd>.
- [38] DUNE Fluxes. <http://home.fnal.gov/~ljf26/2017DUNEFluxes/>.
- [39] H. Duyang, B. Guo, S. R. Mishra, and R. Petti. A Novel Approach to Neutrino-Hydrogen Measurements. arXiv:1809.08752, 2018.
- [40] H. Duyang, B. Guo, S. R. Mishra, and R. Petti. A Precise Determination of (Anti)neutrino Fluxes with (Anti)neutrino-Hydrogen Interactions. arXiv:1902.09480, 2019.
- [41] Edep-sim. <https://github.com/ClarkMcGrew/edep-sim>.
- [42] A. Ferrari, P. R. Sala, A. Fassò, and J. Ranft. Fluka: A multi-particle transport code (program version 2005). Technical Report 2005-10, CERN, 2005.
- [43] GENIE web site. <http://www.genie-mc.org/>.
- [44] gegede - General Geometry Description. <https://github.com/brettviren/gegede/>.
- [45] M. Glück, E. Reya, and A. Vogt. Dynamical parton distributions revisited. *Eur. Phys. J., C* 5:461, 1998.
- [46] David J. Gross and Chris H. Llewellyn Smith. High-energy neutrino - nucleon scattering, current algebra and partons. *Nucl. Phys.*, B14:337–347, 1969.
- [47] Richard J. Hill. On the single photon background to ν_e appearance at MiniBooNE. *Phys. Rev.*, D84:017501, 2011.
- [48] Richard J. Hill, Peter Kammel, William J. Marciano, and Alberto Sirlin. Nucleon Axial Radius and Muonic Hydrogen — A New Analysis and Review. *Rept. Prog. Phys.*, 81(9):096301, 2018.

- [49] George Iakovidis. Vmm3, an asic for micropattern detectors. In *5th International Conference on Micro-Pattern Gas Detectors (MPGD2017)*, 2017.
- [50] George Iakovidis. Vmm - an asic for micropattern detectors. *EPJ Web of Conferences*, 174:07001, 01 2018.
- [51] S. A. Kulagin and R. Petti. Nuclear parton distributions and the Drell-Yan process. *Phys. Rev.*, C90(4):045204, 2014.
- [52] Sergey A. Kulagin and R. Petti. Global study of nuclear structure functions. *Nucl. Phys.*, A765:126–187, 2006.
- [53] Sergey A. Kulagin and R. Petti. Neutrino inelastic scattering off nuclei. *Phys. Rev.*, D76:094023, 2007.
- [54] UK Lamina Tubular Technology. Private communications.
- [55] MyeongJae Lee. The Straw-tube Tracker for the Mu2e Experiment. *Nucl. Part. Phys. Proc.*, 273–275:2530–2532, 2016.
- [56] C. H. Llewellyn Smith. Neutrino Reactions at Accelerator Energies. *Phys. Rep.*, 3:261–379, 1972.
- [57] Kam-Biu Luk. 4th dune near detector workshop. indico.fnal.gov/event/15649/, 2018.
- [58] William J. Marciano and Zohreh Parsa. Neutrino electron scattering theory. *J. Phys.*, G29:2629–2645, 2003.
- [59] Steven Manly Mike Kordosky, Kam-Biu Luk and Alfons Weber. Report from the dune near detector concept study group. Technical Report DUNE-doc-8184-v2, DUNE, 2018.
- [60] S. Mishra. Probing hadron structure with neutrino experiments. *Proceedings of the Workshop on Hadron Structure Functions and Parton Distributions (edited by D. Geesaman and others, World Scientific)*, page 84, 1990.
- [61] M. Modena. The da ϕ ne cryogenic system. Technical Report LNF-97/046 (IR), infn, 1997.
- [62] D. Naumov et al. A study of strange particles produced in neutrino neutral current interactions in the nomad experiment. *Nucl. Phys.*, B700:51, 2004.
- [63] DUNE NearDet Design Redmine Project. https://cdcv.s.fnal.gov/redmine/projects/dune-neardet-design/wiki/DUNE_NearDet_Design.
- [64] H. Nishiguchi et al. Development of an extremely thin-wall straw tracker operational in vacuum – The COMET straw tracker system. *Nucl. Instrum. Meth.*, A845:269–272, 2017.
- [65] J. Park et al. Measurement of Neutrino Flux from Neutrino-Electron Elastic Scattering. *Phys. Rev.*, D93(11):112007, 2016.
- [66] R. Petti. private communication.
- [67] K. Platzer, W. Dunnweber, N. Dedek, M. Faessler, R. Geyer, C. Ilgner, V. Peshekhonov, and H. Wellenstein. Mapping the large area straw detectors of the COMPASS experiment with X-rays. *IEEE Trans. Nucl. Sci.*, 52:793–798, 2005.
- [68] D. Rein and L.M. Sehgal. Neutrino-excitation of baryon resonances and single pion production. *Annals of Physics*, 133:79–153, 1981.
- [69] O. Samoylov et al. A Precision Measurement of Charm Dimuon Production in Neutrino Interactions from the NOMAD Experiment. *Nucl. Phys.*, B876:339–375, 2013.
- [70] W. G. Seligman. *A Next-to-leading order QCD analysis of neutrino - iron structure functions at the Tevatron*. PhD thesis, Nevis Labs, Columbia University, 1997. FERMILAB-THESIS-1997-21.
- [71] Chien-Yeah Seng, Mikhail Gorchtein, Hiren H. Patel, and Michael J. Ramsey-Musolf. Reduced Hadronic Uncertainty in the Determination of V_{ud} . *Phys. Rev. Lett.*, 121(24):241804, 2018.
- [72] A. Sergi. NA62 Spectrometer: A Low Mass Straw Tracker. *Phys. Procedia*, 37:530–534, 2012.
- [73] K. M. Smith et al. Progress in the design and manufacture of the KLOE solenoid for the daphne ring at Frascati. *IEEE Trans. Appl. Supercond.*, 7:630–632, 1997.
- [74] Matthew Szydagis, Adalyn Fyhrie, Daniel Thorngren, and Mani Tripathi. Enhancement of NEST Capabilities for Simulating Low-Energy Recoils in Liquid Xenon. *JINST*, 8:C10003, 2013.
- [75] M. Tanabashi et al. Review of particle physics. *Phys. Rev. D*, 98:030001, Aug 2018.
- [76] M. Tzanov et al. Precise measurement of neutrino and antineutrino differential cross sections. *Phys. Rev. D*, 74:012008, Jul 2006.
- [77] D. Umbach and K. N. Jones. A few methods for fitting circles to data. *IEEE Transactions on Instrumentation and Measurement*, 52(6):1881–1885, Dec 2003.
- [78] A. Wehmann and S. Childress. Tritium production in the dolomitic rock adjacent to numi beam tunnels. Technical Report FERMILAB-TM-2083, FERMILAB, 1999.
- [79] J. Wolcott et al. Measurement of electron neutrino quasielastic and quasielasticlike scattering on hydrocarbon at $e_\nu = 3.6$ $mathrm{GeV}$. *Phys. Rev. Lett.*, 116:081802, Feb 2016.

- [80] Q. Wu et al. A precise measurement of the muon neutrino-nucleon inclusive charged current cross-section off an isoscalar target in the energy range $2.5 < e_\nu < 40$ -gev by nomad. *Phys.Lett.*, B660:19–25, 2008.
- [81] H. Wulandari, J. Jochum, W. Rau, and F. von Feilitzsch. Neutron flux at the gran sasso underground laboratory revisited. *Astroparticle Physics*, 22(3):313 – 322, 2004.
- [82] G. P. Zeller et al. A Precise determination of electroweak parameters in neutrino nucleon scattering. *Phys. Rev. Lett.*, 88:091802, 2002. [Erratum: Phys. Rev. Lett.90,239902(2003)].